HELSINKI UNIVERSITY OF TECHNOLOGY
Department of Civil and Environmental Engineering
Laboratory of Structural Mechanics

KIM CALONIUS

NUMERICAL SIMULATION OF THERMAL RESIDUAL STRESSES IN A FUNCTIONALLY GRADED MATERIAL COMPONENT

Thesis presented for examination for the degree of Master of Science
in Espoo on 17th of August 2000

Supervisor: Professor Juha Paavola
Instructor: LicTech Arja Saarenheimo

HELSINKI UNIVERSITY OF TECHNOLOGY

ABSTRACT OF THE MASTER'S THESIS

Author and name of the thesis: Kim Calonius

NUMERICAL SIMULATION OF THERMAL RESIDUAL STRESSES IN A FUNCTIONALLY GRADED MATERIAL COMPONENT

Date: 17.8.2000 Number of pages: 137

Department: Department of Civil and Environmental Engineering

Laboratory: Laboratory of Structural Mechanics

Supervisor: Professor Juha Paavola

Instructor: LicTech Arja Saarenheimo

The cooling stage of the Hot Isostatic Pressing manufacturing process of a functionally graded material component has been numerically simulated in this work. During the manufacturing process the temperature range varies widely from the room temperature to 1180°C. Non-linear thermo-visco-plastic analyses have been carried out using ABAQUS/Standard finite element method computer code. The material parameters needed for these analyses are partly compiled from the literature and partly acquired through the experimental work. The theoretical aspects of the constitutive model are described. The values of the material parameters needed to model the creep are obtained by curve fitting from the experimental data generated in this project. The simulated stresses are compared to the stresses obtained by X-ray diffraction measurements.

TEKNILLINEN KORKEAKOULU

DIPLOMITYÖN TIIVISTELMÄ

Tekijä ja työn nimi:	Kim Calonius
	JÄÄNNÖSJÄNNITYSTEN NUMEERINEN SIMULOINTI GRADIENTTIMATERIAALIKOMPONENTISSA
Päiväys:	17.8.2000
Sivuja:	137

Osasto:	Rakennus- ja ympäristötekniikan osasto
Oppituoli:	Rakenteiden mekaniikka

Valvoja:	Professori Juha Paavola
Ohjaaja:	LicTech Arja Saarenheimo

Tässä työssä on numeerisesti simuloitu gradienttimateriaalikomponentin isostaattisen kuumapuristuksen jäähtymisvaiheessa muodostuva jäännösjännitystila. Kyseisen valmistusmenetelmän aikana lämpötila vaihtelee huoneenlämpötilasta 1180 Celsius-asteeseen. Epälineaariset termo-viskoplastiset analyysit on suoritettu elementtimenetelmää käyttävällä ABAQUS/Standard tietokoneohjelmalla. Analyyseissä tarvitut materiaaliparametrit on osin kerätty kirjallisuudesta ja osin määritetty kokeellisesti. Käytettyyn konstitutiiviseen malliin liittyvä teoria on selostettu. Virumista kuvaavan materiaalimallin parametrit on saatu käyränsovituksella tämän projektin yhteydessä tuotetusta kokeellisesta datasta. Simuloituja jännityksiä on kvalitatiivisesti vertailtu jännityksiin, jotka on mitattu röntgendiffraktiomenetelmällä osittain simuloitua vastaavasta kappaleesta.

Foreword

This work is a part of the project "Numerical Simulation of Thermal Residual Stresses in Multimaterial Joints" funded by The Technology Development Centre of Finland, Technical Research Centre of Finland (VTT) and Finnish industry. This is the first project, which focuses on simulation of residual stresses in a multimaterial components using FEM analyses.

I wish to thank LicTech Arja Saarenheimo for providing me with an interesting topic for this study and for the patience and support given in the course of this work. I remember the fruitful conversations related to several topics with DrTech Liisa Heikinheimo and DrTech Kari Santaoja. The advice of Professor Juha Paavola is acknowledged.

I also wish to thank all the people involved in the technical and experimental work that was needed for the determination of the material properties of the cases studied. Special thanks are due to MSc Stefan Holmström and engineer Esa Varis for their valuable and professional help in the material testing and evaluation of the test results. I thank MSc Anssi Laukkanen for helping me in theoretical questions and to overcome the practical problems of modern technology. I wish to express my gratitude for the staff of VTT Manufacturing Technology who have had a significant contribution to the completion of this work.

Eero Korhonen and Mikko Lehmuskoski - You'll take my life but I'll take yours too!

Finally, I thank Taru, my beloved wife, for supporting me through this year. Emil, my son, you were born right after I started this work, and you also helped me to put aside this work occasionally - just when it was needed.

Espoo,

Author

Table of contents

Foreword 3

List of symbols 6

1 INTRODUCTION 9

2 MATERIALS AND MANUFACTURING 11

2.1 10CrMo910 Steel 12

2.2 AISI316L Steel 12

2.3 Functionally Graded Materials 13

2.4 Microstructural Characterization and Effects on the Material Properties 14

2.5 Component 14

2.6 Hot Isostatic Pressing (HIP) 15

2.6.1 Sample Procedure 17

2.6.2 Quantitative Metallography 22

3 UNCOUPLED HEAT TRANSFER MODEL 26

3.1 Theory 26

3.2 Thermal Properties 27

4 BUILDING UP THE CONSTITUTIVE MODEL 31

4.1 Coefficient of Thermal Expansion 33

4.1.1 Coefficient of Thermal Expansion Based on the Literature 34

4.1.2 Tests for Determination of the Coefficient of Thermal Expansion 34

4.1.3 Coefficient of Thermal Expansion Data for the Simulations 37

4.2 Elastic Model 39

4.2.1 Young's Modulus and the Poisson's Ratio Based on the Literature 41

4.2.2 Measurements of the Young's Modulus 41

4.2.3 Data of the Young's Modulus and the Poisson's Ratio 42

4.3 Elasto-Plastic Model 44

4.3.1 Isotropic Hardening 46

4.3.2 Tensile Properties Based on Literature 47

4.3.3 Yield and Tensile Strength Tests 48

4.3.4 Tensile Data Used in the Simulations 55
4.4 Rate-Dependent Metal Plasticity 58
4.4.1 Strain Hardening 58
4.4.2 Creep Tests 58
4.4.3 Curve Fitting 69
4.4.4 Creep data 74
5 NUMERICAL SIMULATION 78
5.1 Finite Element Method 78
5.2 Finite Element Models 79
5.2.1 Simulation Cases 83
5.2.2 Problem Size 85
5.3 Loading and Boundary Conditions 87
6 RESULTS 89
6.1 Results of Uncoupled Heat Transfer Analysis 89
6.2 Results of the Elastic-Viscoplastic Analysis 91
6.3 X-ray Diffraction Measurements and Results 106
7 SUMMARY AND DISCUSSION 111
8 REFERENCES 115
9 APPENDICES 117

List of symbols

A	creep model parameter
A^*	creep model parameter used in curve fitting program
b	thickness
c	specific heat
$\mathbf{D}^{el}$	elasticity tensor
d	arbitrary exponent
E	modulus of elasticity
$\mathbf{e}$	deviatoric strain
$\overline{e}$	deviatoric part of equivalent strain
F	force
$\mathbf{f}$	heat flux per unit volume / body force per unit volume
f	yield function
G	shear modulus
h	external heat supply per unit volume
$\mathbf{I}$	identity matrix
K	bulk modulus
$\mathbf{k}$	conductivity matrix
l	length
l_0	initial length
m	creep model parameter
m^*	creep model parameter used in curve fitting program
$\mathbf{N}$	interpolation matrix
$\mathbf{n}$	normal vector
n	creep model parameter
n^*	creep model parameter used in curve fitting program
p	equivalent pressure stress
q	heat flux per unit area
$\overline{q}$	uniaxial equivalent deviatoric stress (von Mises)
$\overline{q}^Y$	uniaxial equivalent yield stress
$R_{0.2}$	yield strength
$R_{1.0}$	stress, where the plastic strain is 1.0 %

R_m	rupture strength
r	radial coordinate
$\mathbf{S}$	deviatoric stress
S	surface area
S_0	initial surface area
T	temperature
T_{ref}	reference temperature
$\mathbf{t}$	force per unit area
t	time
U	internal energy
$\mathbf{u}$	nodal displacement
u	horizontal displacement component
V	volume
$\tilde{V}$	volume fraction
v	vertical displacement component
$\mathbf{x}$	position coordinates
z	axial coordinate

Greek symbols

α	coefficient of thermal expansion (in total form)
α'	coefficient of thermal expansion (in differential form)
γ_{ij}	shear strain
ε	(total) strain tensor
ε^{cr}	creep strain
ε^{el}	elastic strain
ε^{pl}	plastic strain
ε^{th}	thermal strain
$\bar{\varepsilon}^{cr}$	equivalent creep strain
$\bar{\varepsilon}^{pl}$	equivalent plastic strain
$\tilde{\varepsilon}^{pl}$	uniaxial plastic strain
ε_{nom}	nominal strain

ε_{vol}	volumetric strain
$\dot{\varepsilon}_{ref}^{cr}$	reference creep strain rate
θ	circumferential coordinate
λ	conductivity
ν	Poisson's ratio
ρ	density
σ	(total) stress tensor
σ_0	constant used in the creep parameter conversion
σ_{ij}	stress component
σ_{nom}	nominal stress
σ_{ref}	reference stress
σ_{true}	true stress
τ_m	shear strength

Abbreviations

10CrMo910	ferritic steel manufactured by HIP process
25/75 steel	alloy of 10CrMo910 and AISI316L
50/50 steel	alloy of 10CrMo910 and AISI316L
75/25 steel	alloy of 10CrMo910 steel and AISI316L steel
AISI316	conventionally manufactured austenitic steel
AISI316L	austenitic steel manufactured by HIP process
CEEQ	the equivalent creep strain
FEM	finite element method
FG	functionally graded
FGM	functionally graded material
HIP	hot isostatic press
PEEQ	the equivalent plastic strain
PM	powdermetallurgic
RT	room temperature
SHS	self-propagating high-temperature synthesis

1 INTRODUCTION

Pipe assemblies in heavy industry factories have to withstand demanding and varying conditions, such as high temperature, long-term wear and oxidative atmosphere. Due to the fact that it is of utmost importance to have an appropriate tube material for each condition, the material type has to alter within a tube. Two materials have to be connected somehow. Usually this is done with additional threaded fittings or by welding. Sometimes a fitting cannot be used and the materials cannot be welded together straight. One way to solve this transition is to use a transition part where two powder metallurgically processed materials are joined together using a high pressure and an elevated temperature enabling diffusion. The above-mentioned process is called hot isostatic pressing (HIP) (Chapter 2.6). Tubes can then be welded to the transition part.

Manufacturing techniques, such as casting or forging, leave residual stresses of magnitude near the yield strength in a solid. Usually they can be reduced by various post treatments, such as annealing in the case of metals. Annealing can also be carried out feasibly after diffusion bonding, but it is not very efficient in the case of mismatching joints as between a ferritic and an austenitic steel (Kemppainen, 1999). A homogenous component of a single material made by hot isostatic pressing would be virtually free of stresses (Concurrent Technologies Corporation, 1997). However, consolidation of two different materials induces thermal residual stresses, which develop during the cooling down phase especially at their interface. First of all, the mechanical and physical properties of two different materials change in a complex way as a function of time according to their own characteristics and secondly, the cooling is never uniform over the whole material.

There are different ways to reduce thermal residual stresses in multimaterial components. One possible way is to use a seamless bonding, in other words, a section of Functionally Graded Material (FGM) (Chapter 2.3). The main purpose of this study is to numerically simulate thermal residual stresses in a certain FG-material component manufactured at VTT Manufacturing Technology on March 14th 1996 (Chapter 2.5). This component consists of two base powder metals: a ferritic steel 10CrMo910 and a stainless steel AISI316L. The material gradient between these two different metals has been made as smooth as possible using powder

metallurgy based on FGM technology. The second goal is to find other ways to minimize the residual stresses.

To avoid misunderstandings, one thing has to be clarified already here in the introduction: The smooth material gradient is replaced by three alloy materials in the numerical simulations. The linearly changing material gradient would be too complex and time-consuming to simulate accurately and reliably in within the boundaries of this work. Moreover, the numerical models must not be confused with the component manufactured on the 4th of May 1999. That component has five alloy materials and is referred to often in this work.

The subject is approached from a practical point of view. The component, its dimensions, structure, materials and manufacturing are explained. Then a theoretical background for numerical simulations is given and the material parameters are defined. The data is collected partly from the literature and partly obtained from the experimental work. A suitable finite element mesh is created and calculations are carried out using different boundary conditions. Part of the simulation results are compared to the residual stresses of a component determined by the X-ray diffraction method. No exact mathematical methods of calculations are used to back up numerical simulations. Finally, the results of the measurements and the FEM-analyses are discussed and conclusions drawn.

2 MATERIALS AND MANUFACTURING

Manufacturing of Functionally Graded Materials has already been studied worldwide. Manufacturing of transition pieces with the same materials as in the component simulated in this work has also been researched before. The tests carried out before have shown that the manufacturing of FG-material tubes of two different powders of steels is not only possible but at least with the above mentioned materials easy as well with no technical problems. According to tensile tests the material strength of the transition part is clearly higher than that of any pure component. In addition, the standard cooling down cycle used by the HIP-machine in the mentioned manufacturing tests is presumably not the most optimal heat treatment for the component (Heikinheimo et al., 1998).

Altogether six different materials are used in the numerical simulations. Five of them are powder materials manufactured using the HIP process (Chapter 2.6): a ferritic steel 10CrMo910, a stainless steel AISI316L and their three alloys. The last material, a normal austenitic steel AISI316, is used in the process itself in the container for example. It is not a part of the finished component. The three gradient alloys are 75/25 steel, 50/50 steel and 25/75 steel. The numbers before and after the slash are volume percentages of 10CrMo910 and AISI316L, respectively. The same notation is used throughout the text. Table 2.1 shows the nominal compositions of the two base powder materials (Kosonen, 1999). All the values in the table are the allowable maximum proportions or allowable range of proportions for the major alloying elements. The balance is iron (Fe). The values of the metals manufactured by conventional methods (AISI316 steel) are slightly lower than the values of the metals manufactured by HIP process due to the loss of deoxidizing elements and carbon in conventional steel making processes. In addition, sulfur and phosphorous are cleaned off from the steel in conventional processes.

Table 2.1 Nominal compositions of powder materials used.

	10CrMo910	AISI316L
C	0.08 - 0.14	0.08
Cr	2.00 - 2.50	16.0 - 18.0
Mo	0.90 - 1.10	2.0 - 3.0
Si	0.50	1.00
Mn	0.40 - 0.80	2.00
P	0.030	0.045
S	0.025	0.03
Ni		10.0 - 14.0

2.1 10CrMo910 Steel

The steel 10CrMo910 is a heat resisting, ferritic type of low alloyed steel consisting mainly of iron (Fe). It is widely used and well characterized in the literature. It is always referred first in alloy compositions in this study, unless otherwise mentioned.

The steel 10CrMo910 is commonly used in components of energy production, especially in boiler tubes in water walls, evaporators and superheaters of waste incineration boilers. It is especially designed for long-term wear (cyclic load) for relatively high service temperatures (Heikinheimo, 1999).

2.2 AISI316L Steel

The steel AISI316L is known as for its good corrosion resistance. It is an austenitic stainless steel with a high content of chromium and nickel.

The steel AISI316L is used in harsh environments not suitable for normal steels and also simply in common households; in kitchen sinks for instance. Normal industrial applications are valves, pipe fittings and pumps designed for corrosive or otherwise toxic liquids. It is also used as a protective layer in compound pipes and sheath material for vulnerable sensors.

2.3 Functionally Graded Materials

An FG-material can be defined as a material whose composition changes in a desired way as a function of position, usually microstructurally from a base material to another one. It is a composite material without any sharp interfaces. Different kinds of coatings can also be included in this category. The aim is mainly to reach a gradual variation of mechanical or magnetic properties. A great benefit of FG-materials is a significant improvement in impact and thermal shock ductility or fatigue durability compared to other kinds of material joints for instance. It has long been assumed that interface mismatch stresses can be reduced by replacing a sharp interface with an intermediate composite layer and in a similar case to this study the analogy has been demonstrated by FEM-calculations (Saarenheimo et al., 1999). Nevertheless, understanding the stress reduction mechanisms, especially with the materials studied here, is limited.

FG-materials have been manufactured by many methods that can be classified to four categories (Salmi et al., 1998):

1. coating methods
2. powder metallurgic (PM) methods
3. Self-propagating High-temperature Synthesis (SHS)
4. other methods enabling gradient interfaces

The powdermetallurgic methods comprise many shaping, pressing and sintering steps of which the last step is the HIP process (see Chapter 2.6).

2.4 Microstructural Characterization and Effects on the Material Properties

The behavior of materials, especially large differences in material properties between different alloys, can be better understood by focusing on the microstructure of those materials. Only basic phenomena, which either improve or reduce the strength, are superficially considered.

10CrMo910 steel transforms from the ferritic phase (α) to the austenitic matrix phase (γ) at a temperature between 700°C and 900°C and AISI316L steel remains in the austenitic phase (γ) within the whole temperature range needed in this study.

2.5 Component

This study focuses on the certain tube manufactured on March 14th 1996. The initial dimensions of that component and its container are shown in Figure 2.1. The central core is machined slightly cone-shaped, so that it would be easier to separate from the container after the process. There is also room for the solid lubricant between the central core and the container. The FG-region is smooth. It does not consist of distinct material layers. Both the central core and the container are conventionally manufactured of normal austenitic steel AISI316. The lower part of the HIPped tube is ferritic steel and the upper part is austenitic steel.

During the manufacturing process, the temperature was measured at points referred as Z1 and Z2. Those points are in the gas space few millimeters from the container surface. The temperature values at those points were quite divergent. The lower part of the gas space in the furnace was distinctively cooler during the process. That is why more information was needed to be able to choose an accurate temperature data for the numerical analyses. The temperature was measured during the process of a very similar component on May 4th 1999 at points referred as Z1, Z2, W1 and W2 (see Figure 2.1). The points W1 and W2 are inside the tube. That similar component and its manufacturing are described more closely in Chapter 2.6.1.

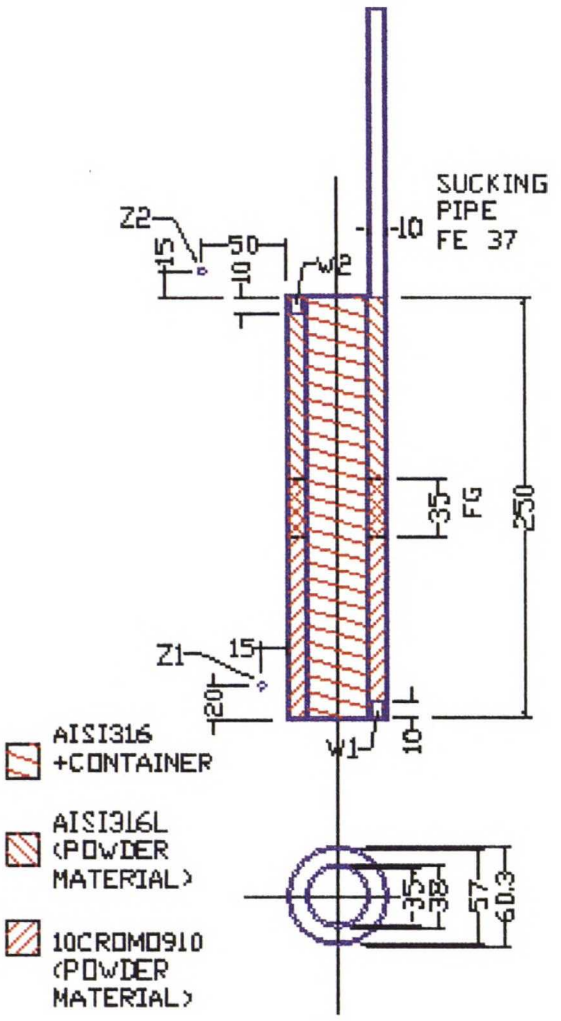

*Figure 2.1 Schematic presentation of the component with dimensions and different materials. Also the temperature measurement points are shown (*W1, W2, Z1 *and* Z2*).*

2.6 Hot Isostatic Pressing (HIP)

The component studied in this work is manufactured using a hot isostatic pressing process (HIP), where the material is consolidated under high isostatic pressure and at high temperature using gas as a medium substance for pressing. The initial state of the material can be solid, porous, or as in this case powder. Because the surface of the powder must be dense in HIPping, thus allowing the component to consolidate properly, the powder is tightly packed and sealed in a mould frame or a container, typically a metal can. In order to transfer the pressure to the powder, the container must be thin enough. It is then loaded into the HIP chamber,

vacuum is created in the container and the temperature and the pressure are applied typically simultaneously in the chamber according to a program.

Many things affect the material's degree of packing: Grain size and its distribution, grain shape, surface quality, agglomerizing, container size, segregation and different kinds of forces between the powder particles. The highest initial relative density of the powder (the powder density divided by the density of the final solid component) can be reached with broad distribution with many large grain sizes and few middle sizes and as circular grain shape as possible (Salmi et al., 1996). Presently in practice, however, the relative density is approximately 70% (Concurrent Technologies Corporation, 1997), thus the component dimensions change remarkably during the process. The dimensional control is the most difficult problem. It is hard to get the desired shape, but on the other hand with different kinds of frames it is possible to get completed components with curved holes for example, which are impossible to drill. This process requires an expensive equipment and time-consuming preparations. That is why it is at present used only to manufacture relatively expensive materials, such as tool steels, superalloys, titanium and ceramics that are also difficult to machine in shapes with conventional machining methods.

Some of the advantages of the HIP process in comparison to other metallurgical methods are (Concurrent Technologies Corporation, 1997):

1. High quality components from materials otherwise difficult to manufacture.
2. Elimination or reduced amount of machining or other finishing operations.
3. Controlled microstructure by powder characteristics and appropriate pressure and temperature cycle.
4. Diffusion bonding of two different materials, even ceramics and metals, without an extra filler metal.

The quality of HIPped materials is excellent; they are much more compact and isotropic than normal cast or forged metals. HIP is better than any other powdermetallurgic method and worth being studied and developed economically (Heikinheimo et al., 1998).

2.6.1 Sample Procedure

A component with exactly the same dimensions (except the FG-region) as the component simulated in this study was manufactured by VTT Manufacturing Technology on the 4th of May 1999. The cooling transient of the component manufactured earlier is used in the simulation, but the manufacturing details are better available for the component concerned in this chapter. Moreover, the temperatures measured at 4 different points give more information on the temperature state in the component during the process. With the aid of that information, the upper transient of the component manufactured earlier is chosen to be used in the analyses. Pressure and different temperatures were registered during the whole process, but only the cooling stage is considered as particularly important in this study. There were altogether 4 thermocouples: 2 of them were placed inside the container in the powder and the other two were outside the container in the gas space. The exact places can be seen in Figure 2.1. The thermocouples were of type B (Annual Book of ASTM Standards, 1991), which are reliable only at temperatures over 400°C. The folds in the graph (Figure 2.2) at that particular temperature are due to this fact. Argon (percentage of purity 99,998%) was used as a pressing gas.

The container was built up of two normally cast steel pipes (AISI316 steel), which were welded to a bottom. The lid included a sucking pipe (material Fe37) for the generation of partial vacuum. In the middle there was a central core, which helped to keep the desired dimensions for the final component. It was a solid cylinder manufactured of AISI316 steel. This central core was painted with boron nitride (BN) paint to prevent sticking with the pipe. For the same reason the core was slightly thicker towards the bottom. The paint is in fact only powder (75%) dissolved into water (25%). It lacks any binding agent. The powder consists of hexagonal boron nitride (87.3%) and aluminum oxide (12.7%). Boron nitride is normally used as a solid lubricant.

The FG-part was built up manually of five different layers of powder mixtures. In numerical analyses the simulated component have only three layers. Each layer in the manufactured component was about 7 mm in height. The 10CrMo910 steel powder and the AISI316L steel powder were first mixed and then each mixture was packed manually one on the other in the container. The upper part of the tube was austenite and the lower part was ferrite. The ratios of mixture were from the bottom to the top:

1. 83% 10CrMo910 + 17% AISI316L
2. 67% 10CrMo910 + 33% AISI316L
3. 50% 10CrMo910 + 50% AISI316L
4. 33% 10CrMo910 + 67% AISI316L
5. 17% 10CrMo910 + 83% AISI316L

Thus, the total height of the FG-region before the HIP process was 35 mm, designed to reduce to 30 mm in the final component. For comparison, the FG-region in the component manufactured in 1996 was smooth without any intentional homogenous layers. Ceramic rods supported and kept the container erect during the process. The dimensions are shown in Figure 2.1.

First both the temperature and the pressure were elevated nearly linearly to 1180°C and 100 MPa, respectively in about an hour. Next they were kept at the certain constant temperature for about 3 hours, in which time also the inner parts reached the same temperature and the powder fully consolidated. Finally, the furnace was cooled down and pressure discharged as shown in Figures 2.2 and 2.3. Also, the computer output of the beginning of the cooling down stage is presented below in Table 2.2.

Table 2.2 Extract of a computer output of the beginning of the cooling down stage (Kosonen, 1999).

Measuring of the cooling down rate of the IVO case component

Recipe name: STD1180F.REC
Data file: 255.PRN

Z1 = temperature measured by the lower thermal couple in the furnace [C]
Z2 = temperature measured by the upper thermal couple in the furnace [C]
W1 = temperature measured by the lower thermal couple inside the specimen [C]
W2 = temperature measured by the upper thermal couple inside the specimen [C]
TSP = temperature set point [C]
PRS = pressure [bar]
PSP = pressure set point [bar]
VAC = vacuum

constant time interval 30 seconds

Z1	Z2	W1	W2	TSP	PRS	PSP	VAC
1179	1180	1174	1171	1180	1002,2	1000	0
1105	1164	1159	1166	250	981,9	0	0
1032	1136	1123	1151	250	960,1	0	0
981	1110	1085	1132	250	943,4	0	0
932	1084	1047	1111	250	924,8	0	0
893	1062	1015	1092	250	909,5	0	0
855	1040	982	1071	250	894,9	0	0
825	1020	948	1053	250	881,1	0	0
793	999	915	1033	250	866,5	0	0
759	977	883	1012	250	851,8	0	0
732	958	857	995	250	840,4	0	0
709	938	834	978	250	829,4	0	0
684	918	809	957	250	817,5	0	0
659	899	785	938	250	806,3	0	0
636	880	761	918	250	795,3	0	0
618	866	742	903	250	786,7	0	0
596	847	720	884	250	775,6	0	0
579	833	700	868	250	766,6	0	0
560	817	680	852	250	757	0	0
537	801	657	835	250	746,9	0	0
515	784	636	818	250	737,4	0	0
498	769	618	805	250	729,1	0	0
483	756	603	792	250	722,2	0	0
465	740	584	775	250	713,5	0	0
449	725	567	759	250	705,1	0	0
434	710	548	742	250	697,2	0	0
422	699	531	730	250	690,8	0	0
411	687	518	719	250	684,5	0	0
398	675	503	706	250	678,5	0	0

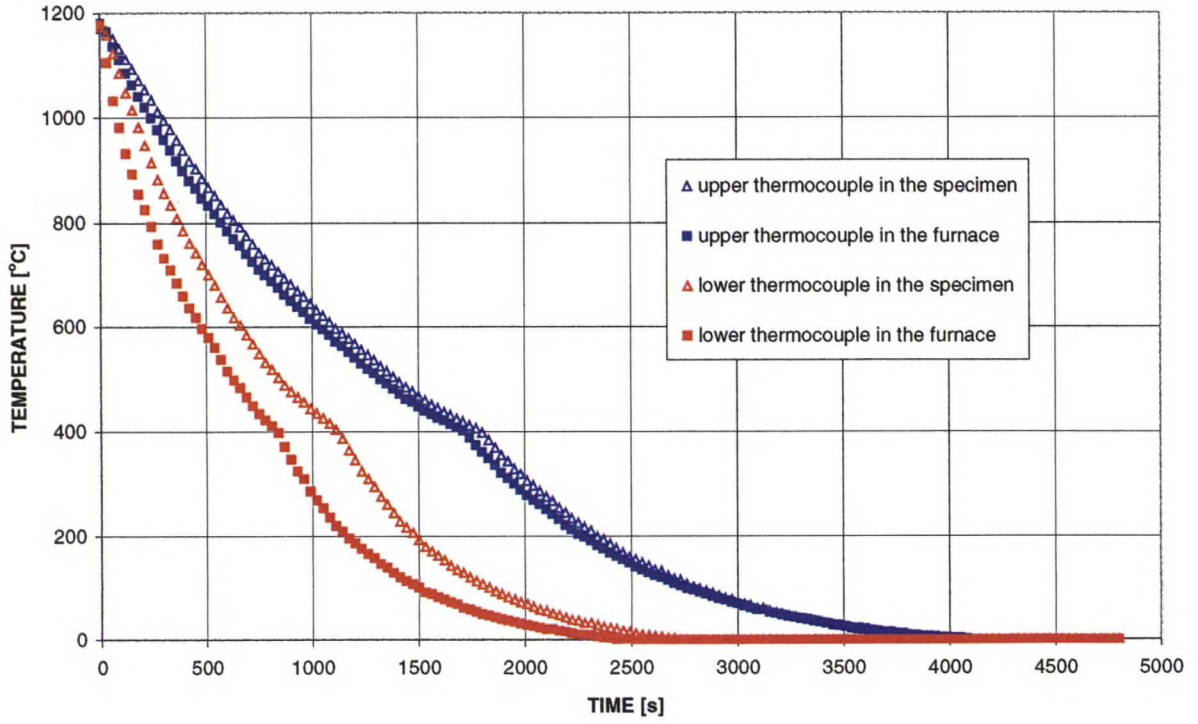

Figure 2.2 Temperatures during the cooling down stage of the HIP process on 4th of May 1999.

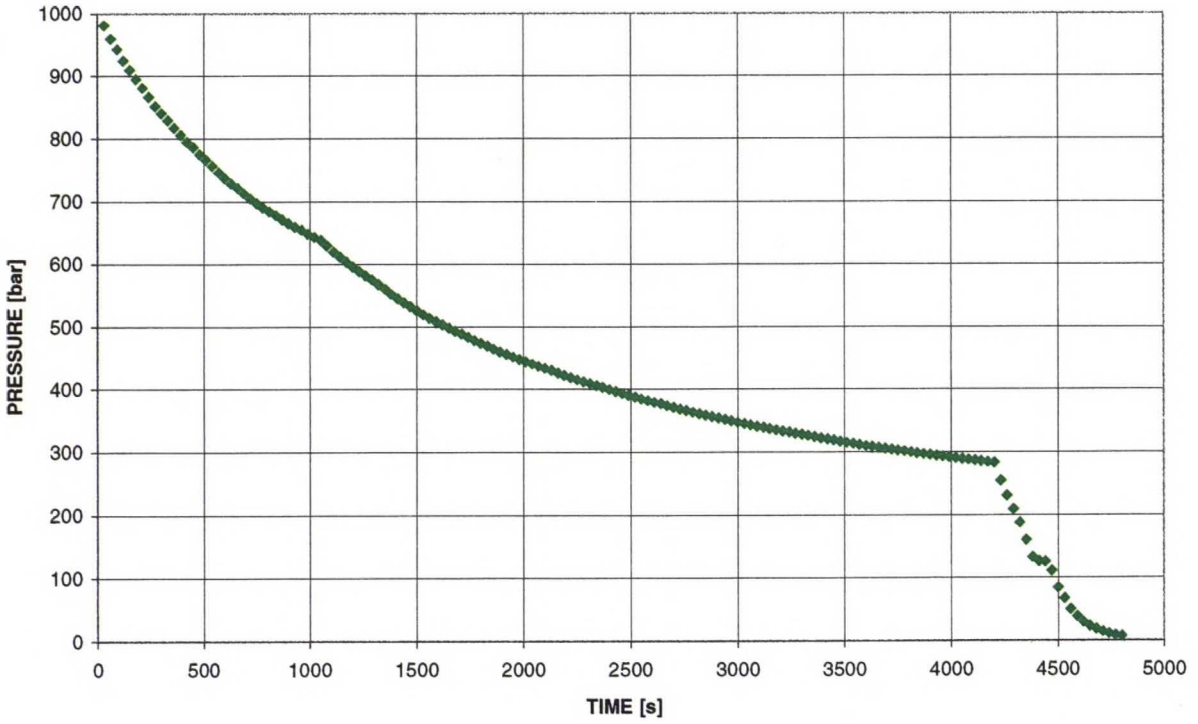

Figure 2.3 Pressure during the cooling down stage of the HIP process on 4th of May 1999.

Several hours after cooling down the furnace was opened and the component was taken out. The central core came loose from the container just by tapping it, but the sheet metal pipes of the container were merged with the HIP-material with a very strong diffusion bond. The ferritic and austenitic metals and the functionally gradient phases between them could easily be demonstrated with a piece of magnet. The magnetic field was clearly stronger in the bottom near 10CrMo910 steel and got weaker towards the top of the component. No accurate test with this respect was carried out.

The dimensions of the complete component after the HIP-process are shown in Figure 2.4. They are measured using a slide gage. The shape is slightly distorted, cone-shaped, as can be seen. There can be various reasons for this shape distortion. The pressure is not necessarily fully isostatic and the effect of the relatively thick container wall between the gas and the powder on the pressure to the powder is difficult to evaluate. The shape of the central core probably has the greatest effect on the distortion of the tube, if both parts are in contact during the process and the tube conforms to the shape of the cylinder. Thermal deformation must also be remembered. Presumably AISI316L steel contracts more due to the differences in the coefficients of thermal expansion.

The accurate initial relative density of the powder is difficult to define, but it was anyway higher than the general present value (70%) mentioned in Chapter 2.6.

There was noticeably a gap between the central core and the container and they were in direct contact only by few small points before uncoupling. For comparison, the diameter of the central core is after the process approximately 32.5 mm near the top and 33.5 near the bottom. The dimensions are nearly the same as before the process. Thus, the gap was finally approximately 1 mm wide uniformly from the bottom to the top. To remind, in the container, the inner diameter was 35 mm and the outer one 60.3 mm before the HIP process. Thus, the container was 12.65 mm thick. After the process it is approximately 10.5 mm thick near the top and approximately 10.4 mm near the bottom (calculated from Figure 2.4). So the thickness of the container is 83% of the original thickness near the top and 82% near the bottom. The compaction in vertical direction is minimal: The height is 99.7% of the original height.

In this connection, the compaction means total change of dimension during the whole HIP process. Thus, it includes consolidation and all inelastic strains, for example. The change of

volume due to the solidification of the powder takes mainly place already during the elevation of the temperature and pressure.

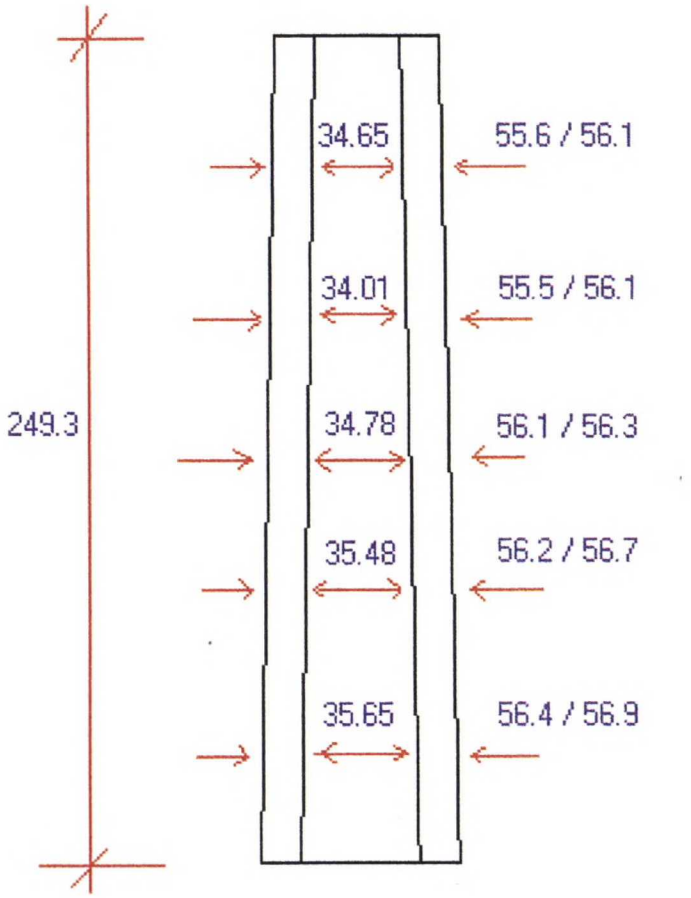

Figure 2.4 Dimensions of the final component (manufactured on 4th of May 1999). The outer diameter in the direction of the thermocouples, which were attached to the opposite sides of the component, is presented before the slash. The correspondent value in the perpendicular direction to the thermocouples is presented after the slash. The inner diameters are in the direction of thermocouples.

2.6.2 Quantitative Metallography

The material composition in the FG-region of the component manufactured on 4th of May 1999 (Chapter 2.6.1) is examined by quantitative metallography. It has to be remembered that the FG-region examined with metallography had five distinct material layers, whereas the component this thesis focuses on has a smooth FG-region.

The phase proportions are determined from a scanned microstructure photograph. A microstructure photograph of a similar component to the studied one is shown in Figure 2.5 (Heikinheimo et al., 1998). The magnification factor of the photograph shown is 65. The main materials in that photograph are the same as the ones studied on this work, except the composition of especially AISI316L steel is slightly different. As can be seen, the two main materials remain separated on a microscopic level. In Figure 2.5, 10CrMo910 steel is the darker material and AISI316L steel is the lighter one.

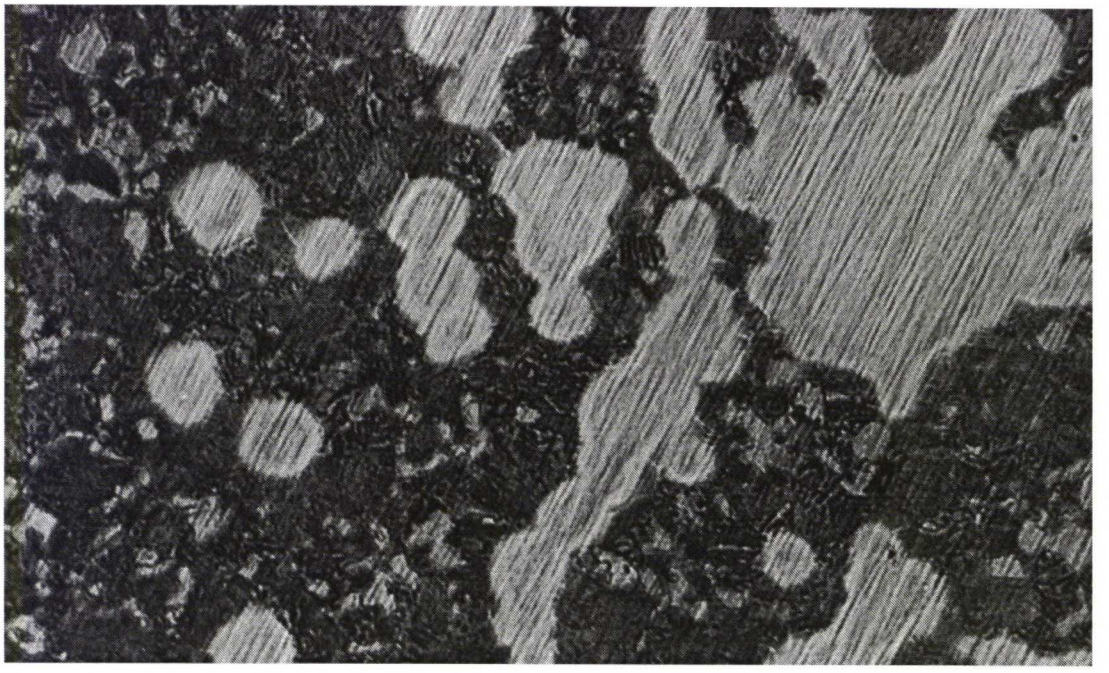

Figure 2.5 Scanned microstructure photograph of a similar component to the studied one. The magnification factor is 65. The darker material is 10CrMo910 steel. (Heikinheimo et al., 1998).

The phase areas displayed in the PC screen are separated by manual drawing with mouse. The photograph is taken from the microsection cut from the FG-region. The microsection cut is from the surface of the tube (powder material). The percentual composition is measured at nine points as shown in Figure 2.6. The proportions of ferrite and austenite are defined in the horizontal axis. The distance in the horizontal axis is measured from the bottom of the component (from the ferritic side). Thus, if the FG-region was 30 mm high and axially in the center of the tube as the intention was, it would begin at the approximated distance of 110 mm from the bottom.

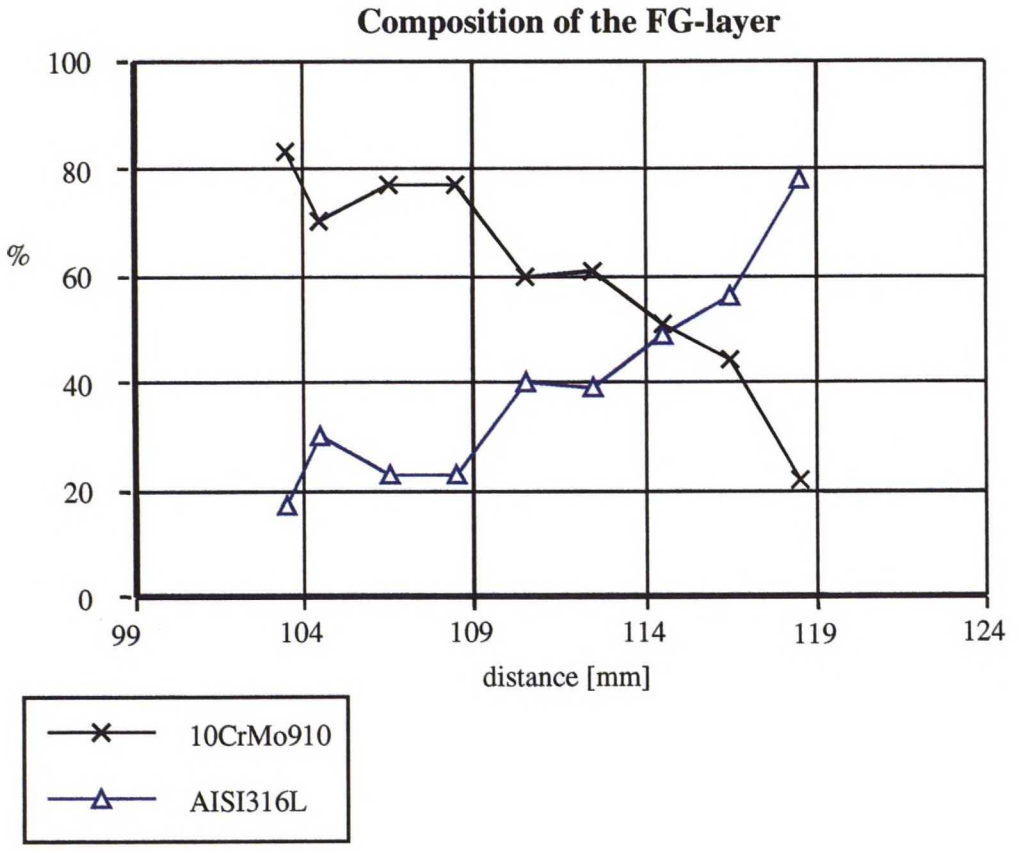

Figure 2.6 Composition of the FG-layer of the component manufactured on 4th of May 1999. The percentual proportion of the materials are in the vertical axis.

According to Figure 2.6, the phase proportion changes from approximately 80/20 to approximately 80/20 in a distance of 15 mm. Thus, the estimation of the total height of the FG-region in that area is 20 mm. It is surprisingly low, when recalling that the powder layers were initially altogether 35 mm high and the total compaction of the component after the HIP process in vertical direction is very minimal, only approximately 1 mm. In addition, the alloy materials are located quite asymmetrically in the vertical direction. The FG-region is closer to the ferritic end than to the austenitic end.

The area analyzed in Figure 2.6 is approximately 15 mm apart (in the circumferential direction) from the area, where the X-ray diffraction measurements are made. The X-ray measurements are explained in Chapter 6.3. To ensure that the results of the quantitative metallography are correct, another microsection is taken from the opposite side of the X-ray measurement area and analyzed. Both the microsections are at 15 mm distance from the X-ray measurement area. In the other microsection the FG-region is approximately 30 mm high. Ac-

cording to the visual estimation, no distinct microstructural layers are detected in either of the microsections, but the structure seems to change relatively smoothly.

The height of the FG-region varies in different locations of the pipe. The powders are packed clearly asymmetrically at least both in axial and circumferential directions. This variation is formed probably during the powder filling stage of the HIP-process, since the manual packing is difficult. Additionally, normal vibration could not be done, due to which the powders were not compact enough. In future industrial applications, the packing is done more precisely. (Kosonen, 2000).

3 UNCOUPLED HEAT TRANSFER MODEL

3.1 Theory

The heat transfer analysis is based on the energy balance between the internal energy of a body and the external energy conveyed to a body. The basic energy balance equation is

$$\int_V \rho \dot{U} dV + \int_V \mathbf{f} dV = \int_S q dS + \int_V h dV , \tag{3.1}$$

where V is a body volume and S is its surface area, ρ is the density of the material, U is internal energy, $\mathbf{f}$ is the heat flux in the body per unit volume, q is the heat flux to the body per unit area and h is the external heat supply per unit volume. The analysis is uncoupled in the sense that both internal and external energies are assumed to be only thermally dependent, disconnected from mechanical problems. This is only a simplification of the actual situation, where at least h is also depending slightly on the strains of the body (ABAQUS, 1998).

The material properties needed for the heat transfer analysis are thermal conductivity, specific heat and density. Conductivity is isotropic - as usual in case of metals. Because coupling between mechanical and thermal problems is neglected and no latent heat effect takes place at phase changes in the temperature range of the analysis, the internal energy can be defined by specific heat, c, in a single equation

$$c(T) = \frac{dU}{dT} , \tag{3.2}$$

where T is temperature. Heat conduction is assumed to be governed by the Fourier law,

$$\mathbf{f} = -\mathbf{k} \frac{\partial T}{\partial \mathbf{x}} , \tag{3.3}$$

where $\mathbf{k}$ is the fully isotropic conductivity matrix $\mathbf{k}(T) = \lambda(T) \cdot \mathbf{I}$, $\mathbf{f}$ is the heat flux and $\mathbf{x}$ is the position vector.

The heat transfer is in fact a pure diffusion problem, because in this work no heat flux to the body is applied. Instead, only the surface temperature as a boundary condition is given. Equation (3.1) is thus simplified to a form

$$\int_V (\rho \dot{U} + \mathbf{f}) dV = 0. \tag{3.4}$$

3.2 Thermal Properties

All the material parameter values for the heat transfer analysis are compiled from the literature mentioned in Table 3.1. The values are originally for the conventionally manufactured metals, but they are assumed to be valid also for the powder materials. The values for interlayer materials are estimated using the Law of Mixtures (Heikinheimo, 1999)

$$X = \sum V_i \cdot X_i = V_{AISI316L} X_{AISI316L} + V_{10CrMo910} X_{10CrMo910}, \tag{3.5}$$

where V_i is the volume fraction of the particular base material and X_i its value. This assumption is justifiable, since the thermal properties are to a large extent based on material specific factors, i.e. proportion of ingredients. AISI316L steel is assumed to have equal values to AISI316 steel.

The density is assumed to be constant at every temperature. The value for 10CrMo910 is 7840 kg/m^3 and the value for AISI316 is 7900 kg/m^3.

Table 3.1 Thermal properties of the base materials in the study as a function of temperature. Values in Italics are extrapolated or otherwise approximated.

T °C	10CrMo910 /1/ λ [W/mK]	10CrMo910 /1/ c [J/KgK]	AISI316 /2,3/ λ [W/mK]	AISI316 /2,3/ c [J/KgK]
25	35	460	14.6	500
100	37	490	16.2	
200	38	520		
300	38	560		
400	37	610		
500	35	680	21.5	
600	33	760		
700	*23*	*870*		
800	*25*	*875*	*25*	*875*
900		*846*		
1000	*27*	*827*		*827*
1027			*28.5*	
1127		*807*		*807*
1327	*29*	*807*	*30.5*	*807*

extrapolated/approximated values are in italics

/1/ ASM Metals Handbook, Volume 1. Properties and Selection: Irons, Steels, and High-performance Alloys, 10th ed. Eds. Davis, J.R. et al. ASM International, USA, 1990. 1063 p.

/2/ Saarenheimo et al., 1999

/3/ ASM Specialty Handbook Stainless Steels, Ed. Davis, J. R. ASM International, USA, 1994. 577 p.

Table 3.2 Thermal properties of the FG materials. They are estimated using Equation 3.5.

T °C	75/25 λ [W/mK]	75/25 c [J/KgK]	50 / 50 λ [W/mK]	50 / 50 c [J/KgK]	25/75 λ [W/mK]	25/75 c [J/KgK]
25	29.9	470	24.8	480	19.7	490
100	31.8		26.6		21.4	
200						
300						
400						
500	31.625		28.25		24.875	
600						
700						
800	*25*	*875*	*25*	*875*	*25*	*875*
900						
1000		*827*		*827*		*827*
1027						
1127		*807*		*807*		*807*
1327	*29.375*	*807*	*29.75*	*807*	*30.125*	*807*

extrapolated/approximated values

Figures 3.1 and 3.2 show thermal conductivity (λ) and specific heat (c) of the two base materials, respectively, as a function of temperature. Notice the fold in Figure 3.1 with 10CrMo910 steel. It takes place in the region of phase transformation of the material in question (approximately 700°C). Red color represents 10CrMo910 steel and blue color represents AISI316L steel in this study. Later on, the mixtures are represented by colors that are roughly between red and blue.

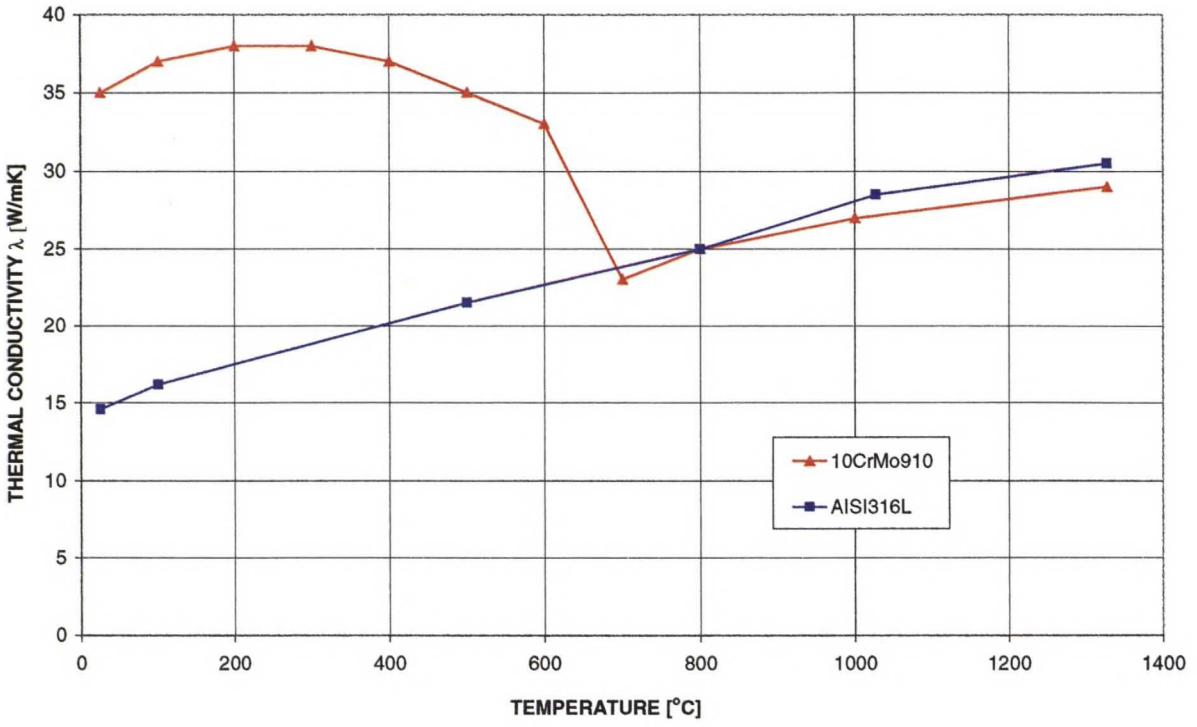

Figure 3.1 Thermal conductivity (λ) of the base materials, 10CrMo910 steel and AISI316L steel, as a function of temperature.

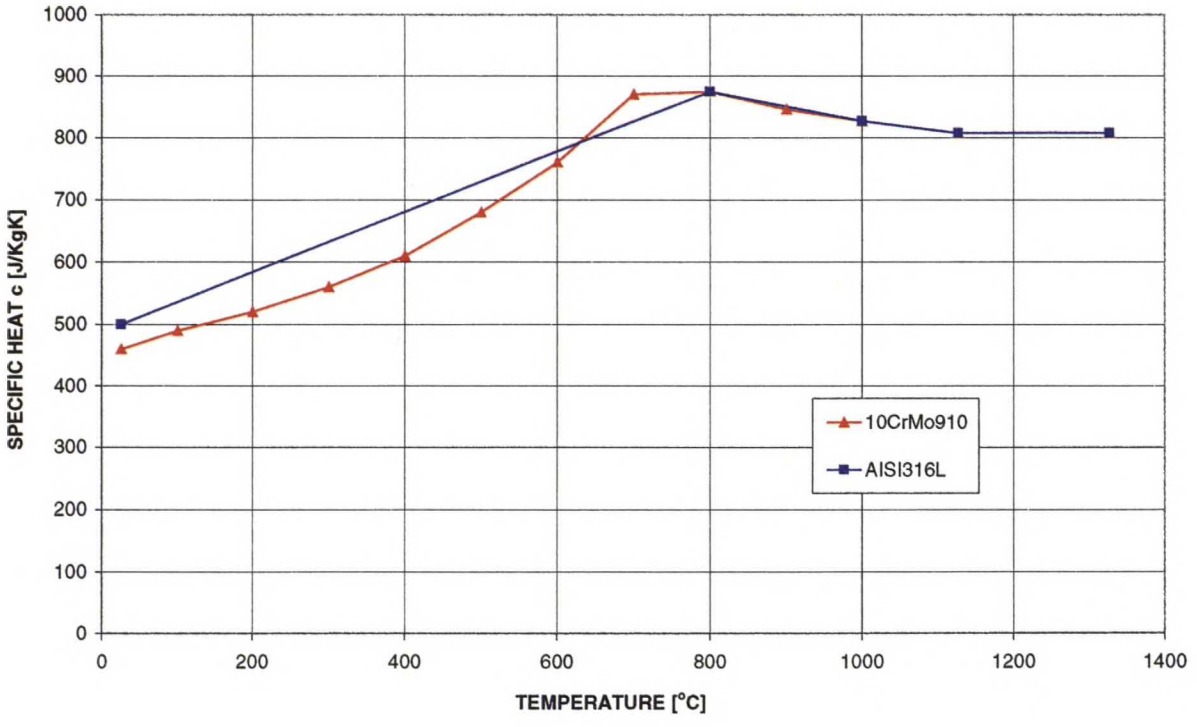

Figure 3.2 Specific heat (c) of the base materials, 10CrMo910 steel and AISI316L steel, as a function of temperature.

4 BUILDING UP THE CONSTITUTIVE MODEL

The continuum mechanics draws its physical information from three sources: the conditions of equilibrium, the kinematic relations and the stress-strain relations. The stress-strain relations are the mathematical description of the mechanical properties of the material - its constitutive equations. The kinematic relations define independently of the forces acting on a solid or the material characteristics the motion which leads from the undeformed to the deformed position (Flügge, 1972). The internal stress state of a solid can be defined by finite element method using both the kinematic and stress-strain relations, when the external forces are known and the solid is supposed to be in equilibrium (Chapter 5.1).

All the materials in this study are modeled as isotropic thermo-viscoplastic (rate-dependent) materials. This is due to the fact, that during the manufacturing process they have to undergo severe conditions - both mechanically and thermally. In this chapter the constitutive models for all the materials used in numerical simulation are built up step by step. The basic feature of the whole system is that the deformation is divided into four different parts, which are in this text approached in the following order: thermal, elastic, plastic and creep deformations. Usually, both plastic and creep deformations are included in a single unified visco-plastic model, but in this work they are handled separately. The theoretical aspects are also described for every step and the nonlinear equilibrium equations are derived. The implementation of these models from a numerical viewpoint is described in the next chapter. That means basically implicit integration of constitutive equations at every integration point over every time increment of the analysis.

The component studied is a body of revolution (axially symmetric solid) under axially symmetric loading and boundary conditions. By symmetry, the two components of displacements in any plane section of the body along its axis of symmetry define completely the state of strain and, therefore, the state of stress. There is, however, an essential difference between plane stress problem and the axisymmetric situation: The fourth component of strain and of the associated stress in the circumferential direction have to be considered (Zienkiewicz, 1977). When r and z denote the radial and axial coordinates of a point, respectively, u and v are the corresponding displacements. The displacement field is given by vector

$$\mathbf{u} = \begin{Bmatrix} u \\ v \end{Bmatrix}. \tag{4.1}$$

The strain vector defined below lists the strain components involved in the analysis and defines them in terms of the displacements of a point. The numbered indexes are used henceforth in the text.

$$\boldsymbol{\varepsilon} = \begin{Bmatrix} \varepsilon_r \\ \varepsilon_z \\ \varepsilon_\theta \\ \gamma_{rz} \end{Bmatrix} = \begin{Bmatrix} \varepsilon_{11} \\ \varepsilon_{22} \\ \varepsilon_{33} \\ \gamma_{12} \end{Bmatrix} = \begin{Bmatrix} \dfrac{\partial u}{\partial r} \\ \dfrac{\partial v}{\partial z} \\ \dfrac{u}{r} \\ \dfrac{\partial u}{\partial z} + \dfrac{\partial v}{\partial r} \end{Bmatrix}, \tag{4.2}$$

where θ denotes the circumferential coordinate of a point. The associated stress vector is

$$\boldsymbol{\sigma} = \begin{Bmatrix} \sigma_{11} \\ \sigma_{22} \\ \sigma_{33} \\ \sigma_{12} \end{Bmatrix}. \tag{4.3}$$

Notice how sigma instead of τ is used to symbolize the shear stress.

The exact solution for the displacements and stresses in a solid body requires that both the equilibrium of momentum and the equilibrium of moment of momentum should be maintained at all times over any arbitrary volume of the body. The corresponding statement for the heat transfer analysis is in Equation (3.4). Let S be the surface bounding any arbitrary volume, V, of material in the body. Let the surface traction (force per unit area) at any point on S be $\mathbf{t}$, and the body force per unit volume be $\mathbf{f}$. The equilibrium of momentum for that volume is then

$$\int_S \mathbf{t} dS + \int_V \mathbf{f} dV = 0 \tag{4.4}$$

and the equilibrium of moment of momentum is most simply written by taking moments about the origin

$$\int_S (\mathbf{x}\times\mathbf{t})dS + \int_V (\mathbf{x}\times\mathbf{f})dV = 0\,. \tag{4.5}$$

Equations (3.4), (4.4) and (4.5) are further used to develop basic finite element equations.

Some of the final data is based on literature, but mostly (unless otherwise referred) - especially at high temperatures - the data is based on tests carried out in the project, which this study is part of. The data was processed to the input needed for the ABAQUS program.

4.1 Coefficient of Thermal Expansion

If a structure is not free to expand, a change of temperature will cause stresses in it. The thermal expansion coefficient is the most fundamental property, when studying the development of thermal residual stresses in a multimaterial system. The difference of the values of this parameter between two materials produces substantial stress peaks, whenever the part is exposed to a thermal cycle, such as processing. The deformations in the shape of the component during the cooling stage of the HIP process are due to the thermal expansion.

Thermal strains develop according to the formula

$$\varepsilon^{th} = \int_{T_0}^{T} \alpha' dT\,, \tag{4.6}$$

where T_0 is the initial temperature and α' is the coefficient of thermal expansion in differential form. However, if α' depends on the temperature, the equation expands to the total form

$$\varepsilon^{th} = \alpha(T)(T - T_{\text{ref}}) - \alpha(T_0)(T_0 - T_{\text{ref}})\,, \tag{4.7}$$

where α is the thermal expansion coefficient in total form (not differential form), T is the current temperature, T_0 is the initial stress free temperature and T_{ref} is the reference temperature. The total thermal expansion values are defined from the reference temperature. Shortly, $\alpha(T)$ is an average coefficient between the reference temperature and the current temperature. Since it is assumed that there is no thermal strain at the initial conditions, the strain due to the difference between T_0 and T_{ref} (the second term in the above equation) must be subtracted to obtain the thermal strain at the current temperature. Equation 4.7 is clearly simplified, if the initial stress free temperature and the reference temperature are equal.

4.1.1 Coefficient of Thermal Expansion Based on the Literature

There is no data of powder materials available especially at high temperatures, but the data of AISI316 steel exists up to 1000°C. Values for the coefficient α at temperatures 1100°C and 1200°C are extrapolated by comparing them to the measured values of the powder material AISI316L (Table 4.1).

Table 4.1 Coefficient of thermal expansion of AISI316 steel as a function of temperature (ASM Metals Handbook, 1990).

T [°C]	α [10^{-5}/°C]
25	1.65
200	1.65
400	1.75
600	1.85
800	1.9
1000	1.95
1100	2.2
1200	2.3

small font extrapolated

4.1.2 Tests for Determination of the Coefficient of Thermal Expansion

The thermal expansion of metals within the temperature range from 20°C to 1200°C is measured with a dilatometer, which is part of a thermoanalysis equipment (Netzsch STA 429) at

VTT. The dilatometer measures changes in the volume of a body. The measured samples are cut out from the slender middle part of the tensile test (Chapter 4.3.3) specimens. The following experimental parameters are used:

ATMOSPHERE:	AIR, STATIC
SAMPLE HOLDER:	Al_2O_3
SPECIMEN LENGTH:	20-30 mm
THERMOCOUPLES	Pt/Pt-Rh(10)
RANGE	dl 1250 µm
	dl/dt 200 µV
TEMPERATURE PROGRAM	heating +20°C→ +700°C, 2°C/min
(for AISI316L steel and 50/50 steel)	keeping 2 h
	heating +700°C→ +1200°C, 2°C/min
	keeping 0,5 h
	cooling down to room temperature, 5°C/min

Because there is no cooling system available, the final phase is not linear (Koskinen, 1999). Similar tests are made for steel materials 75/25 and 25/75 except that the temperatures at the constant hold are 730°C and 1225°C instead of 700°C and 1200°C. The thermal expansion values are based on the volume changes measured during the heating.

Two readings are needed, temperature T and strain $\Delta l / l_0$. The strains are defined from the volume changes. The first measured value of strain is the reference strain, using which the coefficient of thermal expansion in the total form is calculated at any temperature. The reference strain is measured at the reference temperature, which is near the room temperature with each material. The coefficient of thermal expansion is

$$\alpha\big|_T = \frac{\Delta l / l_0\big|_T - \Delta l / l_0\big|_{T_{ref}}}{T - T_{ref}}, \tag{4.8}$$

where T_{ref} is the reference temperature and l_0 is the initial volume or length of the specimen (not necessarily in the reference temperature).

Figure 4.1 shows the measured thermal strain values for 75/25 steel during the test. That shows graphically and directly how the material expands. The strain at temperature of 1180°C is approximately 0.0172.

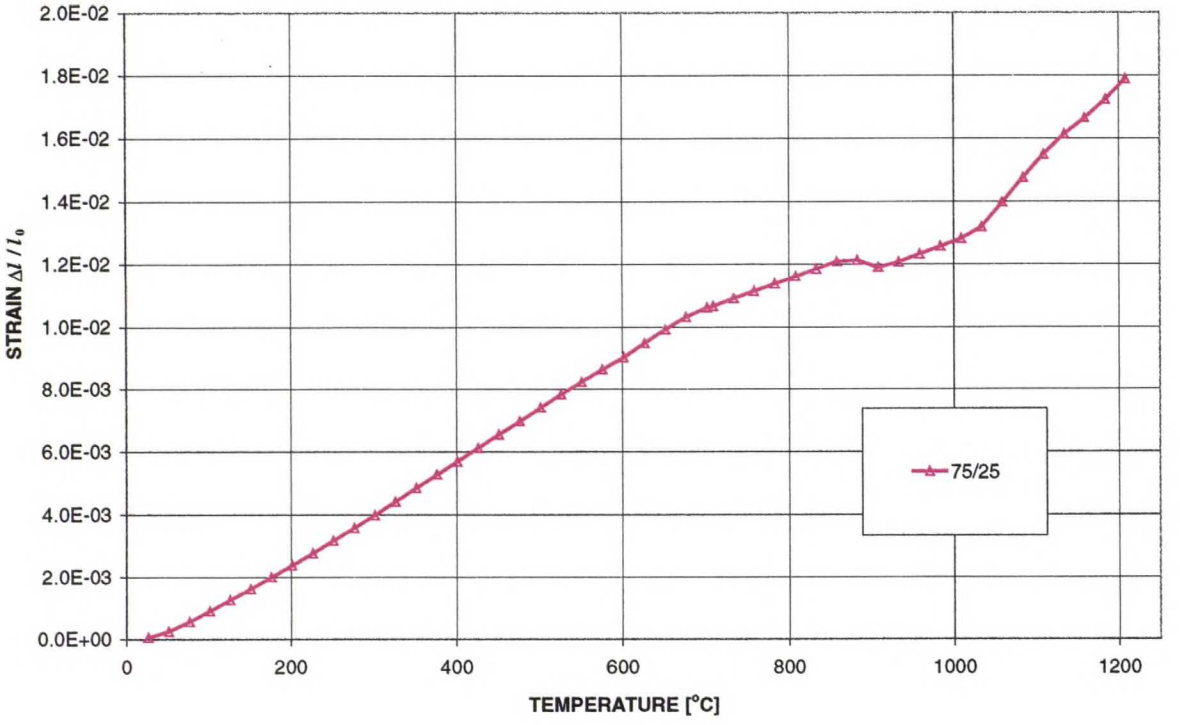

Figure 4.1 Test thermal strain values of 75/25 steel.

Figure 4.2 shows graphically the idea behind Equation 4.8. The coefficients are calculated from the test values in Figure 4.1 in the same manner as in Figure 4.2.

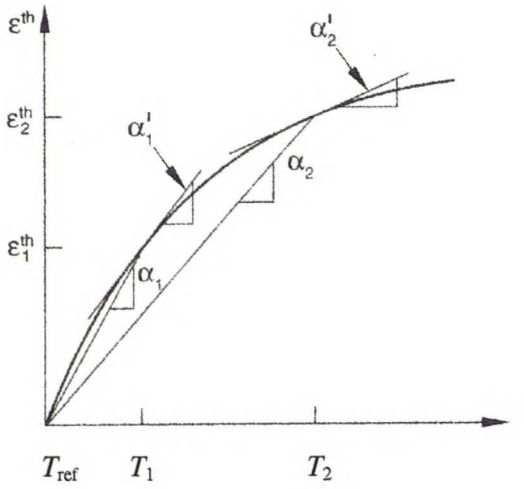

Figure 4.2 The idea behind the differential (α_i') and total (α_i) form of the thermal expansion coefficient.

In order to cut down the number of data points by two thirds, the initial points are arranged into groups of three points with consecutive temperature values. New values are created by taking a mean temperature and strain values of every group. This is done also to decrease the slight fluctuation of test values, since according to other similar materials the behavior should be quite smooth between the transition states. Because the values below 100°C are not very reliable, the first values are set equal to a value at 50°C-100°C. The start of the T-α-curve is made straight horizontally. Because only one test is done for each material, it is difficult to estimate the error, but on the basis of previous studies the error in values has normally been between 2%-3% (Koskinen, 1999)

4.1.3 Coefficient of Thermal Expansion Data for the Simulations

Table 4.2 shows the values of α of each material used in FEM analyses except AISI316 steel, which is shown in Table 4.1.

Table 4.2 Coefficient of thermal expansion as a function of temperature.

10CrMo910		75/25		50/50		25/75		AISI316L	
T [°C]	α [10^{-5}/°C]	T [°C]	α [10^{-5}/°C]	T [°C]	α [10^{-5}/°C]	T [°C]	α [10^{-5}/°C]	T [°C]	α [10^{-5}/°C]
25	0.549	25	1.146	25	1.5	25	1.084	25	1.7
50	0.549	101	1.146	100	1.5	125	1.084	85	1.7
100	0.687	151	1.257	150	1.63	175	1.347	115	1.8
200	1.1	226	1.362	225	1.8	250	1.587	175	1.867
300	1.27	301	1.432	300	1.8	325	1.66	265	2
400	1.35	376	1.491	375	1.8	400	1.699	355	2.033
500	1.38	451	1.525	450	1.8	475	1.698	445	2.1
600	1.39	526	1.551	525	1.8	550	1.729	535	2.167
700	1.39	601	1.559	600	1.867	625	1.726	625	2.167
800	1.36	626	1.57	675	1.567	697	1.69	729	2.1
825	1.33	651	1.577	808	1.5	745	1.697	813	2.1
850	1.24	676	1.58	933	1.45	820	1.663	888	2.2
875	1.18	701	1.565	1033	2.35	895	1.616	963	2.267
900	1.15	709	1.555	1108	2.5	945	1.583	1038	2.267
1000	1.13	758	1.515	1158	4.3	995	1.612	1113	2.433
1100	1.11	833	1.461	1208	3.1	1070	1.661	1163	3.1
1200	1.1	908	1.359			1145	1.777	1188	2.8
		983	1.307			1195	1.876		
		1033	1.303						
		1083	1.388						
		1158	1.467						
		1208	1.509						

Figure 4.3 shows α of each material as dependent on temperature. The folds in curves are due to the complex phase transformations. The magnitude of α seems to depend on the material in a certain order. The closer the powder metal is to AISI316L steel, the higher the α value is. 50/50 steel makes an exception. Between temperatures from approximately 600°C to 900°C the values of 50/50 steel are logically between the values of 75/25 steel and 25/75 steel by magnitude, but otherwise they are near the values of AISI316L steel and form a really noteworthy peak approximately at 1160°C. AISI316 steel has slightly lower values than the powder metal AISI316L.

To understand the figure 4.3 better, it is worthwhile comparing the graphs of 75/25 steel in Figure 4.1 and Figure 4.3 with each other. The higher the coefficient of thermal expansion of a material is during the process, the higher thermal strains the material has in the final state after cooling.

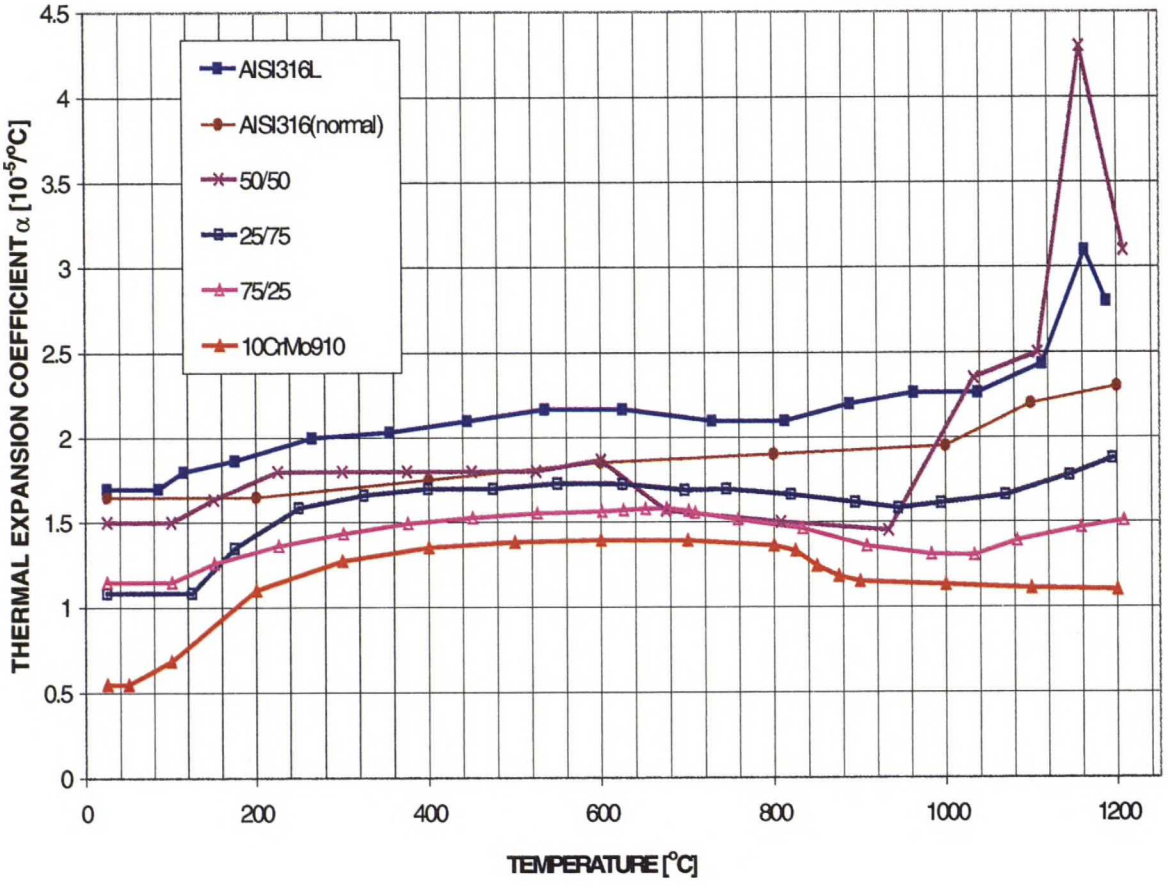

Figure 4.3 Coefficient of thermal expansion as a function of temperature for each of the materials used in the analyses.

4.2 Elastic Model

The metals studied have approximately linear elastic behavior at low stress levels and the Young's modulus or the modulus of elasticity (E), is constant. Elastic behavior means that the deformation is fully recoverable. When the load is removed, the specimen returns to its original shape. Under higher stresses after exceeding some limit they begin to have nonlinear inelastic behavior and theoretically the magnitude of E begins to decrease dramatically. Added to that, if some part of the deformation is non-recoverable, the behavior is referred to as plasticity (see Chapter 4.3).

The elastic and inelastic responses are, however, totally distinguished in this constitutive model by separating the deformation into recoverable (elastic) and non-recoverable (inelastic) parts. So, the assumption of an additive relationship between strain rates is used, when also thermal and creep strains are taken into account

$$\dot{\boldsymbol{\varepsilon}} = \dot{\boldsymbol{\varepsilon}}^{th} + \dot{\boldsymbol{\varepsilon}}^{el} + \dot{\boldsymbol{\varepsilon}}^{pl} + \dot{\boldsymbol{\varepsilon}}^{cr}, \tag{4.9}$$

where $\dot{\boldsymbol{\varepsilon}}$ is the total strain rate and the terms on the right hand side are thermal, elastic, plastic and creep strain rates, respectively. The elastic response is modeled with linear equation

$$\boldsymbol{\sigma} = \mathbf{D}^{el} : \boldsymbol{\varepsilon}^{el}, \tag{4.10}$$

where $\boldsymbol{\sigma}$ is the total stress tensor, $\mathbf{D}^{el}$ is the fourth-order elasticity tensor (equivalent to E in one dimension) depending on temperature but *not* on deformation. The term $\boldsymbol{\varepsilon}^{el}$ is the total elastic strain. This can be used, since elastic strains are known to be small enough.

In addition, every material in this study is isotropic, i.e. the behavior is similar in every direction. Equation (4.10) can also be given in the inverted component form

$$\begin{Bmatrix} \varepsilon_{11} \\ \varepsilon_{22} \\ \varepsilon_{33} \\ \gamma_{12} \\ \gamma_{13} \\ \gamma_{23} \end{Bmatrix} = \begin{bmatrix} 1/E & -\nu/E & -\nu/E & 0 & 0 & 0 \\ -\nu/E & 1/E & -\nu/E & 0 & 0 & 0 \\ -\nu/E & -\nu/E & 1/E & 0 & 0 & 0 \\ 0 & 0 & 0 & 1/G & 0 & 0 \\ 0 & 0 & 0 & 0 & 1/G & 0 \\ 0 & 0 & 0 & 0 & 0 & 1/G \end{bmatrix} \begin{Bmatrix} \sigma_{11} \\ \sigma_{22} \\ \sigma_{33} \\ \sigma_{12} \\ \sigma_{13} \\ \sigma_{23} \end{Bmatrix}. \tag{4.11}$$

In axisymmetric case Equation (4.11) is simplified to

$$\begin{Bmatrix} \varepsilon_{11} \\ \varepsilon_{22} \\ \varepsilon_{33} \\ \gamma_{12} \end{Bmatrix} = \begin{bmatrix} 1/E & -\nu/E & -\nu/E & 0 \\ -\nu/E & 1/E & -\nu/E & 0 \\ -\nu/E & -\nu/E & 1/E & 0 \\ 0 & 0 & 0 & 1/G \end{bmatrix} \begin{Bmatrix} \sigma_{11} \\ \sigma_{22} \\ \sigma_{33} \\ \sigma_{12} \end{Bmatrix}, \tag{4.12}$$

where σ_{11} is the radial stress, σ_{22} is the axial stress, σ_{33} is the circumferential stress and σ_{12} is the shear stress. ν is the Poisson's ratio, which defines the deformation in the directions perpendicular to the loading. The shear modulus, G, can be expressed as $G = E/2(1+\nu)$. (ABAQUS, 1998).

4.2.1 Young's Modulus and the Poisson's Ratio Based on the Literature

Only some values for 10CrMo910 steel and AISI316 steel are found in the literature. They are shown in Table 4.3.

Table 4.3 Young's modulus (E) and the Poisson's ratio (ν) of 10CrMo910 steel (ASM Specialty Handbook, 1994) and AISI316 steel (ASM Metals Handbook, 1990) as a function of temperature.

10CrMo910			AISI316		
T	E	ν	T	E	ν
[°C]	[GPa]		[°C]	[GPa]	
25		0.284	25	193	0.29
100	209	0.287	100	192	
200	202	0.291	200	185	
300	195	0.295	400	168.5	
400	187	0.299	600	151	
500	177	0.303	800	132	
600	167	0.307			

4.2.2 Measurements of the Young's Modulus

The tests for the determination of the Young's modulus are carried out using standard SFS-EN 10002 (1990). The stress is applied to the specimen at a steady pace and the strain is recorded. After that the stress is left to relax. Also the relaxation is recorded. The test specimens are cut out from a larger piece manufactured by HIP process. The tests are inaccurate at high temperatures. At lower temperatures the tests are more accurate, since it is possible to attach the strain gauge directly to the specimen. Figure 4.4 shows the curves for three different test series at temperature 20°C. The value 197 MPa (see Table 4.4a) is determined from those test series.

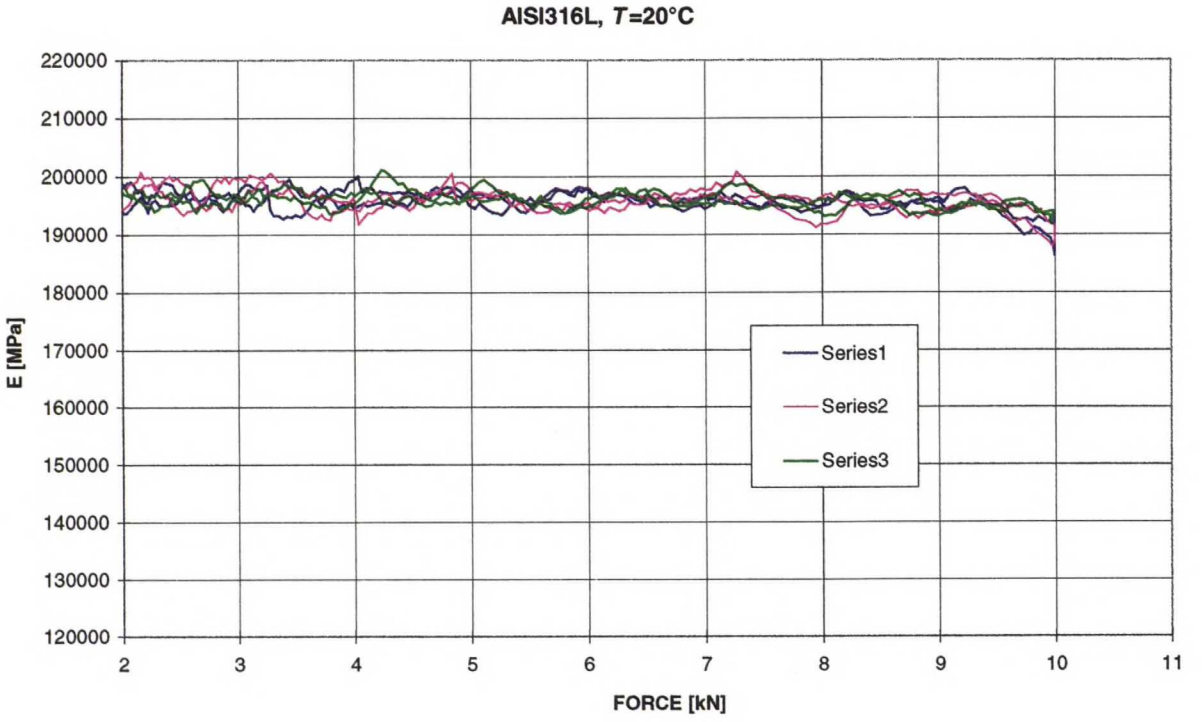

Figure 4.4 Curves of three different test series at room temperature RT. The material is AISI316L steel. The strain gauge is attached directly to the specimen.

The Poisson's ratio is not measured separately. The value 0.3 is used if no more accurate information is available.

4.2.3 Data of the Young's Modulus and the Poisson's Ratio

The data presented in Tables 4.4a-b is compiled of the measured data and the data from the literature (see the caption of Table 4.3). Some values are approximated. This data is further used in simulations.

Table 4.4a Young's modulus and the Poisson's ratio of 10CrMo910 steel, AISI316 steel and AISI316L steel.

10CrMo910			AISI316L			AISI316		
T	*E* (1)	*v*	*T*	*E*	*v*	*T*	*E* (2)	*v*
[°C]	[GPa]		[°C]	[GPa]		[°C]	[GPa]	
25	**214**	0.284	25	**197**	0.3	25	193	0.29
100	209	0.287	400	**176**	0.3	100	192	0.29
200	202	0.291	700	**150**	0.3	200	185	0.29
300	195	0.295	800	140	0.3	400	168.5	0.29
400	187	0.299	900	75	0.3	600	151	0.29
500	177	0.303	1000	30	0.3	800	132	0.29
600	167	0.307	1100	20	0.3	900	55	0.29
700	**142**	0.307	1200	10	0.3	1000	30	0.29
800	**60**	0.307				1100	20	0.29
900	**10**	0.307				1200	10	0.29
1000	*10*	0.307						
1100	*10*	0.307						
1200	*10*	0.307						

Bold font measured in this study

Italic letter interpolated/extrapolated data

Small font approximated

Table 4.4b Young's modulus and the Poisson's ratio of 75/25 steel, 50/50 steel and 25/75 steel.

75/25			50/50			25/75		
T	*E*	*v*	*T*	*E*	*v*	*T*	*E*	*v*
[°C]	[GPa]		[°C]	[GPa]		[°C]	[GPa]	
25	**200.7**	0.3	25	**200**	0.287	25	**196.7**	0.3
400	**171**	0.3	400	**180**	0.2945	400	**165**	0.3
600	**127**	0.3	700	**105**	0.2985	600	**149**	0.3
700	**94**	0.3	800	85	0.2985	700	**125**	0.3
800	**70**	0.3	1000	20	0.2985	800	**105**	0.3
1000	10	0.3	1100	15	0.2985	1000	30	0.3
1100	10	0.3	1200	10	0.2985	1100	20	0.3
1200	10							

Bold font measured in this study

Italic letter interpolated/extrapolated data

Small font approximated

Figure 4.5 shows the Young's modulus for every material used in simulations as a function of temperature. The curves are close to each other between temperatures RT and 400°C, after which the values diverge. No clear pattern is perceivable. At 800°C and above the values are in order by the material composition: 10CrMo910 steel has the lowest values and AISI316L has the highest values.

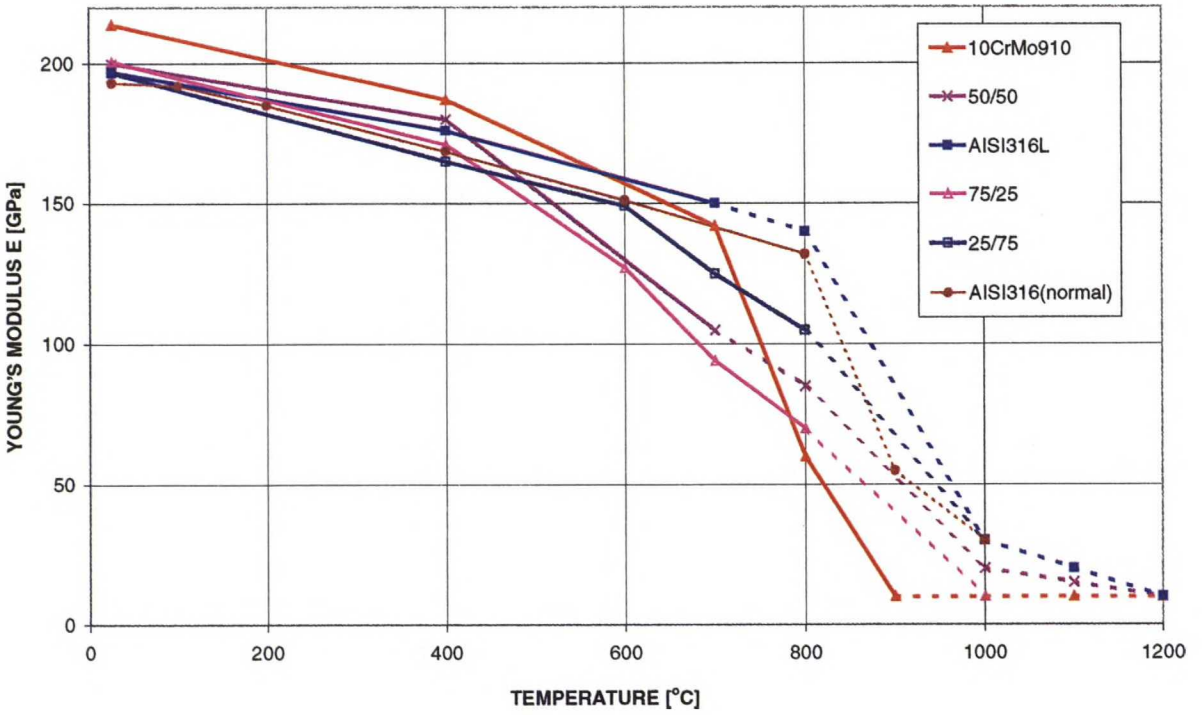

Figure 4.5 Young's modulus (E) of each material used in the simulations as a function of temperature. This figure is based on Tables 4.4a and 4.4b. The approximated values are connected by dashed lines.

4.3 Elasto-Plastic Model

The plastic behavior of a material is described by its yield point on the stress-strain curve and the yield hardening. Yield point is a certain point where the shift from elastic to plastic behavior occurs. To be more precise, the model is formulated in terms of

- the *yield surface*, which determines when the material no longer responds purely elastically at a particular state of stress.
- the *flow rule*, which defines the plastic deformation if the material point is no longer responding elastically.

- evolution laws that define the *hardening*: How the flow definitions are changed with plastic deformation.

A classical metal plasticity model based on the standard von Mises yield surface with associated plastic flow is used in this work. The standard von Mises yield surface means there is no volumetric plastic strain. Since only the deviatoric stress component affects the plastic deformation, it has to be defined next. The elastic volume change will be small since the elastic bulk modulus is quite large. A following simplification is justifiable (some problems may rise during the first few increments of the analysis, when all parts of the total strain are relatively large)

$$\varepsilon_{\text{vol}} = \text{trace}(\boldsymbol{\varepsilon}) \tag{4.13}$$

and, hence, the deviatoric strain is

$$\mathbf{e} = \boldsymbol{\varepsilon} - \frac{1}{3}\varepsilon_{\text{vol}}\mathbf{I}. \tag{4.14}$$

Then, the elasticity can be written in volumetric and deviatoric components as follows:

VOLUMETRIC

$$p = -K\varepsilon_{\text{vol}}, \tag{4.15}$$

where $p = -\frac{1}{3}\text{trace}(\boldsymbol{\sigma})$ is the equivalent pressure stress and K is the bulk modulus.

DEVIATORIC

$$\mathbf{S} = 2G\mathbf{e}^{el}, \tag{4.16}$$

where $\mathbf{S} = \boldsymbol{\sigma} + p\mathbf{I}$ is the deviatoric stress tensor and G is the shear modulus.

Equations (4.15) and (4.16) are written in terms of two temperature-dependent material parameters, since the elasticity is both linear and isotropic

$$K = \frac{E}{3(1-2\nu)} \text{ and } G = \frac{E}{2(1+\nu)}. \tag{4.17}$$

In associated flow plasticity models the direction of flow is the same as the direction of the outward normal to the yield surface. It is considered useful, since no sudden changes in the direction of the plastic strain rate at any point are predicted to take place during the analysis. Thus, *flow rule* is

$$d\mathbf{e}^{pl} = d\bar{e}^{pl}\mathbf{n}, \tag{4.18}$$

where $\mathbf{n} = \frac{3}{2}\frac{\mathbf{S}}{\bar{q}}$ is the outward normal vector.

$\bar{q} = \sqrt{\frac{3}{2}\mathbf{S}:\mathbf{S}}$ (von Mises equivalent stress) and $d\bar{e}^{pl}$ is the deviatoric part of the equivalent plastic strain rate (scalar). (ABAQUS, 1998). Since there is no volumetric plastic strain, the plastic strain component is hereafter in the text denoted by 'epsilon', ε^{pl}.

Von Mises stress (also termed the *effective stress*, *generalized stress* or *equivalent stress*) is in axisymmetric case

$$\bar{q} = \sqrt{\frac{1}{2}\left[(\sigma_{11}-\sigma_{22})^2 + (\sigma_{22}-\sigma_{33})^2 + (\sigma_{33}-\sigma_{11})^2 + 6\sigma_{12}\right]}. \tag{4.19}$$

4.3.1 Isotropic Hardening

The hardening in the model used in this work is isotropic. Isotropic hardening means that the yield surface changes size uniformly in all directions such that the yield stress increases as

plastic deformation occurs. It is a suitable model for problems with relatively large plastic strains without sharp and continuous reversals. The hardening behavior is defined for ABAQUS input by data points in $\bar{q}^Y$-$\tilde{\varepsilon}^{pl}$-T -space. The data points are obtained from the tensile strength tests explained in Chapter 4.3.3. ABAQUS then approximates the smooth stress-strain behavior of a material as a function of temperature with a series of straight lines joining the given data points. Because the first data pair must correspond to the onset of plasticity, the plastic strain must be zero in it at every given temperature.

The given data points define the yield function, which then again defines the *yield surface* and is written

$$f(\boldsymbol{\sigma}) = \bar{q}^Y\left(\tilde{\varepsilon}^{pl}, T\right), \tag{4.20}$$

where T is temperature, $\bar{q}^Y$ is the equivalent uniaxial yield stress and $\tilde{\varepsilon}^{pl}$ is the uniaxial equivalent plastic strain. The three-dimensional plastic behavior must correspond with the uniaxial plastic behavior:

$$\bar{q}^Y \dot{\tilde{\varepsilon}}^{pl} = \boldsymbol{\sigma} : \dot{\boldsymbol{\varepsilon}}^{pl}. \tag{4.21}$$

4.3.2 Tensile Properties Based on Literature

The tensile properties are taken from the literature only for the steel AISI316 (Table 4.5). $R_{0.2}$ is the stress where the plastic strain reaches the magnitude 0.2 % and it is often called the yield strength. $R_{1.0}$ gives correspondingly 1.0 % plastic strain and R_m is the rupture strength.

Table 4.5 Tensile values based on the literature for the steel AISI316 (ASM Metals Handbook, 1990).

AISI316		
T	$R_{0.2}$	R_m
(°C)	**(MPa)**	**(MPa)**
25	275	595
425	186	518
625	156	390

4.3.3 Yield and Tensile Strength Tests

The strength testing is carried out at room temperature (RT) and at elevated temperatures 400°C, 700°C, 800°C and 900°C, except for 75-25 and 25-75 materials at RT and 400°C, 600°C, 700°C and 800°C. The testing standard is SFS-EN 10 002-5 (1990) and the tensile test specimens used are flat bars similar to the ones used in some of the creep tests (Figure 4.9).

The force-displacement curves are measured using a ceramic high-accuracy extensometer to register the displacement. After exceeding the scale of the extensometer, the strain measurements are done from the testing machine pullrods. It is worth noticing that each material parameter is defined by only one test and the reliability of values at high temperatures is not very high. Figure 4.4 shows a stress-strain curve for the 75-25 steel at temperature 20°C. The mean time interval is 0.456 seconds and the whole test lasts for the duration of 17 minutes.

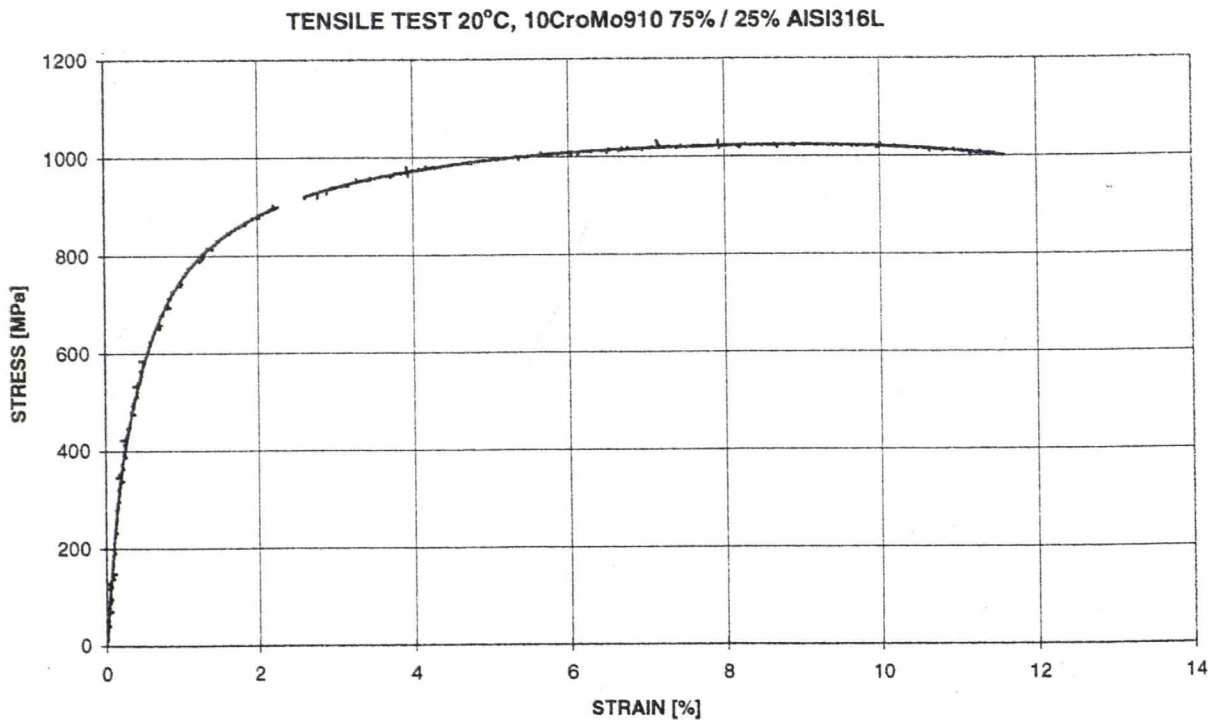

Figure 4.6 Registered stress-strain curve for the 75/25 steel at RT.

Tables (4.6a-f) and three figures (Figures 4.7a-c) show the tensile strength values $R_{0.2}$, $R_{1.0}$ and R_m as a function of temperature for each material further used in the simulations. They illustrate clearly the plastic behavior. Extrapolated values have been marked with dashed lines in the figures. At higher temperatures 75/25 steel is supposed to behave like 10CrMo910

steel, 25/75 steel and AISI316 steel are supposed to behave like AISI316L steel and 50/50 steel is supposed to behave in a way somewhere between. Remarkably, in general outline, AISI316L steel has the lowest tensile strength values below the temperature region of phase transformations. The more ferritic crystal structure an alloy has the more it strengthens - until somewhere between the proportions of 75/25 and 100/0 the values approach the ones of 10CrMo910 steel. The reason for this lies most probably in the interaction between carbides and a suitable proportion of austenite and ferrite (private conversation with Heikinheimo, 1999). It would be interesting to know the proportion for the highest tensile strength. Mainly, the alloys derive their strength from solid solution hardeners and precipitating phases, but carbides may provide limited strengthening directly through dispersion hardening or, more commonly, indirectly by stabilizing grain boundaries against excessive shear (ASM Superalloys, 1984).

Another basic feature is that the order of magnitude almost completely reverses in the region of phase transformation. Thus at temperatures over approximately 700°C AISI316L steel has the highest tensile strength values.

Table 4.6a Tensile properties for 10CrMo910 steel. The same formatting (explained under this table) is used in Tables 4.6a-f.

10CrMo910			
T **[°C]**	$R_{0.2}$ **[MPa]**	$R_{1.0}$ **[MPa]**	R_m **[MPa]**
25	**359**	**498**	**672**
400	**251**	**320**	**394**
700	**171**	**186**	**186**
800	**59**	**63**	**63**
900	**60**	*67*	**70**
1000	*16*		
1100	*14*	*18*	***18***
1200	*11*	14	19

Bold	measured in this study
Italic	interpolated/extrapolated data
Italic bold	interpolated from corresponding creep tests reported on this work
Small	approximated

Table 4.6b Tensile properties for 75/25 steel.

75/25			
T **[°C]**	$R_{0.2}$ **[MPa]**	$R_{1.0}$ **[MPa]**	R_m **[MPa]**
25	**577**	**817**	**1023**
400	**530**	**754**	**1010**
600	**395**	**490**	**497**
700	**174**	**197**	**197**
800	**69**	**82**	**82**
900	60	67	70
1000	16		
1100	14	18	18
1200	11	14	19

Table 4.6c Tensile properties for 50/50 steel.

50/50			
T [°C]	$R_{0.2}$ [MPa]	$R_{1.0}$ [MPa]	R_m [MPa]
25	478	703	943
400	402	589	861
700	191	227	240
800	117	134	140
900	87	96	98
1000	30	40	50
1200	15	20	24

Table 4.6d Tensile properties for 25/75 steel.

25/75			
T [°C]	$R_{0.2}$ [MPa]	$R_{1.0}$ [MPa]	R_m [MPa]
25	357	491	823
400	255	350	674
600	210	267	405
700	168	203	276
800	144	163	179
900	120	128	132
1000	50	60	65
1200	20	25	28

Table 4.6e Tensile properties for AISI316L steel.

AISI316L			
T [°C]	$R_{0.2}$ [MPa]	$R_{1.0}$ [MPa]	R_m [MPa]
25	**341**	**382**	**697**
400	**183**	**225**	**545**
700	**147**	**179**	**340**
800	**149**	**177**	**249**
900	**120**	**128**	**132**
1000	50	60	65
1200	20	25	28

Table 4.6f Tensile properties for AISI316 steel. The values not approximated are also shown in Table 4.5.

AISI316			
T [°C]	$R_{0.2}$ [MPa]	$R_{1.0}$ [MPa]	R_m [MPa]
25	275	317	595
425	186	221	518
625	156	198	390
700	147	179	340
800	149	177	249
900	120	128	132
1000	50	60	65
1200	20	25	28

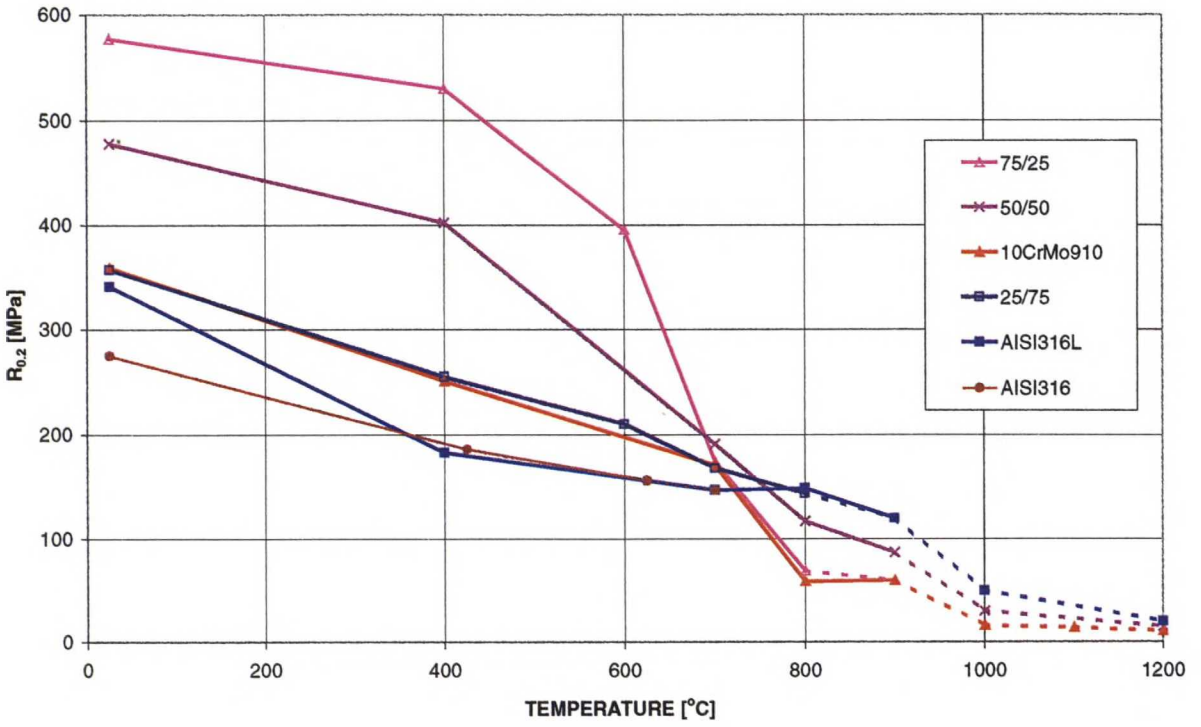

Figure 4.7a $R_{0.2}$ stress for each material as a function of temperature. The approximated or extrapolated points are connected by dashed lines.

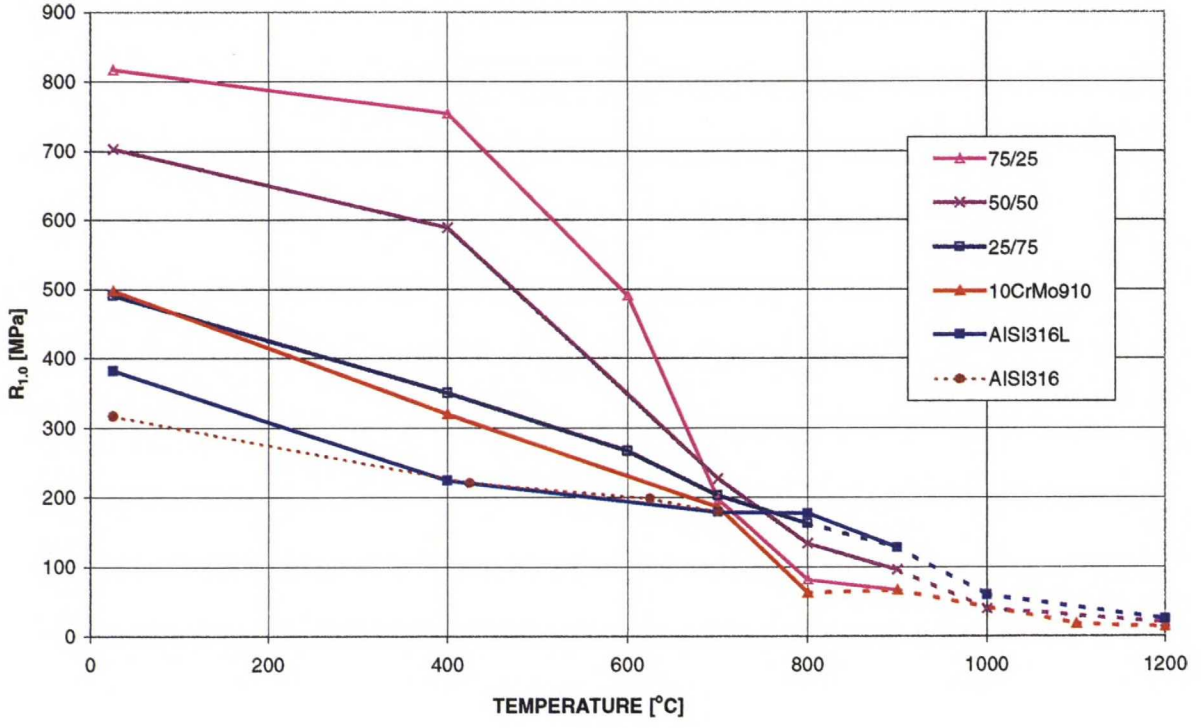

Figure 4.7b $R_{1.0}$ stress for each material as a function of temperature. The approximated or extrapolated points are connected by dashed lines.

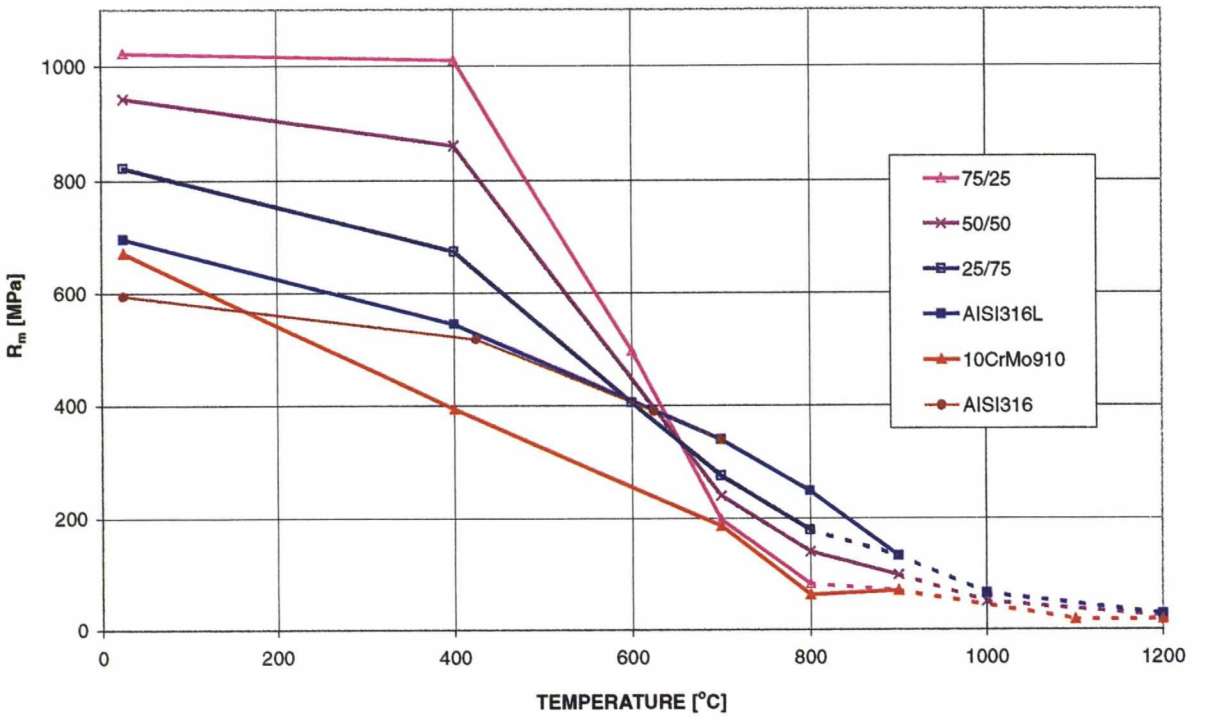

Figure 4.7c R_m stress for each material as a function of temperature. The approximated or extrapolated points are connected by dashed lines.

The data has to be converted from the nominal stress and the total nominal strain, which do not take the change of area into account, to the true stress and true plastic strain. This is done in the following manner:

Let S and l be the *current* cross-sectional area and the length of the specimen. Let S_0 and l_0 be the corresponding *initial* values. Then by the incompressible nature of the plastic deformation

$$l_0 S_0 = lS \Rightarrow S = S_0 \frac{l_0}{l} \tag{4.22}$$

and by the definition of stress

$$\sigma_{true} = \frac{F}{S} = \frac{Fl}{S_0 l_0} = \sigma_{nom}\left(\frac{l}{l_0}\right) = \sigma_{nom}\left(1 + \varepsilon_{nom}\right). \tag{4.23}$$

Because the concept of strain is the change of length in proportion to the current total length that is also continuously changing, the change of length must be divided into infinite small parts. It can be seen why the true strain is also called logarithmic strain.

$$\varepsilon_{true} = \int_{l_0}^{l} \frac{dl}{l} = \ln\left(\frac{l}{l_0}\right) = \ln(1+\varepsilon_{nom}) \,. \tag{4.24}$$

Finally the true plastic strain

$$\varepsilon_{true}^{pl} = \varepsilon_{true} - \varepsilon_{true}^{el} = \ln(1+\varepsilon_{nom}) - \frac{\sigma_{true}}{E} \,. \tag{4.25}$$

4.3.4 Tensile Data Used in the Simulations

Table 4.7 shows the actual values being entered to the input files of FEM simulations. The FEM program interpolates the plastic behavior linearly between the temperatures at which the tests are made. Those test temperatures are shown in the first column of each material in Table 4.7.

Table 4.7 Tensile values for the FEM simulations of each material used in the simulations.

10CrMo910		
T [°C]	σ [MPa]	ε^{pl}
25	355	0
25	360	0.00199
25	504	0.0099
400	247	0
400	252	0.00199
400	324	0.00991
700	167	0
700	172	0.00199
700	188	0.00992
800	54	0
800	59	0.00199
800	64	0.00993
900	55	0
900	60	0.00192
900	68	0.00975
1100	9	0
1100	14	0.00199
1100	18	0.00991
1200	8	0
1200	11	0.00199
1200	14	0.00992

75/25		
T [°C]	σ [MPa]	ε^{pl}
25	575	0
25	580	0.00197
25	828	0.00985
25	2051	0.12519
400	528	0
400	533	0.00197
400	765	0.00983
400	1910	0.15858
600	392	0
600	397	0.00197
600	497	0.00985
600	896	0.13705
700	170	0
700	175	0.00199
700	199	0.0099
700	365	0.19086
800	64	0
800	69	0.00199
800	83	0.00993
800	128	0.19086
900	55	0
900	60	0.00199
900	68	0.00991
1100	9	0
1100	14	0.00199
1100	18	0.0991
1200	8	0
1200	11	0.00199
1200	14	0.00992

50/50		
T [°C]	σ [MPa]	ε^{pl}
25	475	0
25	480	0.00198
25	712	0.00986
25	2410	0.21109
400	399	0
400	404	0.00198
400	597	0.00987
400	1477	0.21093
700	137	0
700	164	0.00103
700	192	0.00236
700	221	0.00686
700	237	0.01657
700	385	0.18695
800	72	0
800	101	0.00121
800	130	0.00663
800	142	0.02595
800	197	0.1461
900	55	0
900	83	0.00141
900	99	0.01522
900	133	0.14188
1000	25	0
1000	30	0.00198
1000	41	0.00989
1200	10	0
1200	15	0.00199
1200	20	0.00991

Table 4.7 continued

25/75		
T [°C]	σ [MPa]	ε^{pl}
25	353	0
25	358	0.00199
25	497	0.00989
25	3473	0.28245
400	251	0
400	256	0.00199
400	354	0.0099
400	1615	0.22133
600	206	0
600	211	0.00199
600	270	0.00991
600	1011	0.29702
700	164	0
700	169	0.00199
700	205	0.0991
700	483	0.25465
800	139	0
800	144	0.0199
800	165	0.00992
800	270	0.17975
900	115	0
900	120	0.00198
900	130	0.0099
1000	45	0
1000	50	0.00199
1000	61	0.00991
1200	15	0
1200	20	0.00198
1200	25	0.00989

AISI316L		
T [°C]	σ [MPa]	ε^{pl}
25	337	0
25	342	0.00199
25	387	0.00991
25	3495	0.47696
400	179	0
400	184	0.00199
400	228	0.00992
400	1927	0.34673
700	111	0
700	139	0.00157
700	168	0.00605
700	198	0.01593
700	229	0.02861
700	298	0.06567
800	112	0
800	141	0.00099
800	155	0.00289
800	170	0.00695
800	201	0.01974
800	236	0.04768
800	597	0.36038
900	87	0
900	101	0.00085
900	116	0.00165
900	132	0.01804
900	239	0.26571
1000	45	0
1000	50	0.00199
1000	61	0.00991
1200	15	0
1200	20	0.00198
1200	25	0.00989

AISI316		
T [°C]	σ [MPa]	ε^{pl}
25	271	0
25	276	0.00199
25	321	0.00991
425	182	0
425	187	0.00199
425	224	0.00992
625	151	0
625	156	0.00199
625	200	0.00992
700	111	0
700	139	0.00157
700	168	0.00605
700	198	0.01593
700	229	0.02861
700	298	0.06567
800	112	0
800	141	0.00099
800	155	0.00289
800	170	0.00695
800	201	0.01974
800	236	0.04768
800	597	0.36038
900	87	0
900	101	0.00085
900	116	0.00165
900	132	0.01804
900	239	0.26571
1000	45	0
1000	50	0.00199
1000	61	0.00991
1200	15	0
1200	20	0.00198
1200	25	0.00989

4.4 Rate-Dependent Metal Plasticity

Since the structure is exposed to a continuous load at high temperatures, the importance of rate-dependent plasticity becomes quite obvious especially for rate-sensitive materials such as metals, which are studied in this project. This material behavior is generally known as creep.

In the constitutive model of this study the creep and plasticity occur simultaneously. Especially as both are isotropic, their interaction can properly be handled and a coupled system of constitutive equations integrated. However, the material model is not unified in a sense that both plastic and creep deformations are approached separately.

4.4.1 Strain Hardening

The uniaxial power-law creep model is chosen. It is relatively simple, nonetheless adequate to fit experimental data. Because the stress state varies during the analysis, the strain-hardening version of the power-law creep is used. It is usually introduced in the form

$$\dot{\bar{\varepsilon}}^{cr} = \left(A\bar{q}^{n}\left[(m+1)\bar{\varepsilon}^{cr}\right]^{m}\right)^{\frac{1}{m+1}}, \tag{4.26}$$

where

$\dot{\bar{\varepsilon}}^{cr}$ is the uniaxial equivalent creep strain rate, $\dot{\bar{\varepsilon}}^{cr} = \sqrt{\frac{2}{3}\dot{\varepsilon}^{cr} : \dot{\varepsilon}^{cr}}$,

$\bar{\varepsilon}^{cr}$ is the equivalent creep strain,

$\bar{q}$ is the uniaxial equivalent deviatoric stress (von Mises) and

A, n and m are defined by the curve-fitting program and are all dependent on the temperature (ABAQUS, 1998).

4.4.2 Creep Tests

Despite the fact that complex non-steady stress and temperature conditions are encountered during the HIP process, the rate-dependent behavior of all the materials in this study is based on uniaxial test data. In fact, most of the results reported in fundamental studies of creep have been obtained using tensile creep and stress-rupture equipment. In addition, the testing for this

work is of the most typical kind, involving the application of a constant load at a constant temperature. The author was involved with the creep tests during three months in 1999. The tests are made with all the 5 powder materials. Exactly the same parameter values are given both for AISI316L powder steel and AISI316 steel. The standard followed is prEN 2002 (AECMA Standard, 1993).

In order to meet the high standards of accuracy and reproducibility, careful consideration must be given to the following aspects of the testing system (Loveday, 1982):

1. the machine frame and loading arrangement
2. the loading bars and specimen grips
3. the specimen design and manufacture
4. the furnace and temperature control system
5. the extensometry and displacement measuring equipment
6. the specimen environment
7. the laboratory environment

These aspects are briefly considered next, not precisely in the same order.

MACHINE FRAME

The testing for this work is conducted at temperatures ranging from 600°C to 1100°C. For the testing at 900°C and below standard creep testing machines are used. At temperatures above that, tests are done with a vacuum furnace fitted on a tensile testing machine. The standard creep machine used is a 20 kN dead-weight testing machine (maximum application of load is 20 kN) with a lever ratio of 1 : 10 (Figure 4.8). The most simple, and one of the most accurate ones, method of applying the load is to make use of the force exerted by a known mass on a stationary support. Using a mechanical lever is one way of amplifying that force. A major difficulty is the change in effective lever ratio of the beam with changes in its angular position. This source of inaccuracy is taken care by an automatic beam leveling system. The loading resolution is 1 N, meaning 10 N or approximately 0.6 MPa stress in the specimen with a cross-section of approximately 18 mm^2.

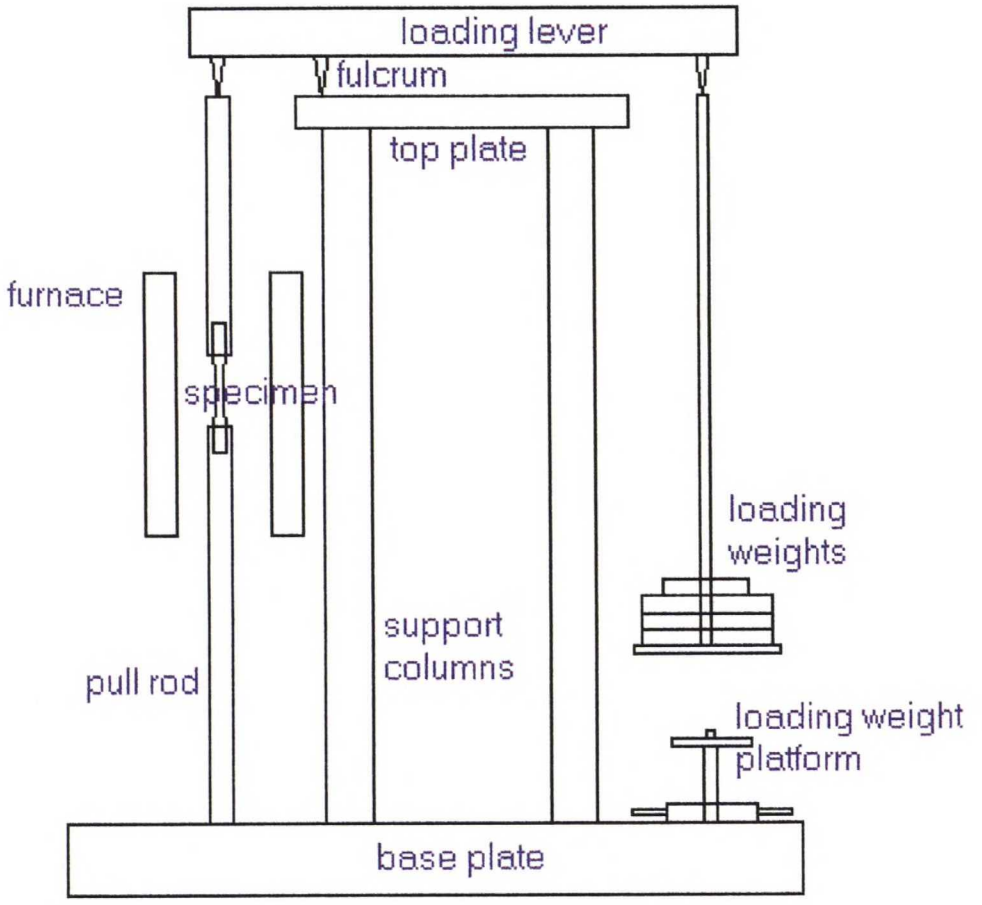

Figure 4.8 Standard creep testing machine.

SPECIMENS

Two types of specimens are used: A rectangular cross section bar (Figure 4.9) with pin jointed grip ends (6x3 mm^2, parallel length 30 mm) better suited for the vacuum furnace and a proportional round (∅ 10 mm) test piece (Figure 4.10). The round specimens are threaded and screwed onto the loading bar adapters, while the flat shaped bars are attached to the grips with a pin. Every test specimen is cut out from a larger piece manufactured by HIP process.

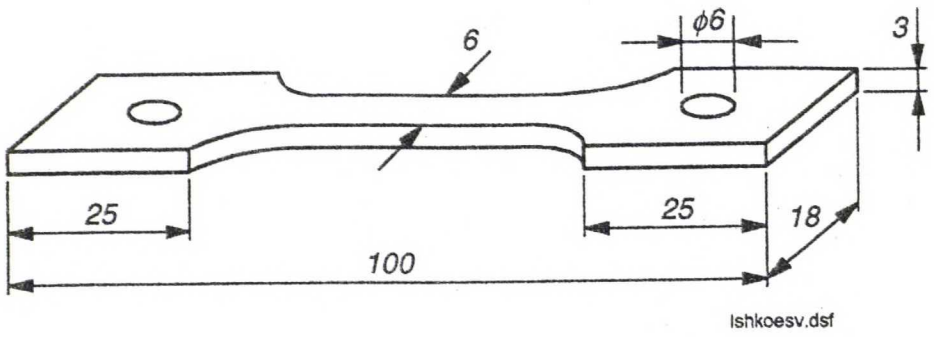

Figure 4.9 Rectangular cross section (bar) test specimen. Dimensions are in millimeters.

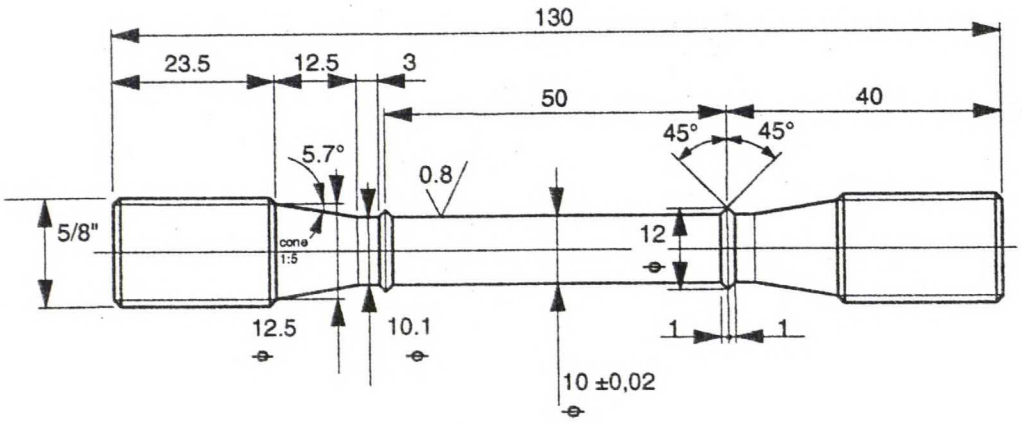

Figure 4.10 Round test specimen. Dimensions are in millimeters unless otherwise indicated.

FURNACE AND TEMPERATURE CONTROL SYSTEM

The requirements when considering temperature control are in general

1. a constant uniform temperature along the specimen gauge length,
2. an adequate thermal response (rapid heating and cooling with minimum overshoot, but small thermal fluctuations after reaching the test temperature) and
3. right type of temperature sensors (especially considering the temperature range).

The specimens are heated by electrically heated resistive furnaces, which are suitable for a conventional creep test with their slow thermal response. They have heating elements in three zones, with possibility to separately tune in and control each one. The loading bar openings are thoroughly insulated with glass fiber to ensure constant temperature over the specimen gauge length and an accurate thermal response. The thermal insulation has to be done without

restricting the loading bar and extensometer movements (see below "The extensometry and displacement measuring equipment"). The temperature measurement is done with type R and type N thermocouples attached to the specimen surface with ceramic paste and insulated wire (Annual Book of ASTM Standards, 1991). Two of the thermocouples record test temperatures and the third and middlemost is controlling the furnace. All the thermocouples are calibrated to the test temperature prior to the testing. The test temperature is reached by first setting the controller just below it to avoid overshoot and offsets in the temperature gradient over the specimen length. The heating zones are after temperature stabilization tuned for minimum gradient over the specimen length, and the final test temperature is set.

All the above-mentioned arrangements still have to enable easy access to the specimen.

EXTENSOMETRY AND DISPLACEMENT MEASURING EQUIPMENT

Two types of displacement measurements are conducted. In both cases extensometers have to be placed outside the furnace. For the tests conducted with round specimens two separate displacement measurements from both sides of the specimen give reliability to produced creep curve. This is done with yokes clamped directly onto the specimen upper and lower ridges. Thin rods attached to the yokes transfer the strain between ridges outside the furnace.

The flat section specimens for their part have to be measured indirectly from the loading bar displacement. It is however assumed that all the displacement (creep) is accumulated in the specimen gauge length. The error is considered negligible since the attachment pins have shown no indication of deformation and the initial, instant displacement, though recorded, is not included in the reported creep curve.

LOADING ARRANGEMENT

Before the actual loading the temperature is left to be stabilized for a while (reported as "soaking time", usually about 2 h). The loading is done manually and proceeds as follows:

- the data acquisition is started
- a small load (usually 5-10 kN) is applied to straighten the loading bars and fittings

- the displacement transducers are adjusted to zero value
- the loading weight platform is raised underneath the loading tray
- the load is applied (still backed up by the loading weight platform)
- the loading weight platform is lowered in a steady pace (loading complete in about 10-20 seconds)
- the initial elongation is documented
- the lever is adjusted to a horizontal position
- the test is running

The data acquisition software records displacements and temperatures at given time intervals. In the case of direct displacement measurement the testing machine is set to automatic mode, enabling automatic lever adjustment. In the case of plate specimens the lever has to be adjusted manually when the loading tray threatens to meet the loading weight platform. This also makes some data manipulation necessary, since the displacement measurement is directly connected to the loading bars. This might cause some minimal fluctuations in the load level (and also temperature level in some test, when the insulation moves) during the test. The test is ended when the specimen reaches its breaking point or all the necessary information for this project is gained.

PROBLEMS AND ERROR SOURCES IN THE TESTING PROCEDURE

There are a few problems in the testing procedure. The thermocouples and extensometers used are installed manually for every single test and in some tests a thermocouple has a tendency to detach from the specimen surface and extensometers occasionally stick. The soaking times are sometimes over 10 hours, when the temperature does not seem to stabilize. There are also some small quality problems with the specimen: Although the specimen dimensions fulfill certain criteria, there is indication of warping in the plate specimens. The quality of round bars is better, because their cross-section is axisymmetric and not so vulnerable to the machining processes.

The loading of the creep machine gives the most problems, especially in the case of plate specimens. Testing machines used belong to the so called constant load category, where for example the effect of thermal expansion and necking (reduction in area due to tensile stress)

on stresses is not taken into consideration. It is essential to recognize that the creep properties are being considered in relation to the initial specimen dimensions and that the stress quoted is always the initial stress applied to the specimen. Let us have a test of AISI316L steel (900°C, 40 MPa) as an example:

When the temperature has reached the test level, the actual area of the specimen's cross section is larger than before the heating. Let S_1 and σ_1 be the cross-sectional area and the stress before the heating and S_2 and σ_2 be the correspondent values at the final test temperature level. Let F be the force applied to the specimen.

$$\alpha = 23 \cdot 10^{-6} / ^{o} C \text{ and } \Delta T = 900^{o} C$$

$$S_2 = (1 + \alpha \cdot \Delta T)^2 S_1 \approx (1 + 2\alpha\Delta T) S_1 \approx 1.0414 S_1 \tag{4.27}$$

$$\Rightarrow \sigma_2 \approx \frac{F}{1.041 S_1} \approx 0.96\sigma_1$$

Thus the tensile stress is approximately 4 % lower than at the room temperature due to the thermal expansion.

The nominal strain is converted to the true strain in the data of these tests. By the incompressible nature of the plastic deformation, the cross-sectional area is not constant. Therefore, the true stress would be after two hours of loading (see Equation (4.23)):

$$\sigma_{true} = \sigma_{nom}(1 + \varepsilon_{nom}) = \sigma_{nom}(1 + 0.0145) \approx 1.01\sigma_{nom} \tag{4.28}$$

The true stress is thus higher than the nominal one. When comparing Equations (4.27) and (4.28), it can be seen that the effect of the incompressible nature of the plastic deformation is thus inverse to the effect of the thermal expansion on stress.

The necking is highly localized thinning under tensile load as the material fails. Its effect on stresses is even harder to judge and not so important in these creep tests, which do not focus on the material failure mechanisms.

4.4.2.1 Measured Creep Curves

The acquired data consists of time readings, one or two displacement readings and temperature readings. The time interval is set according to expected test duration and creep rate, normally within 30-60 seconds to few minutes for tests with small strain rates. Some tests have up to a few thousand data points. For the curve fitting, only strain as a function of time is needed. The first value of both magnitudes has to be zero, and the strain is *true strain*, which is explained in Chapter 4.3.3. In every test temperature t–ε -curves in two different stresses are needed. All the curves adopted to the fitting are shown in Figures 4.11-16 The material is mentioned first in the legend, then the corresponding stress.

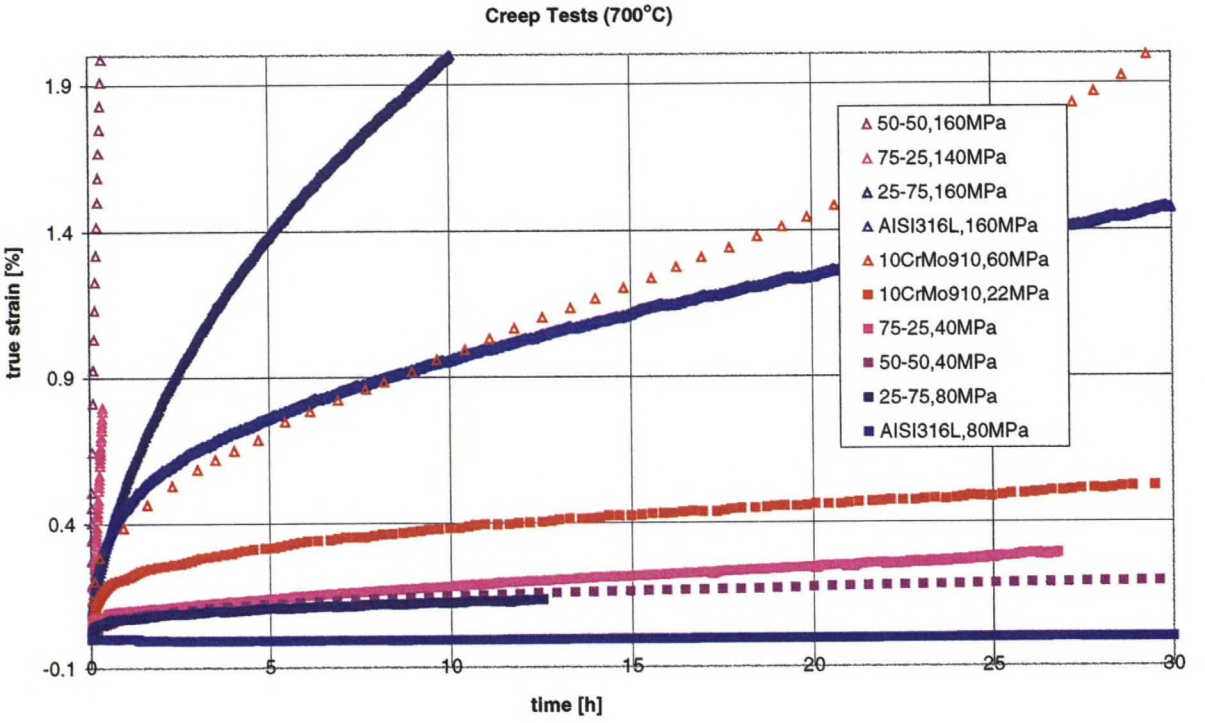

Figure 4.11 Creep strain as a function of time at 700°C. Two tests with different load levels are carried out for each material tested.

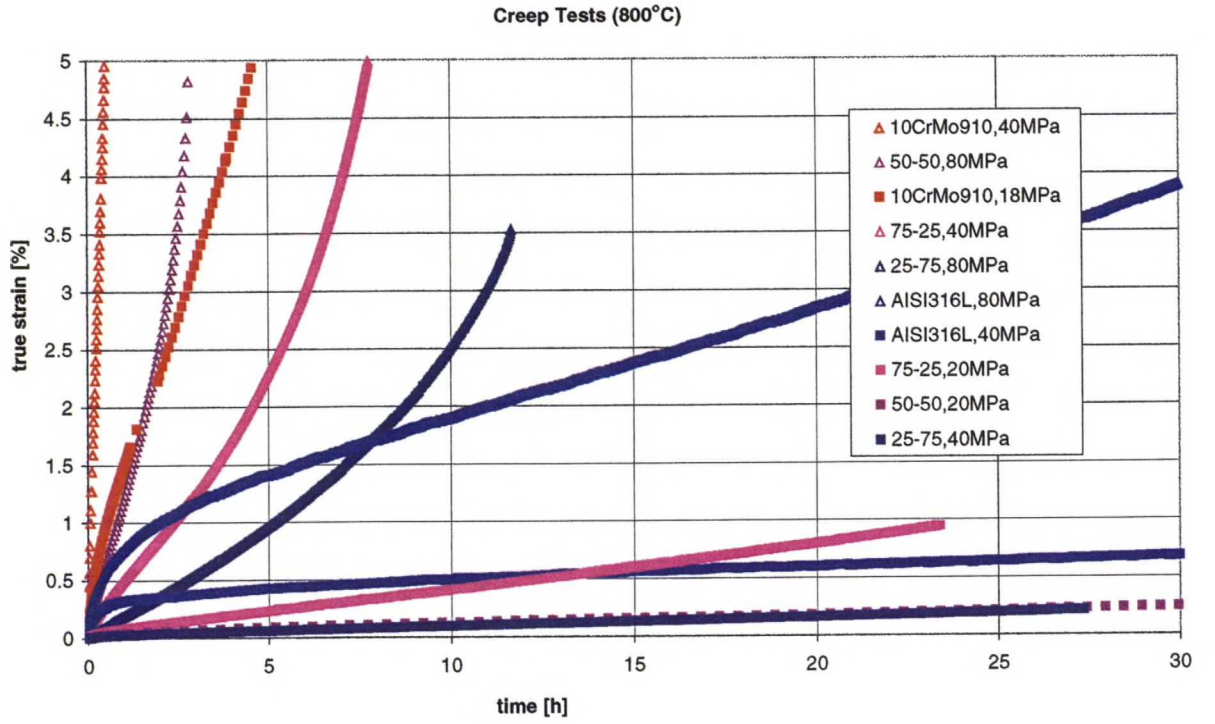

Figure 4.12 Creep strain as a function of time at 800°C. Two tests with different load levels are carried out for each material tested.

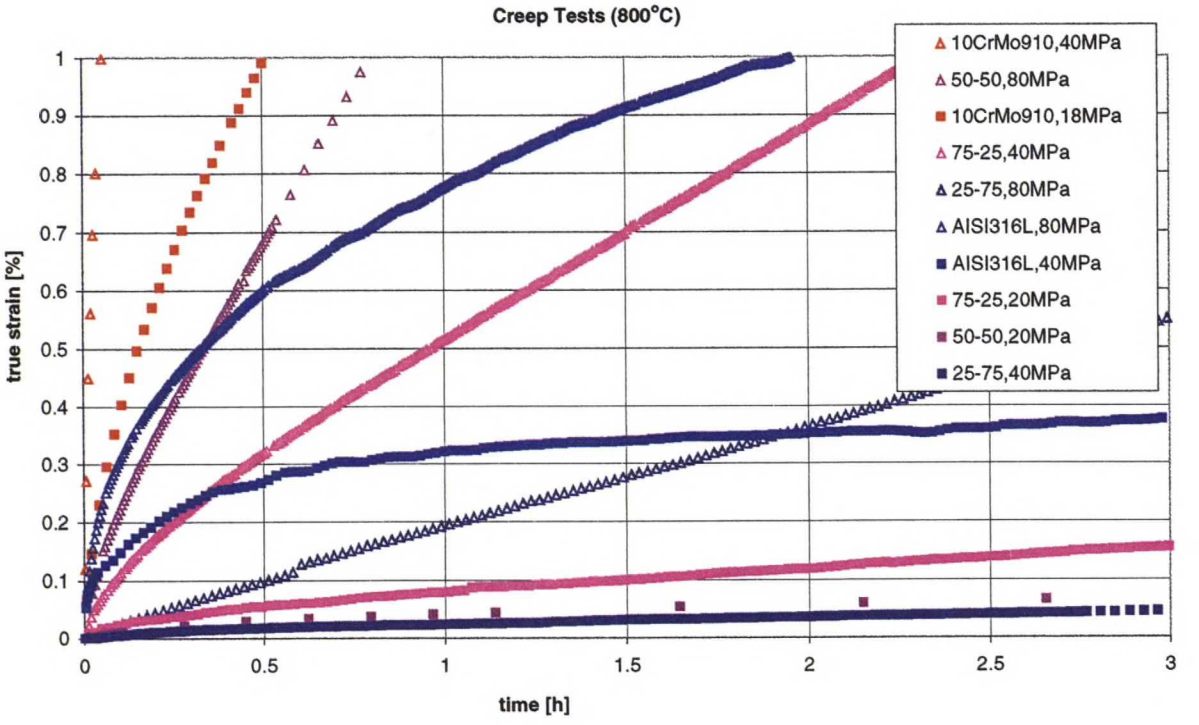

Figure 4.13 Creep strain as a function of time at 800°C. Two tests with different load levels are carried out for each material tested. Time scale is the first three hours of the tests.

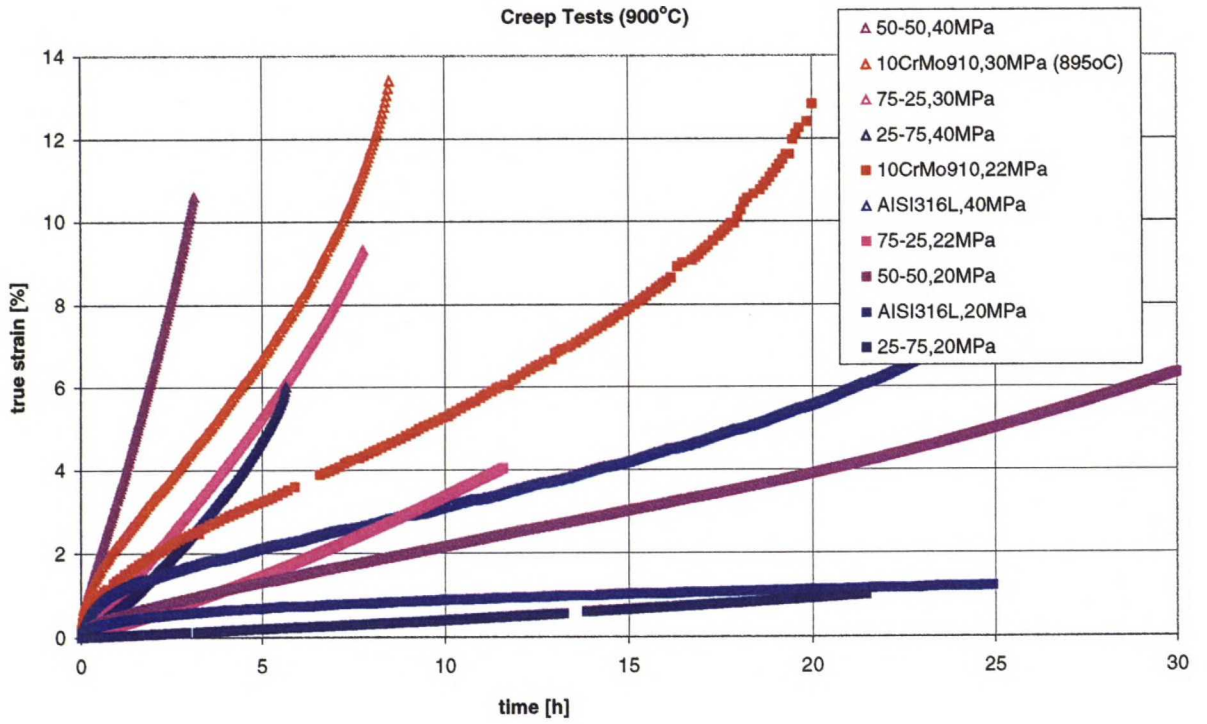

Figure 4.14 Creep strain as a function of time at 900°C. Two tests with different load levels are carried out for each material tested

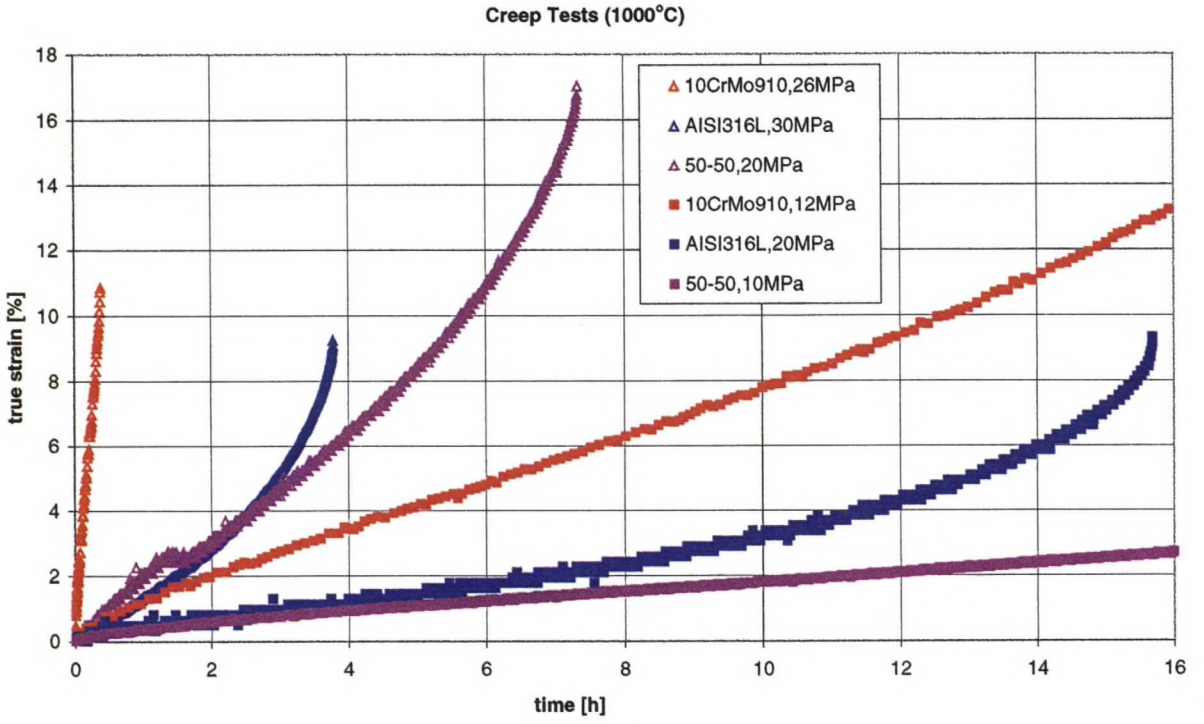

Figure 4.15 Creep strain as a function of time at 1000°C. Two tests with different load levels are carried out for 10CrMo910 steel, AISI316L steel and 50/50 steel.

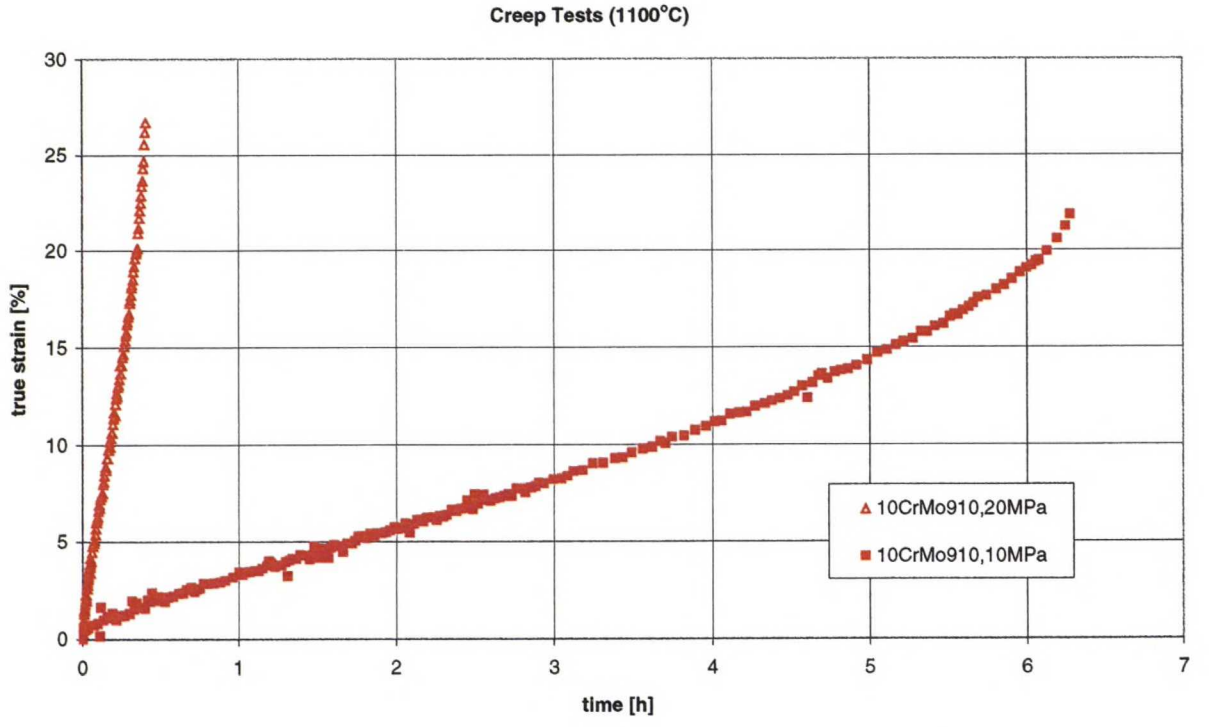

Figure 4.16 Creep strain as a function of time at 1100°C. Two tests with different load levels are carried out for 10CrMo910 steel.

Based on the creep test results (Figures 4.11-16), a couple of things are worth mentioning: First of all, the more the material has 10CrMo910 powder metal, the higher secondary (minimum) strain rate it has. This shows a clear tendency at every test temperature. Secondly, only 10CrMo910 steel and AISI316 steel have a clear phase of primary creep. On average, this phase includes the first two hours of creep, which makes the situation more complicated particularly for the simulation of hot isostatic pressing process, where these first two hours are the essential ones.

4.4.3 Curve Fitting

The curve fitting for this study is done with a computer program CURVEFIT by Santaoja (1996) which utilizes Levenberg-Marquardt method. This program emphasizes every curve equally in the fitting. It is also independent of the number of data points used or the number of creep curves. It does not process the tertiary phase of creep and that is why the data of each test is cut before the tertiary creep or at the latest after a few hours.

It uses the following uniaxial form of the strain hardening model, which differs from the one used by FEM-program and introduced in Chapter 4.4.1:

$$\dot{\varepsilon}^{cr} = \dot{\varepsilon}^{cr}_{\text{ref}} \left(\varepsilon^{cr}\right)^{-m^*} \left(\frac{\sigma}{\sigma_{\text{ref}}}\right)^{n^*}, \tag{4.29}$$

where ε^{cr} is the creep strain as a function of time from the acquired data and σ is the stress applied in the test. $\dot{\varepsilon}^{cr}_{\text{ref}}$ is the reference strain rate and σ_{ref} is the reference stress used to make the term to power n^* dimensionless.

First the value of the reference stress is fixed between the two stresses in which the tests were run and then the values of the other material parameters are solved by CURVEFIT. After that they have to be converged to the material parameters in Equation (4.26) by the conversion expressions

$$m = -\frac{m^*}{1+m^*}, \tag{4.30}$$

$$n = \frac{n^*}{1+m^*} \text{ and} \tag{4.31}$$

$$A = \left[(m+1)^{\frac{-m}{m+1}} \left(\frac{\sigma_0}{\sigma_{ref}} \right)^{n^*} \dot{\varepsilon}_{ref}^{cr} \right]^{m+1} . \tag{4.32}$$

σ_0 = 1 in these test (Saarenheimo et al., 1999).

NUMERICAL EXAMINATION OF THE CREEP MODEL

The validity of the creep model (Equation (4.26)) is controlled by a single-element model. A creep test is simulated with one cubic 8-node element under constant tensile stress and in constant temperature. The creep strain curve of the analysis is then compared to the actual strain curve of the corresponding test. The strain curves of the single element model are also compared to the corresponding fitting curves in order to be convinced that ABAQUS is using the mathematical model correctly. They found out to be very similar to each other. Figure 4.17 shows the real strain curve of AISI316L steel at 700°C and under 160 MPa pressure and its fitting curve. Figure 4.18 shows a simulated creep strain curve of the single-element model with the same material, temperature and stress. Only the first three hours are simulated.

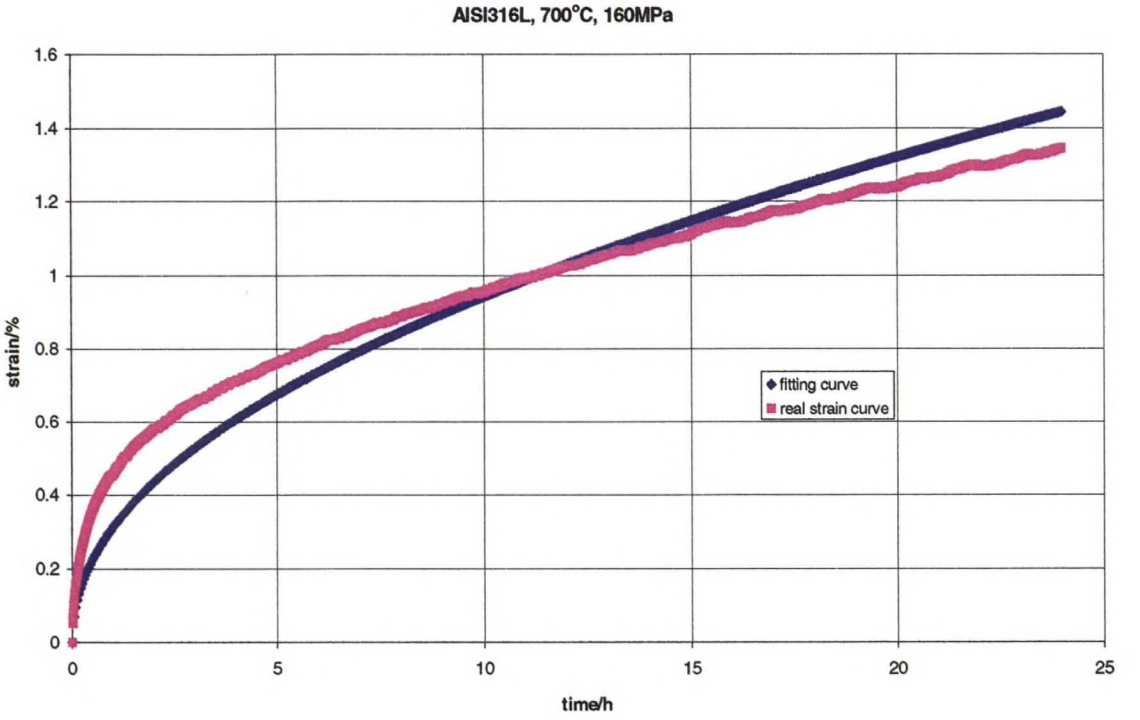

Figure 4.17 Comparison between the real creep strain rate curve of AISI316L steel at 700°C and under pressure of 160 MPa and the correspondent fitting curve.

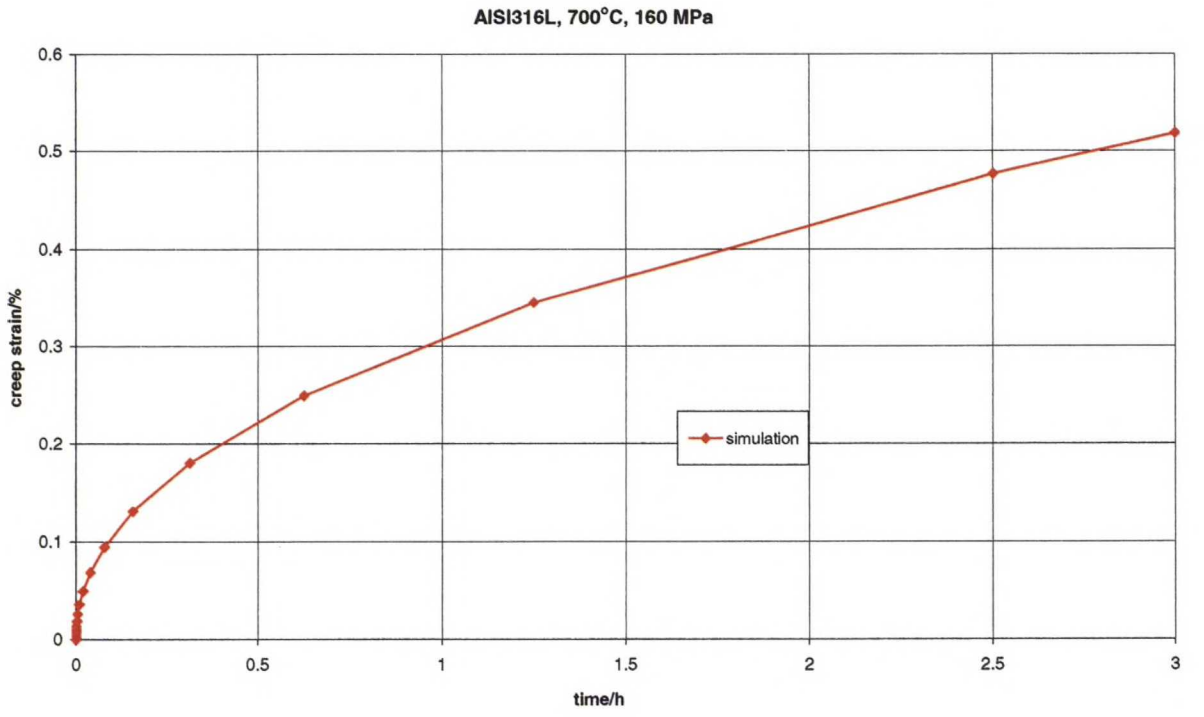

Figure 4.18 Creep strain curve of the analysis of a single-element model. The material, temperature and stress are same as in Figure 4.17.

Two evident problems arose, while analyzing the single-element model. First of all, the curve fittings are done for a too long time period instead of concentrating on the first two hours. In the base materials, especially in AISI316L steel, the very distinct primary phase of the creep is not taken sufficiently into account, as can be seen in Figure 4.17. The creep strain rate is underestimated during the primary creep phase and overestimated during the secondary phase. The difference in behavior of the materials can be seen, when comparing Figures 4.12 and 4.13. The order of magnitude is different during the first three hours than after 10 h for example. Secondly, the rate-dependent behavior is not sensible between the test temperatures, especially when it changes dramatically between these two adjacent temperatures. The minimum creep strain rate should increase with the rise of temperature, unless a different and an exceptional behavior is proven. A sufficient approximation would be interpolating linearly the minimum creep strain rate as a function of temperature between two measured data points. But when interpolating linearly the creep parameters, as ABAQUS does, and inserting them to a non-linear partial differential equation, the strain can be totally unexpected and different from the real behavior. This error is demonstrated by simulating a creep test at 750°C and under the pressure of 80 MPa (Figure 4.19). In the simulation at 750°C, the creep strain is 2636 % after three hours. Thus, the element length is over 27 times the initial length. To show how ABAQUS interpolates the parameters, the same simulation is run with parameters interpolated by the user (Figure 4.20). The curve in Figure 4.20 is similar to the curve in Figure 4.19. In fact, the creep strain values of both simulations are equal by magnitude, which practically proves, that the ABAQUS program interpolates the creep parameters linearly as a function of temperature between two known parameter sets.

Figure 4.21 shows how the behavior changes as a function of temperature when the temperature is lowered linearly as a function of time but the stress remains constant. This problem is most evident with AISI316L, since the viscoplastic behavior of that material is quite extraordinary at 700°C and under 80 MPa. However, the kind of stepwise curve shown in Figure 4.21 hardly has any explanation based on real material properties. The behavior is sensible near 900°C, but after approximately 1.3 hours (while approaching 750°C) the deformation becomes unrealistically high, even though the stress remains constant. The simulation was ended due to numerical problems after approximately 1.7 hours of simulation time (27543 time increments).

The problem concerned above is evident in AISI316L steel. Its behavior between 700°C and 800°C is troublesome also otherwise. In the creep tests, there was almost no creep deformation in 700°C under the lower testing stress. The unrealistically high strain values within a certain small temperature range and in a small area does not affect appreciably the analysis with the whole model. Energy balance of every FEM analysis is monitored and no sudden energy leap is detected.

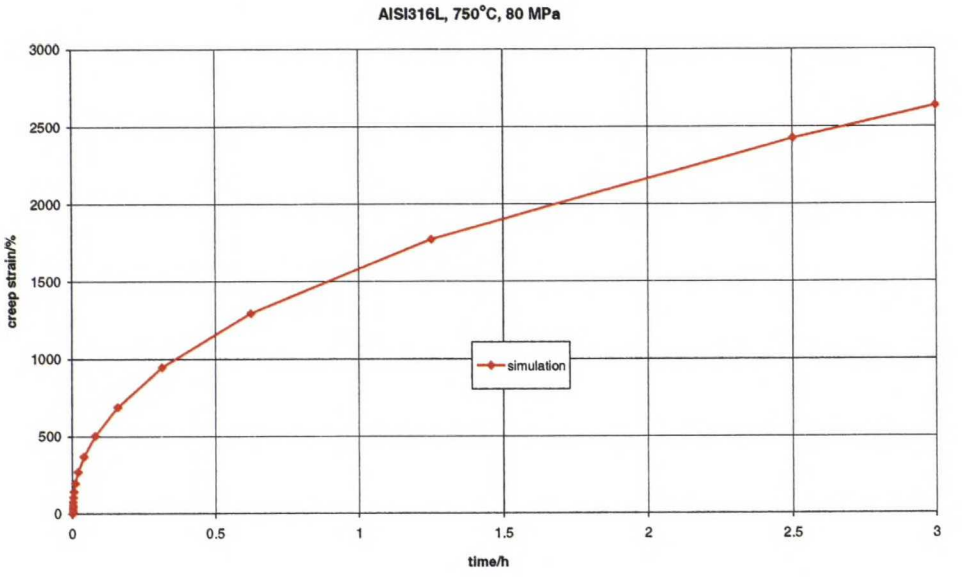

Figure 4.19 Equivalent creep strain of the single element (AISI316L steel) under 80 MPa tensile stress and at temperature of 750°C.

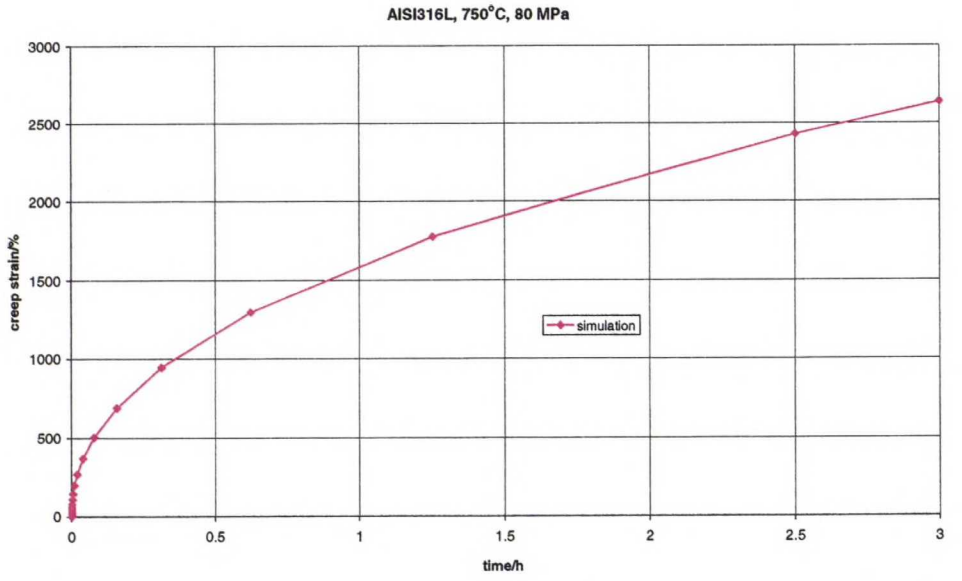

Figure 4.20 Equivalent creep strain of the single element (AISI316L steel) under 80 MPa tensile stress and at temperature of 750°C. The creep parameters for 750°C are interpolated linearly as a function of temperature by the user.

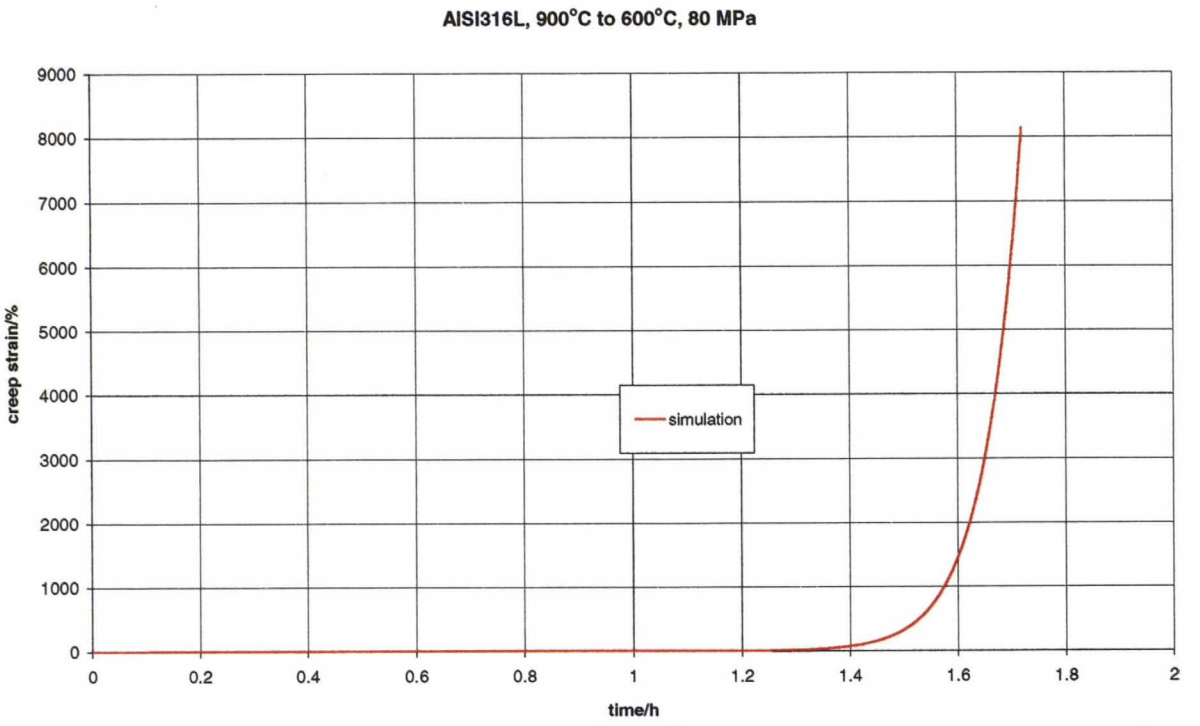

Figure 4.21 Equivalent creep strain of the single element (AISI316L steel) under 80 MPa tensile stress and with a linear temperature transient from 900°C to 600°C during a time interval of 10800 seconds (3 hours). The FEM analysis is ended after approximately 1.7 hours.

4.4.4 Creep data

Tables 4.8 and 4.9 show the creep parameters for FEM analyses derived from the test data by curve fitting. The information given in tables does not cover the whole temperature range for the finite element analyses. The values for the parameters outside the temperature range of the tests has to be extrapolated. At the room temperature (25°C), the value of the parameter A is set to be 10^{-4} times the A of the next temperature (the lowest test temperature for the material in question). It is then assumed to be linearly dependent on the temperature between those two points. The values of n and m at the room temperature are set to be equal to the value at the lowest test temperature of the corresponding material. The values of every creep parameter at higher temperatures outside the range are assumed to be equal to the ones at the highest test temperature.

Table 4.8 Creep parameters from the test data of 10CrMo910 steel and AISI316L steel (AISI316 steel has equal values to AISI316L steel values).

	10CrMo910			AISI316 and AISI316L		
T	*A*	*n*	*m*	*A*	*n*	*m*
25	4.5357E-13	1.7053	-0.3883	8.5879E-12	1.0326	-0.6558
600	4.5357E-09	1.7053	-0.3883	8.5879E-08	1.0326	-0.6558
700	1.2427E-07	1.2232	-0.452	1.5504E-17	5.586	-0.53365
800	1.0085E-09	2.7653	-9.8383E-04	3.9467E-08	1.7228	-0.56034
900	5.7879E-09	1.968	-4.9267E-02	5.7255E-07	1.5931	-0.6196
1000	6.0086E-11	4.3951	-6.9811E-02	5.8276E-10	2.572	-5.2063E-03
1100	1.3742E-09	3.971	-9.3382E-02			

Table 4.9 Creep parameters from the test data of different FG-alloys.

	75/25			50/50			25/75		
T	*A*	*n*	*m*	*A*	*n*	*m*	*A*	*n*	*m*
25	3.72E-13	2.0506	-0.53373	3.8189E-13	2.4636	-0.67728	1.6991E-16	3.3579	-0.48114
600									
700	3.72E-09	2.0506	-0.53373	3.8189E-09	2.4636	-0.67728	1.6991E-12	3.3579	-0.48114
800	7.45E-10	2.6623	-0.30985	4.0439E-09	2.2591	-0.5087	7.3310E-14	3.6489	-4.9149E-02
900	3.13E-11	4.0493	-0.29178	1.2449E-07	2.1176	-0.53347	9.7791E-11	3.4655	-0.33656
1000				2.2725E-06	1.574	-0.56529			

Figures 4.22, 4.23 and 4.24 show the values of the creep parameters in a form of charts. Also the extrapolations and interpolations are shown by lines between the markers, except in Figure 4.22 the lines only have an illustrative function. The lines in Figure 4.22 do not represent the interpolated values, since the vertical axis has a logarithmic scale. The lines are completely dashed, since both the linear interpolations between the test temperatures and the extrapolations outside the test range are quite inaccurate.

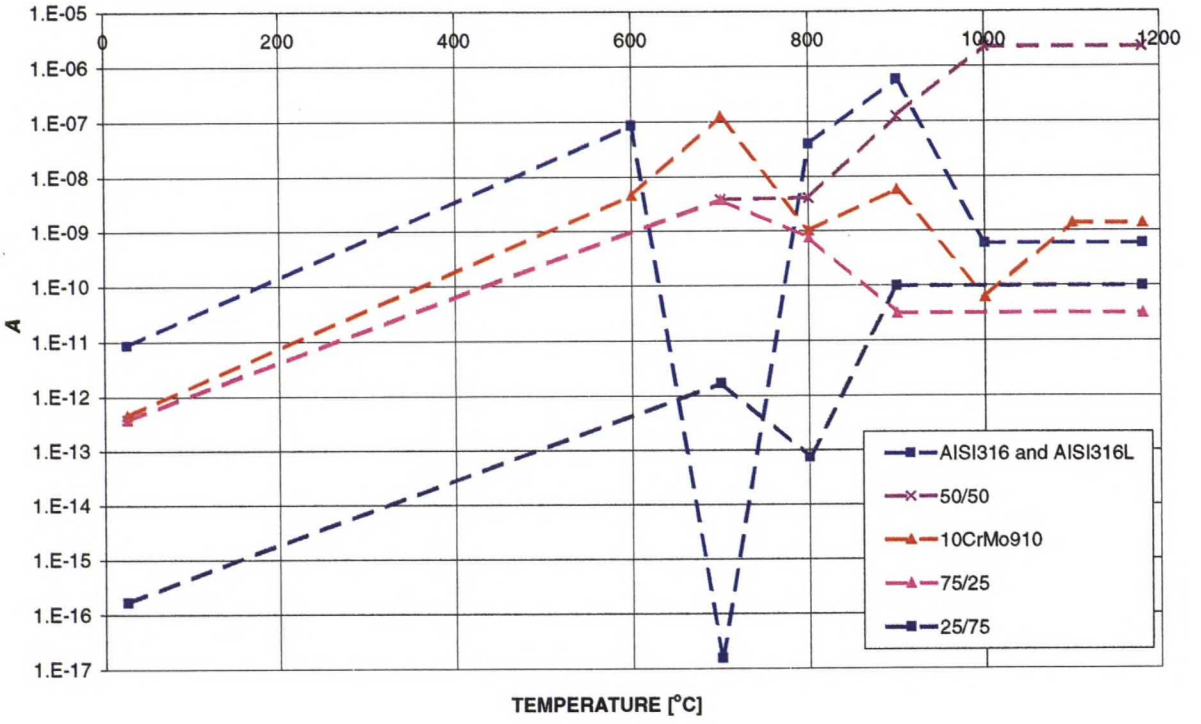

Figure 4.22 The creep parameter A as a function of temperature. The y-axis has a logarithmic scale. The lines between the fitted values do not correspond here with the interpolated values.

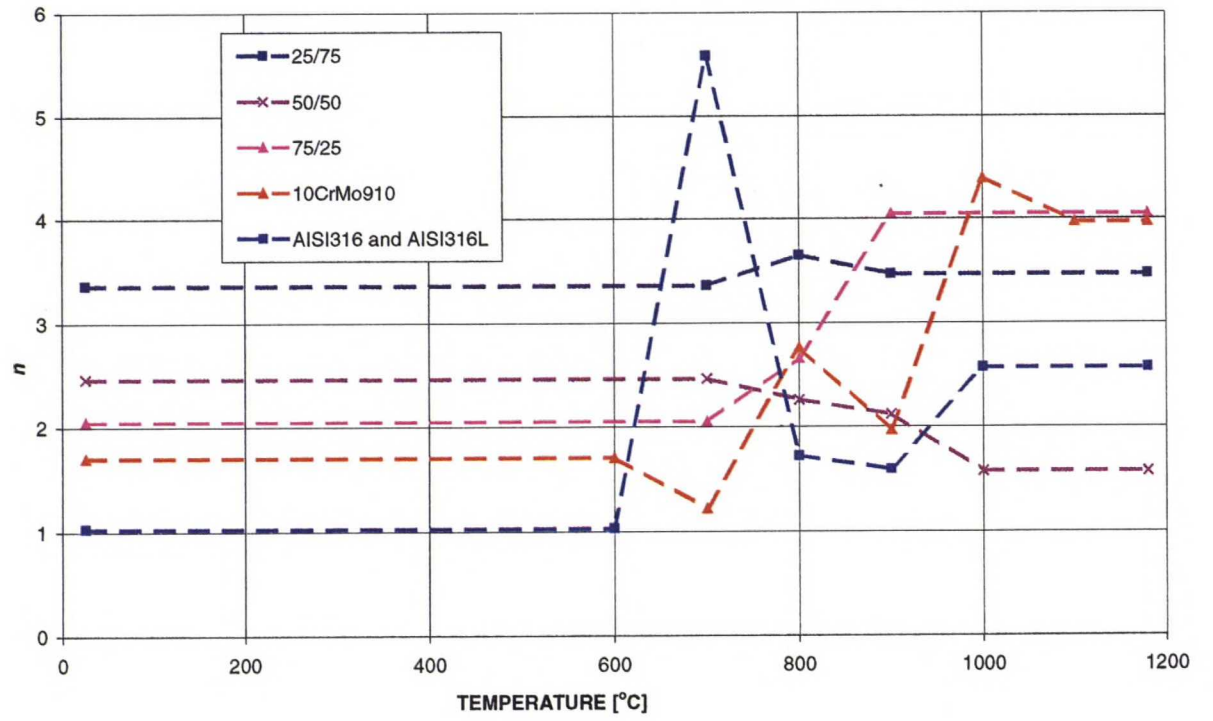

Figure 4.23 The creep parameter n as a function of temperature.

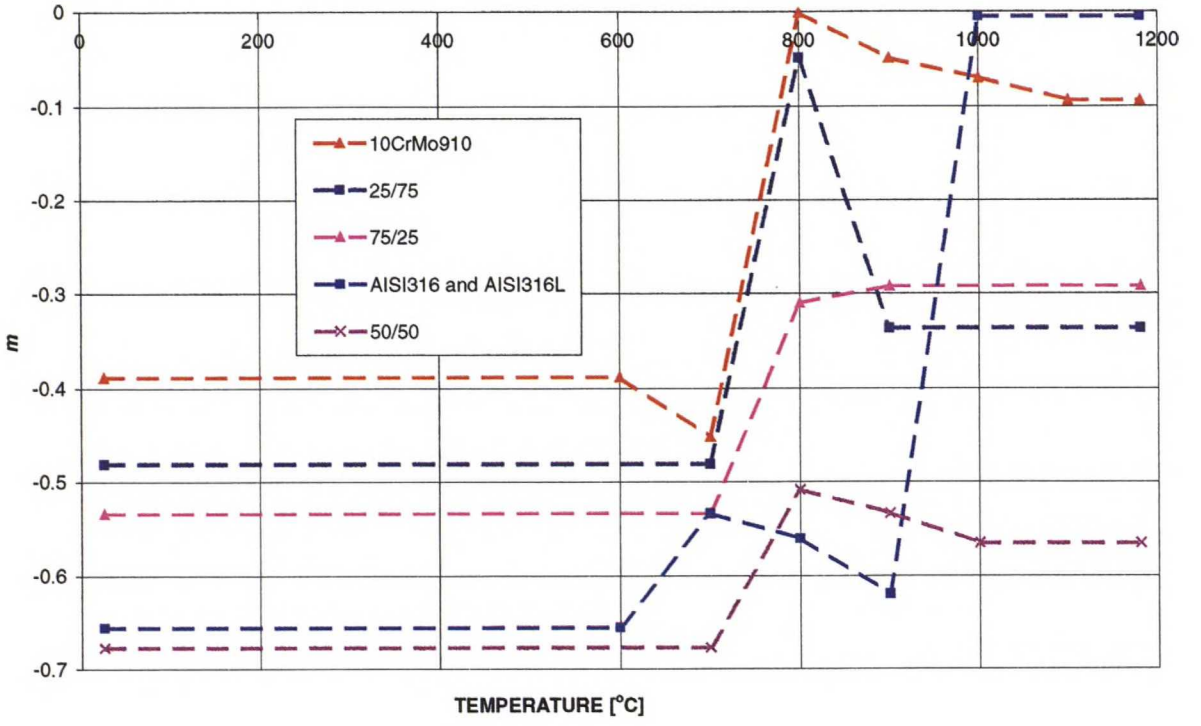

Figure 4.24 The creep parameter m as a function of temperature.

5 NUMERICAL SIMULATION

5.1 Finite Element Method

The thermal and mechanical intial-boundary value problems are solved by ABAQUS/Standard, which is a commercial, general-purpose computer program using finite element method (FEM). FEM is shortly characterized as a general discretization procedure of continuum problems posed by mathematically defined statements. In other words, the continuum is divided into a finite number of parts. These parts are called elements and their behavior is specified by a finite number of parameters. They are connected at certain points, nodes. At each node, a local equilibrium is established. The displacement formulation of FEM is based on approximating the equilibrium requirement by replacing it with a weaker requirement: The equilibrium (Equation (4.4) in static analyses) must be maintained in an average sense over a finite number of divisions of the volume of the body. The displacements of nodes are the basic unknown parameters of the static problem. Once the displacements have been determined by solution of the over all structural type equations, the strains are determined in the global coordinate system. The stresses at any point can then be found using the stress-strain relations, which can be very complex. The displacement at any point within the element (e) is approximated by

$$\mathbf{u} = \mathbf{N}\mathbf{u}^e \tag{5.1}$$

in which the components of $\mathbf{N}$ are prescribed interpolation functions and $\mathbf{u}^e$ represents a listing of nodal displacements. The elements applied to the models in this study are so called second-order elements, which use quadratic interpolation.

A Lagrangian description of the motion of the continuum is used: The element deforms with the material. Reference configuration is chosen to be the actual initial configuration at point of time t=0. Since the material response involves nonlinear behavior, solutions to the partial differential equations are obtained at consecutive time increments. Iteration is allowed within each increment. (ABAQUS, 1998).

5.2 Finite Element Models

The same base finite element model is divided into several slightly different cases, where material definitions vary or some elements are added, changed or ignored. The cases are explained in Chapter 5.2.1. First, let us have an overview of the models and their common features. Since the specimen remains axisymmetric during the whole process (due to axially symmetric loading and boundary conditions), the model is simplified to two dimensions using axisymmetric solid elements. Each element, except the gap elements explained in Chapter 5.2.1, is assigned properties of a certain material. The powder material layers from the bottom to the top are 10CrMo910 steel, 75/25 steel, 50/50 steel, 25/75 steel and AISI316L steel. They are treated as series of perfectly bonded composite interlayers. The remaining elements are assigned material properties of AISI316 steel. The coordinate system and an example of the finite element mesh utilized are shown in Figure 5.1. This example mesh is the largest one, where both the central core and the container are modeled and assumed to be connected with the powder material as a solid continuum. The model dimensions are similar to the dimensions of the component shown in Figure 2.1. The total height is 250 mm. Total diameter is 30.15 mm. It consists of the central core with 17.5 mm radius, the inner wall of the AISI316 steel container (1.5 thick), the HIPped powder metal tube itself (9.5 mm thick) and the outer wall of the container (1.65 mm thick).

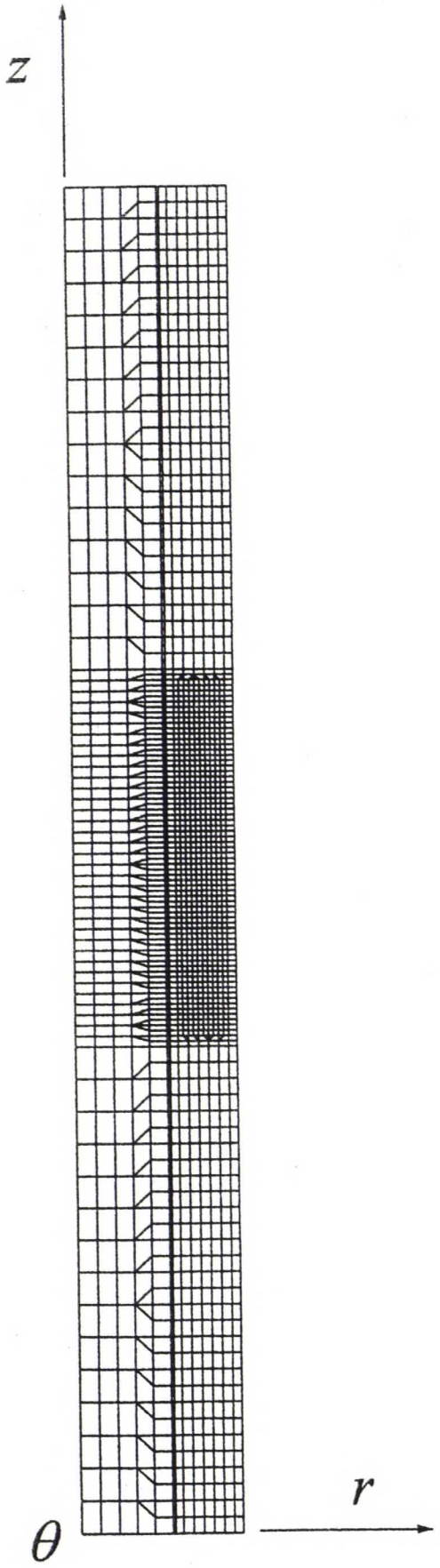

Figure 5.1 Coordinate system and an example of FE mesh.

As can be seen in Figure 5.1, the mesh is coarse near the left boundary, which corresponds to the axis of symmetry. The largest elements are 6 mm high. The middle part of the mesh is refined, because the most interesting points are located in the functionally graded part of the specimen, especially near the outer radial free surface. The refined mesh is 70 mm high and includes well the FG-region. Elements of that section are 0.95 mm wide and 1 mm high. A 50 mm high part from the middle of the refined section is shown in some detail contour plots (Figure 9.3 for example). In the center of the model there is a vertical zone of 0.5 mm wide elements, which is needed in modeling the contact of the central core and the container.

The main variable property in the models is the height of the FG-region. The aim is to find out the lowest possible height with which the overlapping interfaces do not have an effect on each other's stress distribution, at least a distinct one that elevates the stresses. It would be interesting to simulate different kind of material proportions as a function of distance, for example a volume fraction of the other material by a power-law equation (Williamson et al, 1995)

$$\tilde{V} = \left(\frac{x}{b}\right)^d, \tag{5.2}$$

where x is the distance from the pure material towards the other one, b is the thickness of the graded region and d is an arbitrary exponent controlling the shape of a nonlinear composition gradient. However, with only 3 different FG-materials that is difficult and pointless in its inaccuracy. Instead, a linear change from 10CrMo910 steel to AISI316L steel is modeled in every case and with accuracy limited by the number of FG-materials and the size of the elements in the FG-region. In these analyses, four different heights are considered: 10 mm, 20 mm, 30 mm and 40 mm. Each FG-region is located in the middle of the component.

The outer wall of the container is modeled only in a single case. The powder material was totally incorporated with the container after the HIP process, which is known beforehand to cause shear in the interface of the isostatically pressed solid and the container. That is why the effective stress would be higher with the outer container wall. Peeling off the container, however, induces relaxation and the situation is estimated to be in the long run nearly the same as without the wall. According to many previous studies the peak stresses develop near the radial

free surface and the interface of materials. That is why those regions are of main interest in this work. The inner wall of the container is modeled to be a part of the same continuum with the powder metals in every case. Some attention is paid also to their interface.

A certain problem arises. How much does the boundary condition in the inner surface of the specimen affect the stresses in the outer surface? After the HIP process, the central core was easily separated from the tube, as previously mentioned. It served as a mold in horizontal direction and also as a friction surface in vertical direction. Either both parts are considered to be intact or the clearance and interaction between them is modeled with certain elements or constraints, which are explained in the subchapters of the particular cases.

The central core is modeled to have a constant radius (a perfect cylinder in mathematical sense). Actually, the radius in the real core was slightly thinner towards the top.

The mesh configuration is made up with eight-node biquadratic elements with reduced integration. Reduced integration means that a lower-order integration is used to form the element stiffness. It reduces running time. Normally eight-node biquadratic axi-symmetric elements would have 9 integration points, but with reduced integration they have only 4 integration points. Therefore, element assembly is roughly 2.3 times more costly for the element with full integration than for the element with reduced integration. In addition, second-order reduced-integration elements generally yield more accurate results than the corresponding fully integrated elements. Some triangular elements have to be used in regions where the mesh is refined. They are quadratic with 6 nodes and 3 integration points. Each node has two active degrees of freedom unless separately constrained: The displacements u and v. Quadratic diffusive heat transfer (correspondingly 6- or 8-node) elements are used in the heat transfer analysis and their nodes have only one active degree of freedom: temperature.

5.2.1 Simulation Cases

Next all the simulation cases are explained. Table 5.1 gathers all the cases and shows their differences in few columns of information.

CASE 1

The height of the FG-region is 10 mm, of which 4 mm is 50/50 steel. The material layers for both 75/25 steel and 25/75 steel are 3 mm high. The clearance between the central core and the tube is modeled with gap elements provided in ABAQUS program (ABAQUS, 1998). The gap elements allow for contact between the opposite nodes of the interfaces. The initial separation distance between those nodes is 0.5 mm. The interaction normal to the surfaces allows no penetration of the tube nodes into the inner cylinder surface and no transfer of tensile stress across the interface. The tangential interaction is defined by classical isotropic Coulomb friction model, where the magnitude of the coefficient of friction is set to 0.1. These gap elements are well shown in detail plots of the upmost interface (The white column on the left in Figure 9.16).

CASE 2

The height of the FG-region is 20 mm, of which 6 mm is 50/50 steel. The material layers for both 75/25 steel and 25/75 steel are 7 mm high. The clearance between the inner cylinder and the tube is modeled with gap elements and interactions identical to Case 1.

CASE 3

The height of the FG-region is 30 mm and all three layers are 10 mm high. The clearance between the inner cylinder and the tube is modeled with gap elements and interactions identical to Case 1. This is considered to be a basic case. The other cases are basically only variations of this.

CASE 4

The height of the FG-region is 40 mm, of which 14 mm is 50/50 steel. The material layers for both 75/25 steel and 25/75 steel are 13 mm high. The clearance between the inner cylinder and the tube is modeled with gap elements and interactions identical to Case 1.

CASE 5

This is identical to Case 3, except the outermost element column (AISI316 steel) is now also modeled. The mesh of this case is shown in Figure 5.1.

CASE 6

This is identical to Case 3, except the whole system is modeled intact. The gap elements are replaced by eight-node biquadratic elements with four integration points and reduced integration. Material properties of AISI316 steel are applied to those elements.

CASE 7

This case is identical to Case 3, except it is with a different temperature and pressure transient. The temperature is held at 500°C for five hours during which the pressure is naturally constant as well. This procedure is expected to cause relaxation of stresses. The creep induced relaxation is likely to be small compared to Case 8, but two temperatures are analyzed in order to find a suitable one.

CASE 8

This is identical to Case 3, except it is with a different temperature and pressure transient. The temperature is held at 800°C for five hours during which the pressure is constant. This procedure is destined to cause relaxation of stresses, since creep deformation was observed to occur mainly at temperatures above 600°C.

CASE 9

This is identical to Case 3, but only a part of the cooling down process is simulated starting from a temperature of 800°C and the corresponding pressure of 73.76 MPa. Also the initial stress free temperature for every node is 800°C. This case is studied to make sure that also the stress and strain history at high temperatures has an effect on residual stresses at the room temperature and the expensive testing at temperatures above 800°C is necessary.

CASE 10

This is identical to Case 3, but without thermal expansion for any material. The aim of this case is to show how important role the thermal expansion has in the evaluation of residual stresses in a functionally graded material component.

Table 5.1 Simulation cases.

CASE	FG HEIGHT	GAP	OUTER WALL	HOLD	INITIAL TEMPERATURE	THERMAL EXPANSION
1	10	yes	no	no	1180°C	yes
2	20	yes	no	no	1180°C	yes
3	30	yes	no	no	1180°C	yes
4	40	yes	no	no	1180°C	yes
5	30	yes	yes	no	1180°C	yes
6	30	no	no	no	1180°C	yes
7	30	yes	no	500°C	1180°C	yes
8	30	yes	no	800°C	1180°C	yes
9	30	yes	no	no	800°C	yes
10	30	yes	no	no	1180°C	no

5.2.2 Problem Size

The problem size of the heat transfer and viscoplastic analysis for Case 3 is shown in Table 5.2 by means of a few main attributes. There is no significant difference in problem sizes for the different cases. The computer used is Origin 200 with two R10000 processors.

Table 5.2 Problem size of Case 3.

HEAT TRANSFER

NUMBER OF ELEMENTS	1705
NUMBER OF NODES	5260
DEGREES OF FREEDOM IN THE MODEL	5260
NUMBER OF INCREMENTS	103
TOTAL CPU TIME (SEC)	501.60

VISCO

NUMBER OF ELEMENTS	1836
NUMBER OF NODES	5651
DEGREES OF FREEDOM IN THE MODEL	11563
NUMBER OF INCREMENTS	1200
TOTAL CPU TIME (SEC)	13407
	(3.7 HOURS)

Each analysis is divided into multiple time increments so that the nonlinear solution path can be followed. The challenge is to obtain a convergent solution in the least possible computational time. The time incrementation is automatically controlled. The user only specifies the maximum number of increments, the maximum size of the increment and the size of the first increment. After that, ABAQUS automatically adjusts the size of the increments. In viscoplastic analyses, the user specifies a certain tolerance parameter, which limits the inelastic strain rate change over an increment. This parameter affects the accuracy of the creep integration. It is chosen to be such that the approximate stress error tolerance is 1 MPa. However, it has to be remembered that the tolerances of the material tests are looser. The stress results are presented with a maximum accuracy of 1 MPa in this study.

An iteration is an attempt at finding an equilibrium solution in an increment. Almost in every time increment of every analysis in this study, only one iteration is needed to reach the equilibrium. In some increments, two iterations are needed.

5.3 Loading and Boundary Conditions

Exactly similar temperature and pressure transients are used in every case, except in Case 7 and Case 8, where the temperature and the pressure are kept constant for five hours at certain levels. The temperature transient used in the heat transfer analysis is the measured temperature of the upper thermocouple inside the furnace in Figure 5.2 (the blue curve). This temperature transient was measured at a point located a few millimeters from the specimen surface during the HIP process of the component manufactured in 1996 (Figure 2.1). That is closer to the actual temperature on the specimen surface than the lower one. The initial and stress free temperature for every node is 1180°C (except in Case 9, where it is 800°C) and the above-explained transient is set to every node on the surface of the model. In practice, the temperature transient is different in every node on the edge. The lower part is colder mainly due to convection, as can be concluded both from Figure 5.2 and Figure 2.2. Modeling that behavior would excessively increase the calculation time. Figure 2.2 also tells that the temperatures in the specimen and just outside it in the gas are closer to each other near the top of the oven than near the bottom.

An example of a non-uniform temperature gradient changing linearly in the horizontal side nodes is given on a VTT report (Saarenheimo & Kosonen, 2000). The report shows that a linearly distributed, non-uniform temperature along the model edge brings the residual stresses higher than a uniform one in the studied case.

The isostatic pressure is modeled with a uniformly distributed pressure load on every element face on the edge: In the top, side and bottom of the model. When the gap is modeled, the distributed load is also set both on the inner and outer surface of the gap. The pressure transient is also from the same manufacturing process than the temperature transient (Figure 5.2).

The vertical displacement of every node in the bottom is fixed in every case. The left edge of the mesh corresponds to the axis of symmetry and is thus fixed in the radial direction.

No initial residual stresses or initial strains are applied. Because the analysis is decided to be ended to the room temperature, the total time of the analysis is 6158 seconds, the final temperature is 25°C and the final pressure is 22.02 MPa.

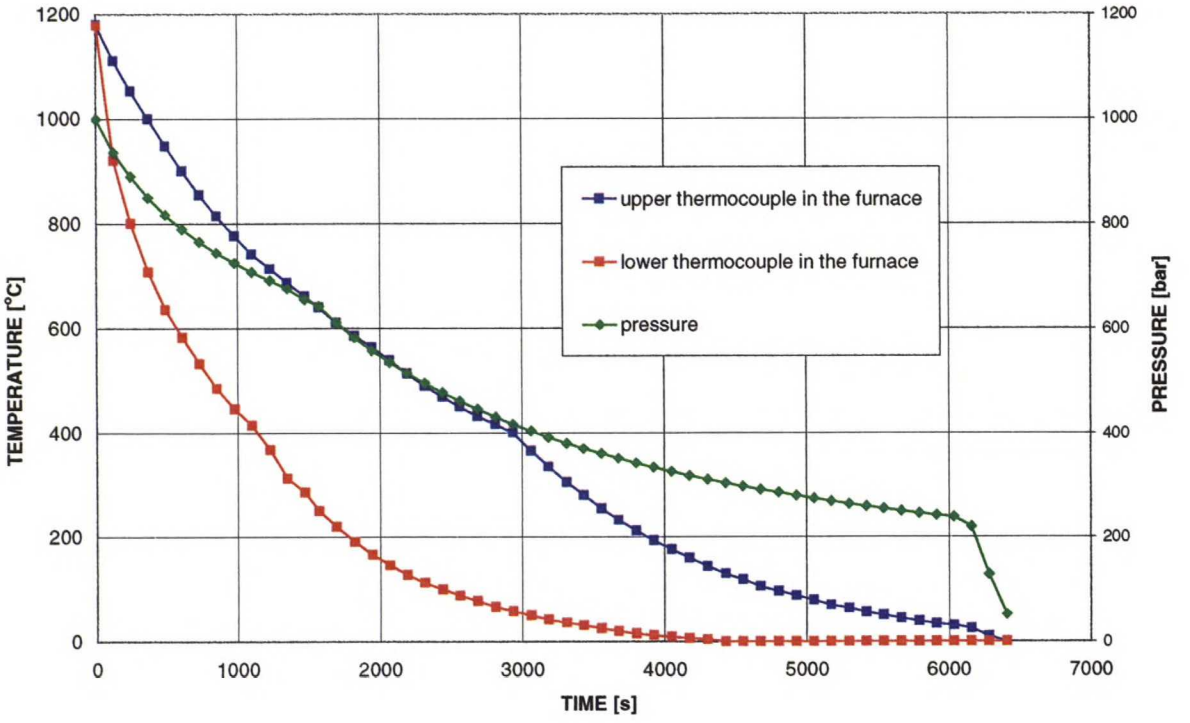

Figure 5.2 Temperatures and pressure in the HIP process on 14th of March 1996. The pressure transient is used in the analyses. The blue curve is the temperature used in the analyses.

6 RESULTS

6.1 Results of Uncoupled Heat Transfer Analysis

The result is as expected: The whole model cools down steadily and the inside is warmer than the surface during the whole analysis. The temperature distribution contour plot in Case 5 at the last time increment of the analysis is shown in Figure 6.1. The surface temperature in the final state is 25°C and the maximum value, circa 27°C, is found on the axis of revolution slightly towards the top. The lower part cools faster, because 10CrMo910 steel has larger thermal conductivity than AISI316L steel. Figure 6.2 shows the cooling at three different nodes in different parts of the model. It shows how uniformly the component actually cools down when the same transient is given to every node on the edge. The coordinates are (node number is subscripted)

$(r,y)_{5385}=(0,90)$,
$(r,y)_{5743}=(0,160)$ and
$(r,y)_{5867}=(0,250)$.

The origin of the coordinates is in the lower left corner of the model (Figure 5.1). The lowest curve (printed in blue) is the temperature transient of a node lying on the edge of the model (number 5867) and is thus the boundary condition (Figure 5.2). The temperatures of the other two nodes are naturally slightly higher during the analysis. The largest differences occur between the range from 1100°C to 900°C, during which the temperatures of nodes 5743 and 5385 are approximately 20°C and 15°C higher than the boundary condition, respectively. In HIP processes of more massive components the temperature differences would be greater.

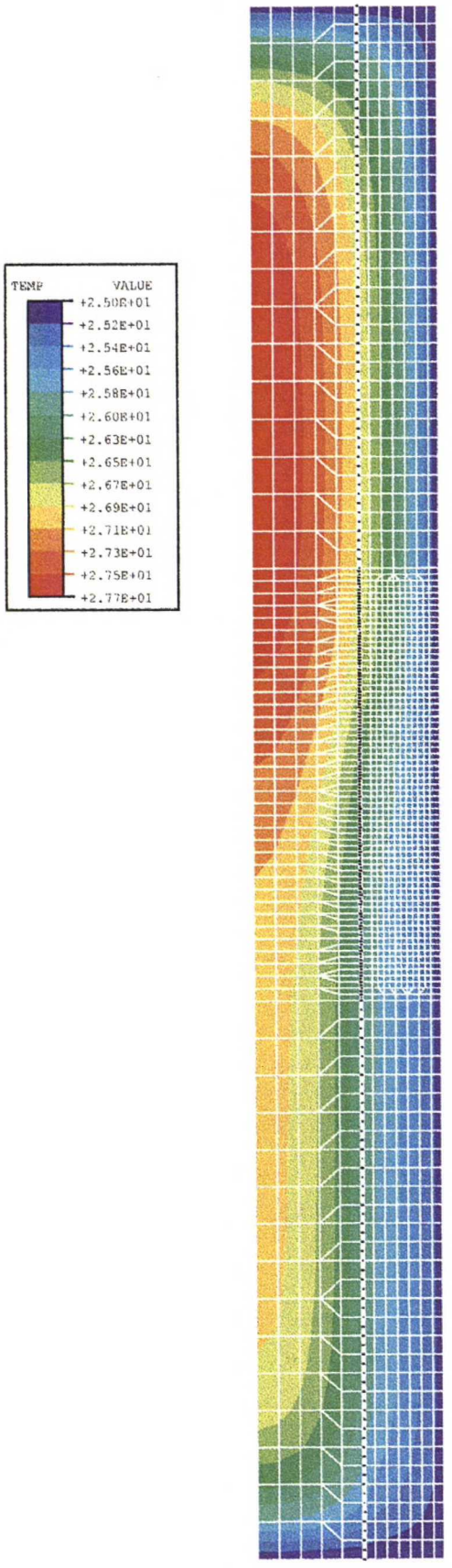

Figure 6.1 Temperature contour plot at the last increment in Case 5. The dark blue color stands for 25°C and red color for 27°C.

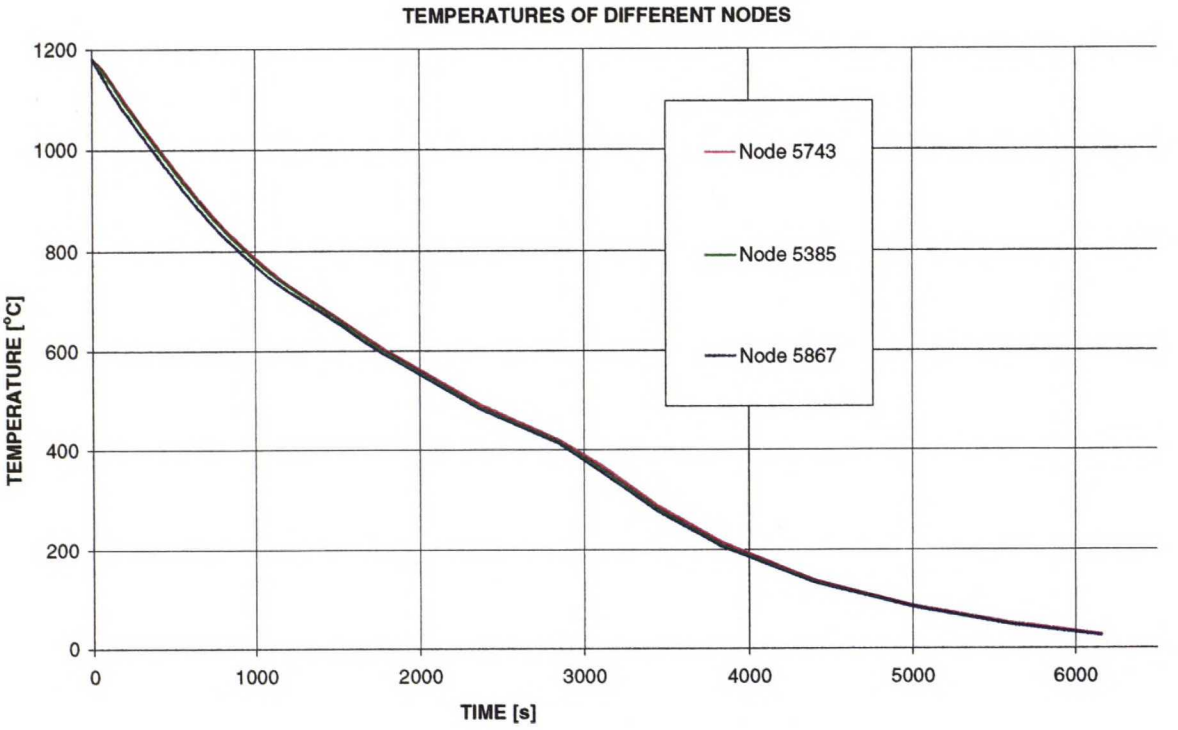

Figure 6.2 Temperature of different points (coordinates written down) as a function of time. The coordinates are $(r,z)_{5385}=(0,90)$, $(r,z)_{5743}=(0,160)$ and $(r,z)_{5867}=(0,250)$.

6.2 Results of the Elastic-Viscoplastic Analysis

The dimensions of the displaced model after the analysis are considerably different to the dimensions of the real component (Chapter 2.6.1). There may be various reasons for that. The pressure may not be uniformly distributed during the HIP process and the boundary conditions do not correspond to the real ones. The main reason is of course that the consolidation of the powders is not numerically modeled in any way. That is why this comparison is slightly questionable. Hopefully, some useful points will arise. The compaction (the total change of dimension) in vertical direction is more than 6 mm in the model and only 0.7 mm in practice, as can be calculated from Figure 2.4. According to conversation with Antero Jokinen (Jokinen, 1999), the very low compaction in practice is due to the fact that the pressure cannot be made totally isotropic and it is larger on the longer side of the component. In other words, the axial pressure relatively decreases during the process. It is not examined, if there was same kind of undulation along the surface of the real component as in FEM-model (Figure 9.1 and especially detailed Figure 9.2). This kind of shape distortion is mostly due to the inequal values of the coefficient of thermal expansion within the whole temperature range of the process. The layers with AISI316L steel and 50/50 steel as the material have higher coefficient of

thermal expansion than their neighboring material layers and thereby contract more. The compaction in horizontal direction is larger in practice than in the model. In the model (Case 5), the nodes on the outer surface have radial displacements from approximately -0.5 mm (10CrMo910 steel) to approximately -1 mm (AISI316L steel). In the same model, each node on the edge of the central core moves approximately 0.4 mm towards the axis of symmetry. Thus, the core is finally approximately 0.8 mm thinner than in the initial position, which is quite close to the real situation.

The elastic, plastic and creep strains do not have as distinct effect on the final shape of the model as the thermal strain does. The elastic deformation (ε^{el}) is recoverable. Both the plastic strain (ε^{pl}) and the creep strain (ε^{cr}) occur only in certain small areas and have thus a minor effect on the distortion of the whole component (Figures 9.13-9.15).

When closely examining Figure 9.1, it shows that the gap is closed between the upper part of the tube and the central core (where the powder material is AISI316L). They are in direct contact. All the other gap elements are open, which means there is a gap of width between 0 mm and approximately 1 mm. The friction between these two solids has a clear effect on stresses in AISI316L steel, especially on the inner edge.

There is still one similarity between the displaced shape of the real component and the numerical model: Both are thinner towards the top. In practice, this is at least partly due to the fact, that the central core did not have a constant radius even before the process (as the FEM model does) and it served as a mold for the tube around it.

Before examining the residual stress and strain results, the main variables are briefly described. They are:

$\overline{q}$

von Mises equivalent stress, defined in chapter 4.3. It does not tell the direction of the stress, but is useful in telling about possible yielding.

σ_{12}

Shear stress in the radial and axial direction (thus in the direction of every material interface in the undeformed shape of the model). In the case of von Mises yield criterion, the ratio between the yield strengths for shear and tension is $1/\sqrt{3} \approx 0.58$ (derived from Equation (4.19)). That holds true for most of the metals.

$\overline{\varepsilon}^{pl}$

Equivalent (or effective) plastic strain, which can be derived from Equation (4.18) and the definition of von Mises stress. Thus,

$$\overline{\varepsilon}^{pl} = \int_0^t \sqrt{\frac{2}{3}\dot{\boldsymbol{\varepsilon}}^{pl} : \dot{\boldsymbol{\varepsilon}}^{pl}}\, dt,$$

where $\dot{\boldsymbol{\varepsilon}}^{pl} : \dot{\boldsymbol{\varepsilon}}^{pl}$ is the scalar product of the plastic strain rate tensors. (A notation PEEQ is used in Table 6.2 for equivalent plastic strain. It is a notation used by ABAQUS postprocessing program).

$\overline{\varepsilon}^{cr}$

Equivalent creep strain, defined as

$$\overline{\varepsilon}^{cr} = \int_0^t \sqrt{\frac{2}{3}\dot{\boldsymbol{\varepsilon}}^{cr} : \dot{\boldsymbol{\varepsilon}}^{cr}}\, dt.$$

(A notation CEEQ is used in Table 6.2 for equivalent creep strain. It is a notation used by ABAQUS postprocessing program).

WHOLE COMPONENT

First a clear general picture of the stress state can be got by looking at the contour plot of von Mises stresses in the whole system (Figure 6.3). Case 5 is considered for the reason that the whole system is modeled and on view. The stresses are scaled in a way that the different regions are well separable. The central core is in blue color, which means that the equivalent stress stays below 20 MPa. The container is completely colored red, which means the stress is all through over 220 MPa. The HIPped pipe itself has mainly stresses of magnitude between 80 MPa and 120 MPa (green), but higher values occur near the inner and outer surfaces and especially in the FG-region, where the values go well beyond 220 MPa.

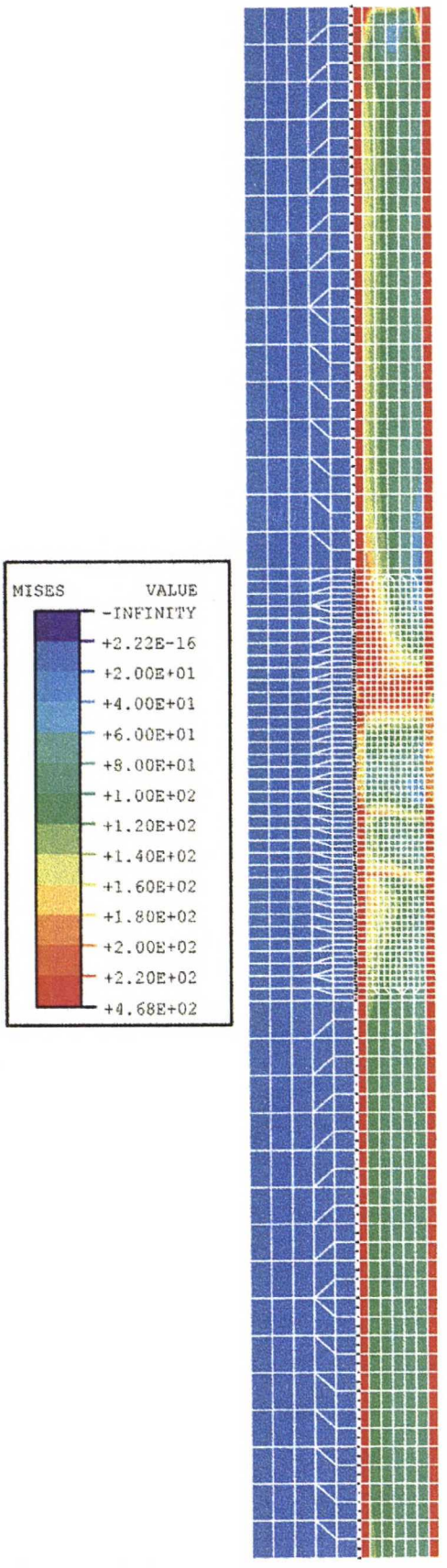

Figure 6.3 Contour plot of von Mises stress [MPa] distribution at the last time increment of the analysis (total accumulated time is 6158 seconds) in Case 5.

FG-REGION

Hereafter, only stresses in the FG-region are considered. All the contour plots in this work are from the last time increment. Thus, they are from the final state of the analysis, when the whole component has an approximate temperature of 25°C. The detail plots are from the middle of the component and they are 50 mm high. Thus, in Case 3 for example, there is the 30 mm high FG-region completely shown. Above that region there is a 10 mm high layer of AISI316L steel shown (10 element rows). Under that there is a 10 mm high layer of 10CrMo910 steel shown. The material layers are best seen in Figure 9.2. First the residual stress state of the basic case (Case 3) is studied. Contour plots of different stress components are shown in Figures 9.3-9 (except 9.6, which is a vector plot). The order is following: von Mises stress ($\overline{q}$), shear stress (σ_{12}), the maximum principal stress (σ_3), axial stress (σ_{22}), radial stress (σ_{11}) and circumferential stress (σ_{33}).

Before going deeper into results, it must be remembered that the model is only an idealization of the real situation. The bonds are mainly made quite seamless nowadays. The material composition changes smoothly in them. Naturally, distinct stress and strain peaks develop between different materials, and in smooth joints this phenomenon is surely not so evident. The different cases are, however, comparable and the results give at least a right direction both qualitatively and quantitatively. For example, if there is a maximum peak somewhere near a material interface (let it be between AISI316L steel and 25/75 steel), most presumably highest values are also found in a real component in a spot where the composition is similar (~20/80). Moreover, a real component may have some critical areas, which do not exist in these numerical analyses at all.

According to (Chiu, 1992) and (Thouless, 1991), in failure of ceramic-metal interfaces, at the radial free edge, the most important stress components are believed to be the axial tensile stresses (σ_{22}) and shear stresses (σ_{12}). In the interior region, the main stress components of interest are the in-plane stresses, radial (σ_{11}) or circumferential (σ_{33}). It holds certainly for metal-metal interfaces as well. The interior region is believed not to be important in this case. The contour plots of von Mises stress distribution, for example, show that the stress peaks are at the interface, near both the inner and outer surface.

Figure 9.3 shows that the most interesting interface is the upmost interface between AISI316L steel and 25/75 steel. The material is yielding and hardening still at the room temperature. Details of different stress and strain contours from that particular region in Case 3 are shown in Appendices (Figures 9.16-24) to get a clear picture of the stress/strain state and its history. Corresponding contours of the same region in different cases are also examined, although every one is not shown here. They tell that the situation is very similar at least in Cases 1-4. Only the magnitudes differ slightly. The range in Figure 9.3 is from zero to 440 MPa. Near the lowest and second lowest interface $\overline{q}$ is between 120 MPa and 160 MPa. Near the interface between 25/75 steel and 50/50 steel it stays below 120 MPa.

Figure 9.4 shows, how the shear stress peaks develop near the edges - both in the interfaces of different alloy materials and directly between them in the middle of each material edge. The sign of the shear stress has no essential meaning. Notice how σ_{12} is very small in dark green regions, in very large areas around the peaks. The absolute values stay below 100 MPa, except near the upmost material interface.

Another variable examined is the maximum principal stress, σ_3 (Figure 9.5). Principal stresses act across planes on which the shear stresses are zero. The order of principal stress magnitudes is $\sigma_1<\sigma_2<\sigma_3$. If the whole component was made of the same single material, the state of stress in it would be near hydrostatic. Every three principal stress values would be equal and, in addition, they would all be negative. That means uniform compression in every direction. However, they are not equal in these analyses. If there is tension, σ_3 represents its magnitude and especially its direction well. Tensile stresses in the interface are of notable interest, since possible cracks develop most likely in the interface to the radial free surface and the tensile stress increases the crack propagation. Figure 9.5 is scaled from zero to 220 MPa. Dark blue represents regions with pure compression, because even the maximum principal stress is negative. The relatively large area of tensile principal stress in AISI316L material is easy to understand, when remembering the displaced shape of the component. The material AISI316L steel contracts most and 25/75 steel tends to pull it to its original position.

The direction of the maximum principal stress (σ_3) is examined in Figure 9.6, where σ_3 is shown as vectors in Case 3 again. The figure is bounded to cover only a part of the FG-region and also a part of the central core. The gap elements are also well separable. First of all, this

figure shows that the large area of tensile stresses is directed along the circumferential axis (θ-axis). The inner wall of the container has high axial tensile stresses (at least near 25/75 material). The detail of upmost interface is shown in Figure 9.19.

Figure 9.7 shows the axial stress, σ_{22}, in Case 3. On the outer edge, there is tension and compression on opposite sides of each interface, except the second upmost interface. More attention is paid to the outer edge. The stress distribution is different on the inner edge, since the capsule wall carries the axial stress there. There is a large area of tension in AISI316L and high peaks exactly at the intersection of three different materials. Mainly, the values are between zero and -100 MPa (compression).

Figure 9.8 shows the radial stress, σ_{11}, in Case 3. It is concentrated in the center of the material interfaces. The upmost interface has values over 220MPa and under -220 MPa, otherwise the absolute values remain relatively low.

Figure 9.9 shows the circumferential stress, σ_{33}, in Case 3. It also concentrates on the interior region near the interfaces. This figure shows that the tension in AISI316L (near the joint) is mainly directed along the third axis. If AISI316 steel is not considered, the distributions of the radial and circumferential stresses are very similar.

Next all the different cases are compared by showing von Mises stress distribution contour plots in every case (Figures 9.10-12). The plots are still about the FG-region. The stress distributions for Cases 1, 2, 3, 4, 5, 7 and 8 are very similar. In Case 1 there are also rather high stresses near the lowest interface. According to Figures 9.10 and 9.11, Case 5 is otherwise similar to Case 3, but the stress peak on the radial free edge does not extend so far. That is again due to the outer container wall, which carries the axial stress in Case 5. Cases 3, 7 and 8 are almost identical. Keeping the temperature constant for five hours does not seem to affect clearly the residual stresses according to these figures. In Case 6 the stresses are higher near the inner surface of the HIPped pipe, especially in 10CrMo910 steel. That is due to the fact that there is no gap, which would permit sliding between the tube and the central core. In other cases except Case 6 the tube is not in contact with the core near 10CrMo910 steel. In Case 9 the model seems to have slightly lower stress values than in Case 3. If the values differ very much, the analysis cannot be started at the temperature of 800°C without further infor-

mation. Case 10 is completely different. Notice the scaling: Red color represents values over 50 MPa while for other cases over 440 MPa. The reason for having Case 10 was only to show the importance of the thermal expansion. By the way, largest creep and plastic deformation occur in the same location as the stress peaks lie in Case 10 (see Figures 9.14 and 9.15).

Figures 9.13-15 show contours of the thermal strain, the equivalent plastic strain and the equivalent creep strain after the last increment in Case 3. Figure 9.13 shows that the thermal deformations in the model are very logically distributed. When comparing to Figure 4.1, it is seen that the higher the coefficient of thermal expansion is during the process, the higher the thermal strain is. Interestingly, 50/50 steel has higher thermal strains than AISI316L steel. Plastic deformation takes distinctly place only in small areas, around the 50/50 material, where the highest values are up to 10 %. To be precise, the peaks are located in upper sides of both 50/50 steel and 75/25 steel (the concept of horizontal direction can be misleading and should not be generalized. However, in this text, "up" means always "towards AISI316L steel"). The highest creep strain occurs also in 50/50 steel. The creep strain has not as high values as the plastic strain, but it is more widely spread. The whole 50/50 material has creep strain values approximately between 1.2 % and 3.8 %, Figure 9.15.

Large inelastic strains can also promote failure due to the void growth and coalescence (Reimanis, 1991). That is why cracks may develop for example between 50/50 steel and 25/75 steel, where the inelastic strains are highest. The same conclusion could easily be reached just by viewing the displaced shape (Figure 9.2).

The residual stresses and strains at integration points of certain elements of are calculated in each case and shown in Tables 6.1-4. Only the highest value of the four integration points is included in the tables. The elements chosen are in both sides of every four material interface in the second vertical element layer from the outer container wall. The values are from the final state of the analysis. The locations of these elements for Case 3 are painted in red in Figure 9.2. The second column instead of the outermost is chosen in order to reduce the singularities due to the container or the influence of the free edge if the outer container wall is not modeled. The stresses and strains are more unstable in the outermost element column, where singularities may exist.

Table 6.1. von Mises stress values. The values are rounded to the nearest value divisible by 5. The yield stress of each material at room temperature is also shown in the second column of the table. The values are from the elements shown in Figure 9.2.

CASE	1	2	3	4	5	6	7	8	9	10	$R_{0.2}$
AISI316L	360	365	360	360	380	350	360	360	340	10	341
25/75	300 110	335 30	350 20	360 30	380 95	340 130	350 20	350 20	300 55	10 35	357
50/50	55 95	60 120	65 140	65 160	70 160	115 275	45 155	65 120	50 185	25 55	478
75/25	220 135	185 125	150 150	130 160	150 190	115 290	155 130	110 145	135 115	45 30	577
10CrMo910	280	210	175	160	170	295	170	130	145	10	359

Table 6.2 Shear stress values. The values have are rounded to the nearest value divisible by 5. The shear strength of each material at room temperature is also shown in the second column of the table. The values are from the elements shown in Figure 9.2.

CASE	1	2	3	4	5	6	7	8	9	10	τ_m
AISI316L	-145	-155	-160	-160	-185	-140	-160	-160	-140	0	197
25/75	-145 5	-155 10	-160 -5	-160 -10	-190 -20	-140 20	-160 5	-160 -10	-140 25	0 -10	206
50/50	10 -45	10 -55	-5 -60	-15 -60	-15 -60	30 -45	10 -65	-10 -45	30 -60	-15 -20	276
75/25	-45 -60	-55 -65	-60 -65	-60 -65	-60 -70	-50 -35	-65 -60	-40 -65	-60 -50	-20 -10	333
10CrMo910	-55	-60	-65	-65	-65	-35	-60	-65	-50	-10	207

Table 6.3 Equivalent creep strain values in percentages. The values are rounded to the nearest thousandth part. The values are from the elements shown in Figure 9.2.

CASE	1	2	3	4	5	6	7	8	9	10
AISI316L	1.3	1.4	1.4	1.5	1.5	1.4	1.4	1.4	0.2	0
25/75	0.6 0.5	0.8 0.5	0.9 0.5	1 0.6	1.1 0.8	1 0.8	0.9 0.6	1 0.5	0.2 0	0 0
50/50	3.3 3.4	3.5 3.5	3.5 3.4	3.5 3.3	3.4 3.5	3.7 3.4	3.5 3.4	3.5 3.4	0.4 0.3	0.1 0.3
75/25	1.1 0.4	1.1 0.2	1.2 0.2	1.3 0.2	1.4 0.5	1.4 0.8	1.2 0.2	1.3 0.2	0.1 0	0 0.1
10CrMo910	1	0.8	0.8	0.8	0.8	1.4	0.8	0.9	0	0.5

Table 6.4 Equivalent plastic strain values in percentages. The values are rounded to the nearest thousandth part. The values are from the elements shown in Figure 9.2.

CASE	1	2	3	4	5	6	7	8	9	10
AISI316L	0.5	0.6	0.5	0.5	0.8	0.4	0.5	0.5	0.1	0
25/75	0.6 0.8	0.8 1	0.8 1.5	0.9 2.1	0.8 1.8	1.1 3.8	0.8 1.5	0.8 1.5	0 0	0 0
50/50	5.2 1.8	6.3 1.9	6.8 1.7	6.9 1.5	6.4 2.3	7.4 1.1	6.8 1.7	6.8 1.7	0 0	0 0
75/25	6 0.4	6.3 0	6.8 0	7.3 0	6.4 0	5 0.3	6.8 0	6.8 0	0 0	0 0
10CrMo910	0.1	0.1	0.1	0.1	0	0.2	0.1	0.1	0	0

When comparing the residual stresses in cases with different FG-region heights (from Case 1 to Case 4), some obvious trends can be seen, Tables 6.1-2. It is natural to assume that the lower the FG-region is the higher the stresses are. However, in the lower side of the upmost interface (material 25/75), von Mises stress is getting lower with lower FG-regions. In fact, the material is yielding in the final condition, at the room temperature, only in Case 4. A

similar trend can be seen near the bottom of the 50/50 material. And still more, there is a reversed trend in some other points. The higher peaks occur with the lowest FG-region, as predicted, but the total situation is not that simple. It seems that when the interfaces are closer to each other, they interfere more with each others stress states - by increasing or by decreasing stresses near each other. That phenomenon can somehow be compared to the interference in the theory of wave motion. The stress state stays probably very similar if the height of the FG-region exceeds 50 mm. The shear stresses, σ_{12}, depend much less on the FG-height. The differences are due to other components, such as axial stress component.

If the container is completely modeled, the stresses are slightly higher as seen in Tables 6.1-2 (comparison between Case 3 and Case 5). It is not perfectly known how the stress state changes when the container is peeled off. It is here assumed to relax and be eventually similar to the stress state of Case 3. That is partly why Case 3 is considered as the main case under closer study. The von Mises stress distribution is quite similar in both cases, but especially the axial stress is completely different near the container.

The creep strain values (Table 6.3) are highest in 50/50 steel - more than 3%. In Cases 1-8 creep is very similar. In Case 9 the initial temperature is 800°C, what results in small creep deformations. The plastic strain values (Table 6.4) have more alternation in different cases, especially in Case 6, where the equivalent plastic strain is up to 7.4%. The equivalent plastic and creep strain distributions near the interface areas are shown in Figures 9.14 and 9.15.

THE INTERFACE BETWEEN AISI316L STEEL AND 25/75 STEEL

The most interesting interface is between AISI316L steel and 25/75 steel and it is studied more closely here. Figures 9.16-24 show contour plots from that region (from the final states of the analyses). Mainly the plots are from Case 3, but some other cases are also compared to each other. They are mentioned separately. The order of discussion is the same as with the plots from the whole FG-region: $\overline{q}$, σ_{12}, σ_3, σ_{22}, σ_{11} and σ_{33}. The scaling varies in different figures. It is separately described also in captions.

Figure 9.16 shows a contour plot with $\overline{q}$ as the variable. It is a detail plot of Figure 9.3, where also the inner wall of the container, the central core and the gap elements between them are

shown. The highest peak lies, as expected, in the junction of three different materials. The stress invariant $\overline{q}$ is higher than 440 MPa there. Near the outer edge $\overline{q}$ remains below 400 MPa.

Figure 9.17 shows a contour plot of shear stress (σ_{12}) distribution. The peaks are near the outer edge (between -120 MPa and -200 MPa) and directly on the inner edge (between 200 MPa and 280 MPa) of the HIPped component. If the outer container wall was modeled (Case 5), the peak would also be directly on the outer edge. As mentioned before, high shear stress (σ_{12}) values on edges near the interface are critical to the joint strength. The shear strength of the material can be defined by

$$\tau_m = R_{0.1} / \sqrt{3} \approx 0.58 R_{0.1}. \tag{9.1}$$

Thus, the shear strength of AISI316L steel and 25/75 steel is 197 MPa and 206 MPa, respectively. If local peak values at the surfaces are not considered, σ_{12} remains just below the shear strength.

Figure 9.18 shows a contour plot of σ_3 distribution, Case 3. It is a detail plot of Figure 9.5, except its scale is between zero and 440 MPa. The maximum principle stress rises above 320 MPa in an approximate area of 5 elements. The area of each element is approximately 1 mm^2. Dark blue regions are in three-dimensional compression.

Figure 9.19 shows a rotated plot of maximum principal stress vectors near the upmost interface and the free edge, Case 3. The tension directly on the interface takes place almost in radial direction. AISI316L steel tends to contract more than 25/75 steel, and mainly towards the axis of symmetry. The angle between the vectors and the radial coordinate is approximately 150° (or -30°). 25/75 layer is distinctively in tension in the axial direction on the edge, which can be critical for the joint strength.

Figure 9.20 shows a contour plot of axial stress (σ_{22}) distribution, Case 3. The scaling is between -220 MPa and 220 MPa with intervals of 40 MPa. Figure 9.20 is compared with Figure 9.21, where the outer wall is modeled (Case 5). The stress near the outer edge in the HIPped tube is lower in Case 5 than in Case 3. More interesting, the sign of σ_{22} on two sides of the

interface, near the outer surface of the HIPped material, is opposite in those two different cases. The outer surface under tension in Case 3 is under compression in Case 5 and vice versa. However, modeling of the outer wall has very small effect on the axial stresses in the inner parts of the HIPped material.

Tension near the outer surface is critical to the joint strength. Next contour plots of axial stress (σ_{22}) distributions on the outer edge in Cases 1-4 are compared with each other in Figure 9.22. That is done in order to find out the effect of the height of the FG-region on the axial stress. Figure 9.22 shows that the higher the FG-region is the more critical the situation is in this respect. The tension below the interface is higher in Case 4 than in Case 1. In Case 4 it reaches over 220 MPa on the edge. In Case 1 there is just a small area with axial tension between 140 MPa and 180 MPa. Correspondingly, the compression is highest in Case 1.

Figure 9.23 shows a contour plot of radial stress (σ_{11}) distribution. This is a detail of Figure 9.8. The radial stress in the middle of the HIPped wall and the shear stresses on the edges are depending on each other. The stresses parallel to the interface cause shear stresses on the edges.

Figure 9.24 shows a contour plot of hoop stress (σ_{33}) as the variable. This is an exact detail of Figure 9.9.

DEVELOPMENT OF STRESSES AND STRAINS

It is naturally very essential to know the mechanisms how the stresses and strains develop. The causal connections in the system are very complex. Almost everything affects everything. Curves of different variables as a function of time give a general insight into the mechanism. Figure 6.4 shows the values of the variables presented in Tables 6.1-4 as function of time. The values are from the element in 25/75 layer, near AISI316L steel (second highest element painted in red in Figure 9.2). Again, the case is Case 3.

First of all, the clear connection between $\overline{q}$ and σ_{12} is seen. The curves look otherwise similar except $\overline{q}$ is almost twice as high by magnitude. The stresses alternately increase and decrease at least during the first half an hour in all the 8 elements studied in Tables 6.1-4. This seems

to be the situation in the whole model. $\bar{q}$ and σ_{12} are stabilized, as shown in Figure 6.4, after approximately 1000 seconds in a sense that they increase continuously. The temperature in that moment is approximately 800°C. Since they both develop in a very similar way, the other stress components - σ_{11}, σ_{22} and σ_{33} - develop most probably in that similar way as well. That conclusion is drawn from Equation (4.19). Just before $\bar{q}$ and σ_{12} are stabilized, the equivalent creep deformation stops and $\bar{\varepsilon}^{cr}$ stays constant for approximately 2000 seconds. After that (temperature is approximately 400°C) there still occurs some additional creep deformation. Plastic deformation takes place only during the first 200 seconds (until approximately 1050°C). The strain values shown do not tell about the direction of the strains. It is also noteworthy that some of the material properties at high temperatures are approximated or extrapolated.

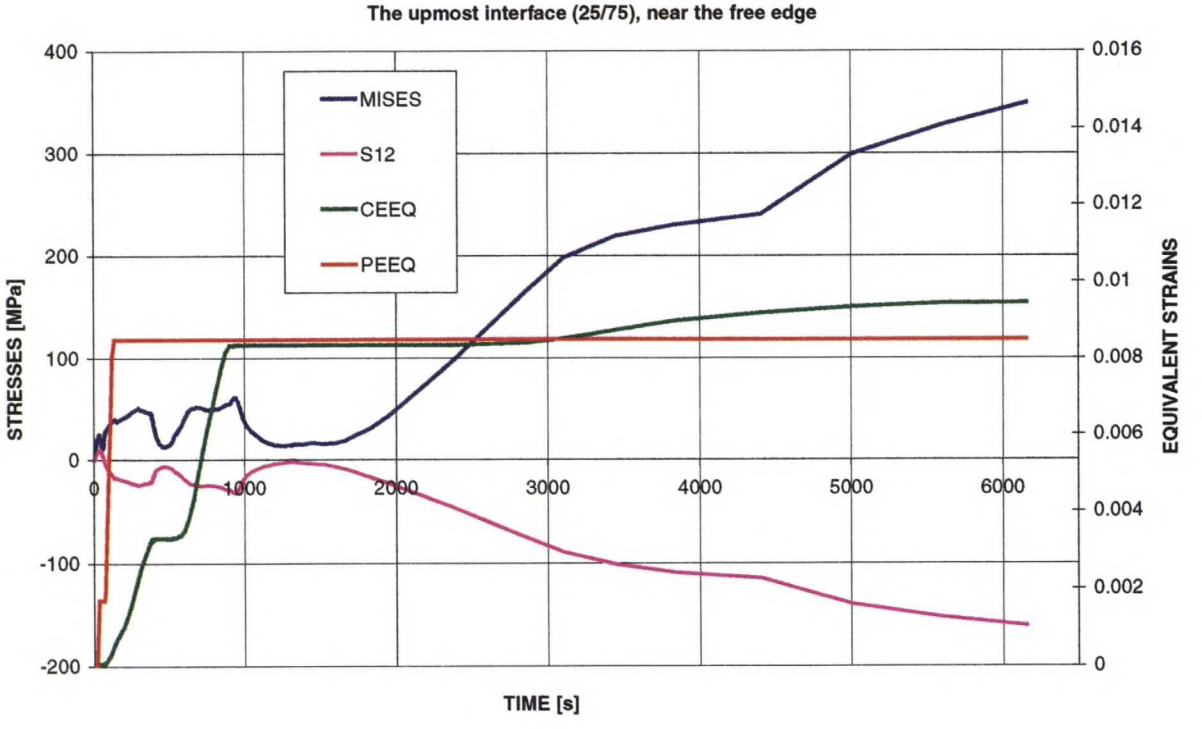

Figure 6.4 $\bar{q}$ (MISES *on the legend),* σ_{12} (S12)*, the equivalent creep* (CEEQ) *and plastic strain* (PEEQ) *as functions of analysis time. Case 3. Values are from the second highest element painted in red in Figure 9.2. The material is 25/75 steel.*

6.3 X-ray Diffraction Measurements and Results

The component manufactured at VTT 4th of May 1999 (Chapter 2.6.1) is examined with X-ray diffraction technique. The aim is to measure the residual stress distribution and to define different phase regions in the component (Siiriäinen, 2000).

First, the central part of the outer container wall (AISI316 steel) is machined off as shown in Figure 6.5. The material around the measurement area is dissolved by electrolysis in order to remove the rough surface layer after machining. The depth of material removal ranged from 0.15 mm to 0.35 mm.

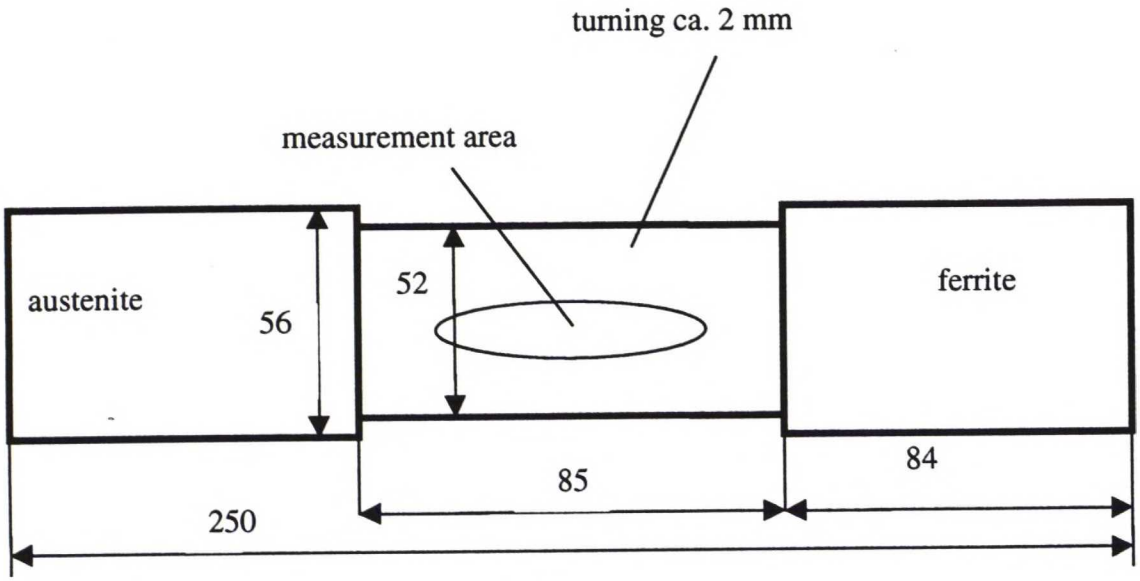

Figure 6.5 Outline drawing of the specimen.

The principal arrangement of X-ray stress measurements is shown in Figure 6.6. Measurements are made in one millimeter strips in the axial direction. This is done using a thin lead plate (25 μm) in which there was a 1 * 15 mm^2 slot. The shorter side is in the axial direction. Lead plate is moved in 1 mm steps in the axial direction. Measurement volume is the following: Penetration depth of X-rays is about 10 μm, width 1 mm and length about 3 mm in the hoop direction.

No distinct borders, where sudden changes in ferrite-austenite proportion would take place, are detected. The measured stress values vary illogically.

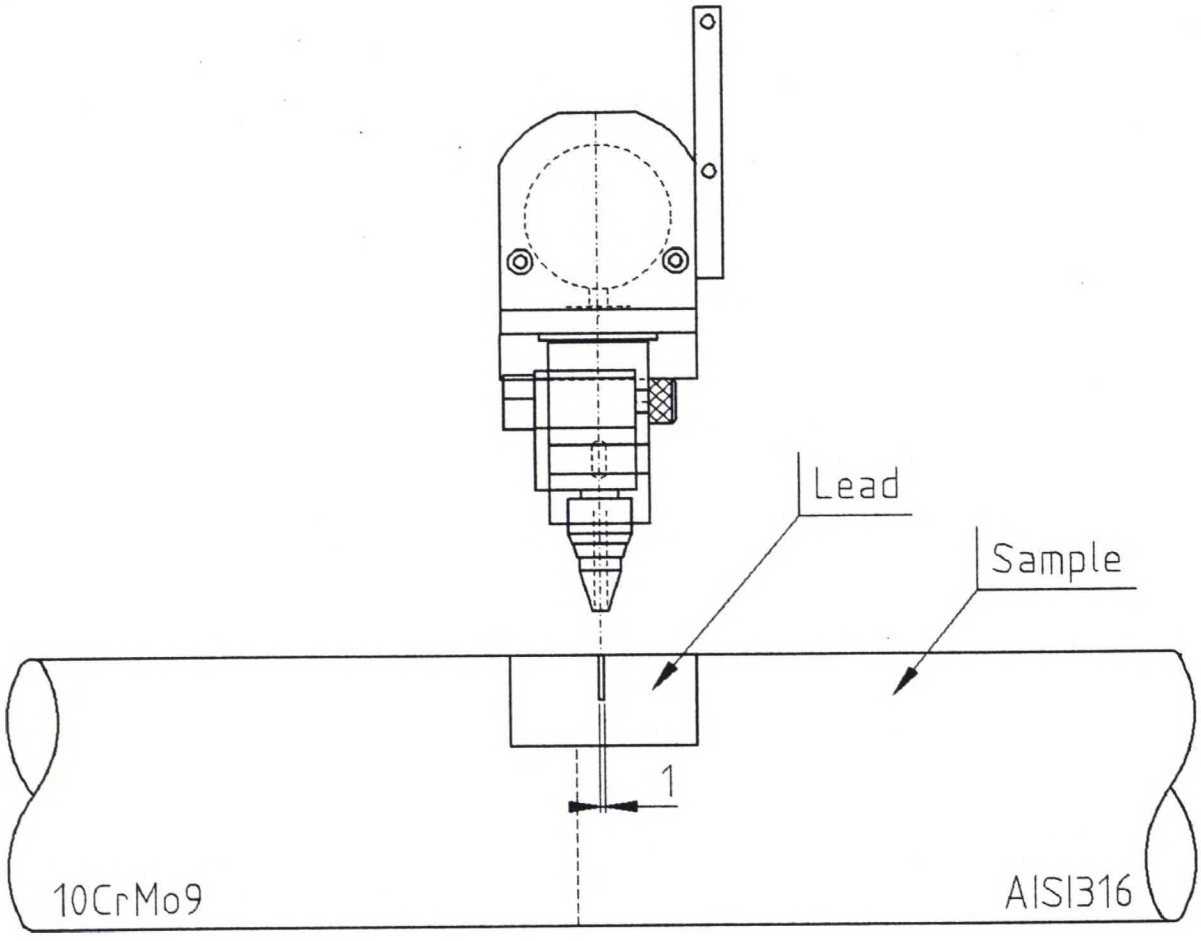

Figure 6.6 Principal arrangement of X-ray measurements.

The measured stresses are the axial stress σ_{22} and the circumferential stress (or hoop stress) σ_{33} and they are measured at 1 mm intervals. They are measured both from the austenite phase and from the ferrite phase. The result is a sum of micro and macro stresses.

The measured stresses from ferrite and austenite are compared to the corresponding simulated stresses of Case 3, which are obtained from the same elements than the variables in Tables 6.1-4. The elements are shown in Figure 9.2. The height of the FG-region was 35 mm before the HIP process. It is presumably the same also after the process, since the compaction in axial direction is so minimal in the whole component. The component has five FG-material layers. The simulated model has FG-region with three FG-materials and height of 30 mm. The results are compared with each other in Figures 6.7-8. The distance in those figures is measured from the bottom of the component (from the side of 10CrMo910 steel). Thus, the center is at 125 mm and 10CrMo910 steel is on the left and AISI316L is on the right.

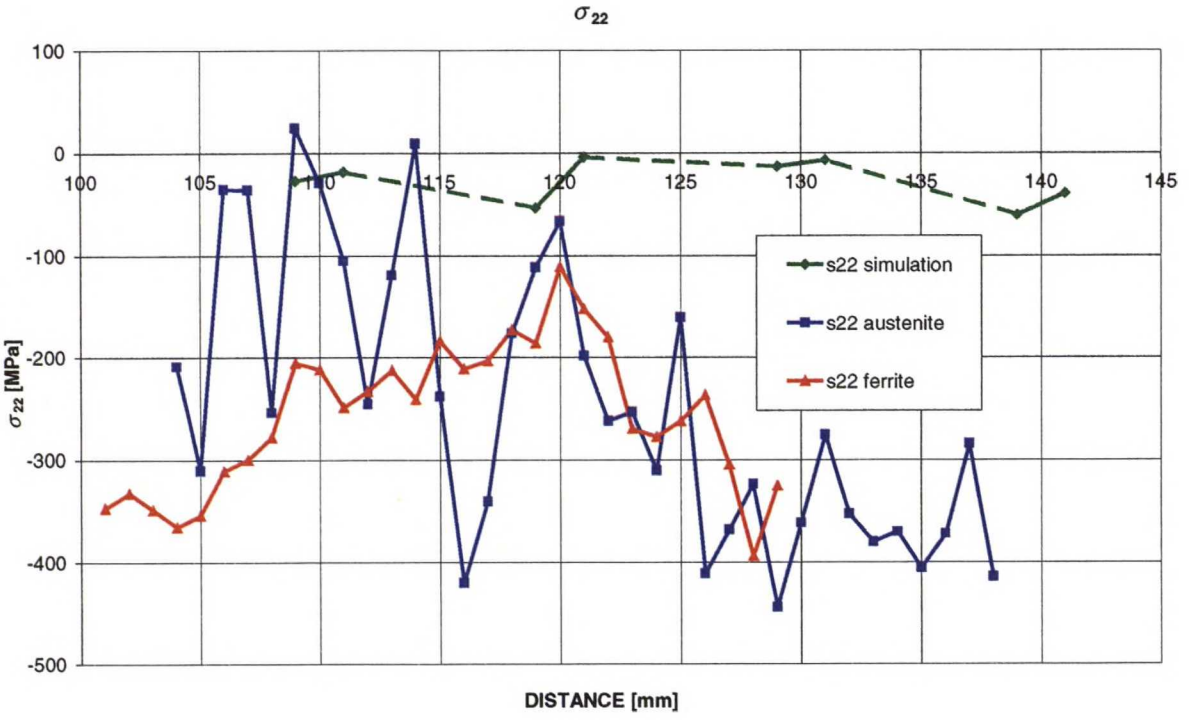

Figure 6.7 Axial stress of the FEM model and axial stress in the austenite and ferrite phase in the measured component.

The axial stress values compared in Figure 6.7 do not coincide well. The simulated absolute values stay low. The reason for that can be seen in Figure 9.7. The values are taken from the second vertical element layer from the right hand side, but the stress peaks lie in the edge elements. It is illogical that the axial stresses measured with X-ray technique seem to be compression. However, when comparing Figures 9.20 and 9.21, it can be seen that with the container modeled there is not much tension in the HIPped material.

If the powders were packed in a desired way, the FG-material interfaces of the measured component would be located approximately on the level 107.5 mm, 114.5 mm, 121.5 mm, 128.5 mm, 135.5 mm and 142.5 mm from the bottom of the component. These interfaces cannot be discerned from the Figure 6.7. That is not surprising, because according to the quantitative metallography measurements in Chapter 2.6.2, no distinct interfaces are found near any side of the X-ray measurement area.

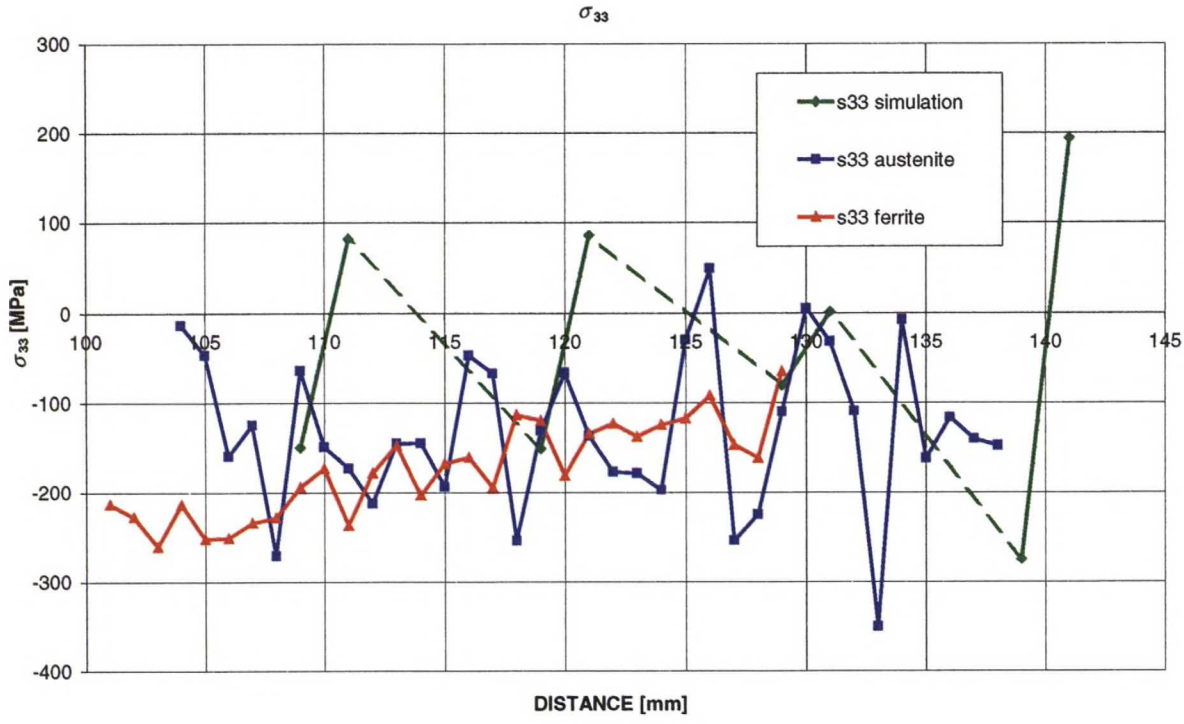

Figure 6.8 Circumferential stress of the FEM model and the austenite and ferrite phase in the measured component.

The hoop stresses compared in Figure 6.8 coincide slightly better. The alternation of simulated stresses is clearly seen both in Figures 6.8 and 9.9. Same kind of alternation is seen in the values measured from the austenite, although not so distinctly. Maybe, even some of the material interfaces can be distinguished with the help of the values from the austenite phase. Also, the hoop stress values measured with X-ray technique stay mainly below zero, which is not the situation with the simulations.

Unfortunately, stresses can be measured only near the outer surface of the specimen with the X-ray technique. Due to the rather high stress gradient near the outer surface, the comparison of measured and calculated stresses is not completely a straightforward procedure. In order to verify the numerical results concerning residual stresses in the specimen, measurements inside the specimen are needed. It would also be a benefit to have measurements done using methods of different kind. When considering these results, it should be remembered that the stresses in the measured component are relaxed after machining and the dissolved surface is not as even as it should be. Above all, the real component, which is measured, does not have the same FG-material layers as the simulated model. In fact, the quantitative metallography

measurements in Chapter 2.6.2 show that the component has no distinct separate layer at all. Thus, the pure stress results of the X-ray measurements and the simulations cannot well be compared with each other.

7 SUMMARY AND DISCUSSION

In this study, material parameters of two powder metals, AISI316L and 10CrMo910, and their three mixtures are defined for the elastic-viscoplastic analyses. The component with a smooth FG-region is simulated with different boundary conditions and material sections. The residual stresses and strains are analyzed and the critical aspects are examined thoroughly. Stresses on the edge of the FG-part of the finite element model are qualitatively compared to the values measured using the X-ray diffraction method. The main results of numerical simulations are specified below.

MAIN RESULTS

No considerable significance with the functionally graded region height between 20 mm and 40 mm is found in this study. Anyway, the minimum height at present is 30 mm, because shorter regions are not practical to manufacture for technical reasons. Longer FG-regions than 40 mm probably have only slightly lower residual stresses.

The first interface between AISI316L steel and 25/75 steel is the most critical one concerning the joint strength. This would most probably be the situation also with more powder material layers modeled - with smaller steps in proportions for the powder materials. The highest stress peaks develop thus in reality very near to AISI316L steel. Axial tension near the interface in question is higher in models with higher FG-regions.

The differences in the thermal expansion coefficients of the materials is the most important factor concerning residual stresses. An ultimate aim would be to find out an uniform expansion throughout the body. The 50/50 test material has a very problematic gradient of the coefficient of thermal expansion during the manufacturing process.

The plastic and creep deformations are relatively low in the simulated component and take place very early in the process. Both the plastic and creep deformations are concentrated around the 50/50 material and that is why no clear stress peaks are found in the middle part of the joint.

The whole process starting from the initial temperature and pressure must be simulated for a correct stress build-up. However, this study does not give very exact results at temperatures over 900°C due to the restrictions on acquiring the material data.

Keeping the temperature and pressure constant for five hours either at 500°C or at 800°C has only a minor effect on the residual stresses. At 800°C the effect is more noticeable than at 500°C.

The results of X-ray diffraction measurements do not correlate with the simulation results. Main reasons for this are the differences between the FG-regions of the simulated and the measured component. The stresses in the real component relax after machining the outer container wall. The measurement point locations are not optimal.

FUTURE STUDIES

The future studies should mainly concentrate on designing a more accurate model in many respects. The material model and geometric model built in this study are both decent bases, from which to go further.

Analyses with more materials layers in FG-region would yield more accurate results. Each new material would demand all the material tests explained in this text.

Denser element meshing and would yield more accurate results. Three-dimensional analyses are not necessary, if the geometry and boundary conditions are kept axially symmetric. With a more powerful processor those would be realistically possible. In fact, smaller element size is necessary with more material layers in FG-region. Even in this study material sections of 75/25 steel and 25/75 steel both consist of only three element layers (Case 5).

Carefully considered interpolation of material parameters could be used to replace the expensive and time-consuming material testing. After few more FG-materials tested, maybe some new materials could be modeled between two known ones completely by interpolation. A suggestion is to test four new material between the five used in this study. After that new materials between tested materials would be interpolated - one between each material. Thus,

there would be altogether 17 materials. To model FG-region that is 10 mm high with 15 different materials, at least 45 element rows would be needed. Each element could be at the most 0.22 mm high.

A better creep model should be used. A unified unisothermal material model would be interesting to apply. The model used in this project is good in its simplicity, but inaccurate between two temperatures at which the parameters are achieved by testing. The aim is to make the time dependent behavior depend accurately on the temperature as well. Basically, the minimum creep strain rate should increase with the temperature. ABAQUS interpolates the creep parameters linearly between the test temperatures, which does not make the behavior itself linear or in some cases sensible at all.

Both the creep tests and model should concentrate only on the first few hours of the creep, because the HIP process lasts only for 1.7 hours. In case of 10CrMo910 and AISI316L, the secondary phase of the creep is needed only if very long cooling phases are considered.

Additional tests at high temperatures are needed. In this study material properties above the temperature of 900°C were mainly obtained by using approximations and extrapolations based on the existing data and knowledge. Case 9 shows that also the early stages of the analysis are significant, when considering residual stresses.

Different cooling transients, similar to the ones used in VTT report (Saarenheimo & Kosonen, 2000), should be experimented with this FEM-model. One example would be a linear cooling with duration of approximately 10 hours, which brings down the stresses according to the report mentioned above. A non-uniform temperature gradient along the model edge should also be included in the study, because it is known to affect the residual stresses. At present, the temperature cannot be made totally uniform along the component during the HIP process.

Interesting would be to make a model without 50/50 material, or if a smoother gradient is simulated, to completely exclude materials with powder proportions of between 40/60 and 60/40.

Special attention should be paid on the joint side near AISI316L steel. Probably a very smooth change in material proportions near AISI316L steel would decrease the stresses.

In order to verify the numerical results concerning residual stresses in the specimen, X-ray diffraction measurements inside the specimen are needed. Also, it would be a benefit to have measurements using different kinds of methods.

Besides having results in the form of thermal residual stresses in the whole component, also other valuable information is gathered in this work. Two materials, and their three alloys, are quite thoroughly examined regarding mechanical and some physical properties. Their parameter values are recorded and shown illustratively. Also input values for FEM program are presented to the reader. Various geometric models with finite element meshes are built up. Some suggestions for improving models are made.

8 REFERENCES

1991 Annual Book of ASTM Standards, 1991. Section 14.: General Methods and Instrumentation. Volume 14.03: Temperature Measurement. ISDN 0-8031-2586-0.

ABAQUS / Theory Manual, Version 5.8. Hibbitt, Karlsson & Sorensen, Inc., 1998.

AECMA standard, 1993, part 5.: Uninterrupted creep and rupture testing (prEN 2002).

ASM Metals Handbook, Volume 1. Properties and Selection: Irons, Steels, and High-performance Alloys, 10th ed. Eds. Davis, J.R. et al. ASM International, USA, 1990. 1063 p.

ASM Specialty Handbook Stainless Steels, Ed. Davis, J. R. ASM International, USA, 1994. 577 p.

ASM, 1984. Superalloys Source Book. ISBN 0-87170-170-7.

Chiu, C. C., 1992. Mater. Sci. Eng. A vol 150, 139.

Concurrent Technologies Corporation, 1997. Web document. (referred on March, 1999). Available http://www.ncemt.ctc.com/modsim/hip/

ERA Tech. Sprint Specific Project SPI 249: Standard Data Tables.

Flügge, W., 1972. Tensor Analysis and Continuum Mechanics. Springer-Verlag, Berlin.

Heikinheimo, L., Jokinen, P., Nuutinen, S. and Salmi, J. 1998. FG-materiaalien valmistus. Espoo, VTT. VTT Publications 829. 78p. ISBN 951-38-5002-1.

Heikinheimo, L., 1999. Materials Properties for Assessment of Thermal Residual Stresses. Report VALB360.

Heikinheimo, L., 1999. Private Conversation.

Kemppainen, M., 1999. Private Conversation

Koskinen, P., 1999. E-mail report, Espoo 12.4.1999.

Kosonen, T., 1999. E-mail.

Kosonen, T., 2000. E-mail arrived on February 18th 2000.

Loveday, M.S., Day, M. F., Dyson, B. F., 1982. Measurement of High Temperature Mechanical Properties of Materials. National Physical Laboratory.

Reimanis, I. E., Dalgleish, B. J., Evans, A. G., 1991. Acta. Metall. Mater. vol 39, 3133.

Saarenheimo, A., Heikinheimo, L., Holmström, S., Santaoja, K., 1999. Numerical Simulations of Thermal Residual Stresses in a Multimaterial Component - A Hot Isostatically Pressed Steel to MMC Assembly. Report VALB393.

Saarenheimo, A., Kosonen, T., 2000. Numerical Simulations of a Hot Isostatically Pressed Test Specimen. Report VALB426.

Salmi, J., Keskinen, J., Sillanpää, H., Ruuskanen, P., 1996. FG-materiaalien valmistus isostaattisella kuumapuristuksella ja SHS-menetelmällä (Manufacturing of FG-materials by hot isostatic pressing amd SHS). Espoo, VTT. VTT Research Notes 1770. 36p. ISBN 951-38-4965-1.

Siiriäinen, J., 2000. Report, Stresstech Oy.

Thouless, M. D., 1991. J. Vac. Sci. Technol. A vol 9, 2510.

Williamson, R.L., Rabin, B.H., Byerly, G.E., 1995. FEM STUDY OF THE EFFECTS OF INTERLAYERS AND CREEP IN REDUCING RESIDUAL STRESSES AND STRAINS IN CERAMIC-METAL JOINTS. Composites engineering, Vol.5, No.7. Elsevier Science Ltd.

Zienkiewicz, O.C., 1977. The Finite Element Method, Third Edition. McGraw-Hill, London 787p.

9 APPENDICES

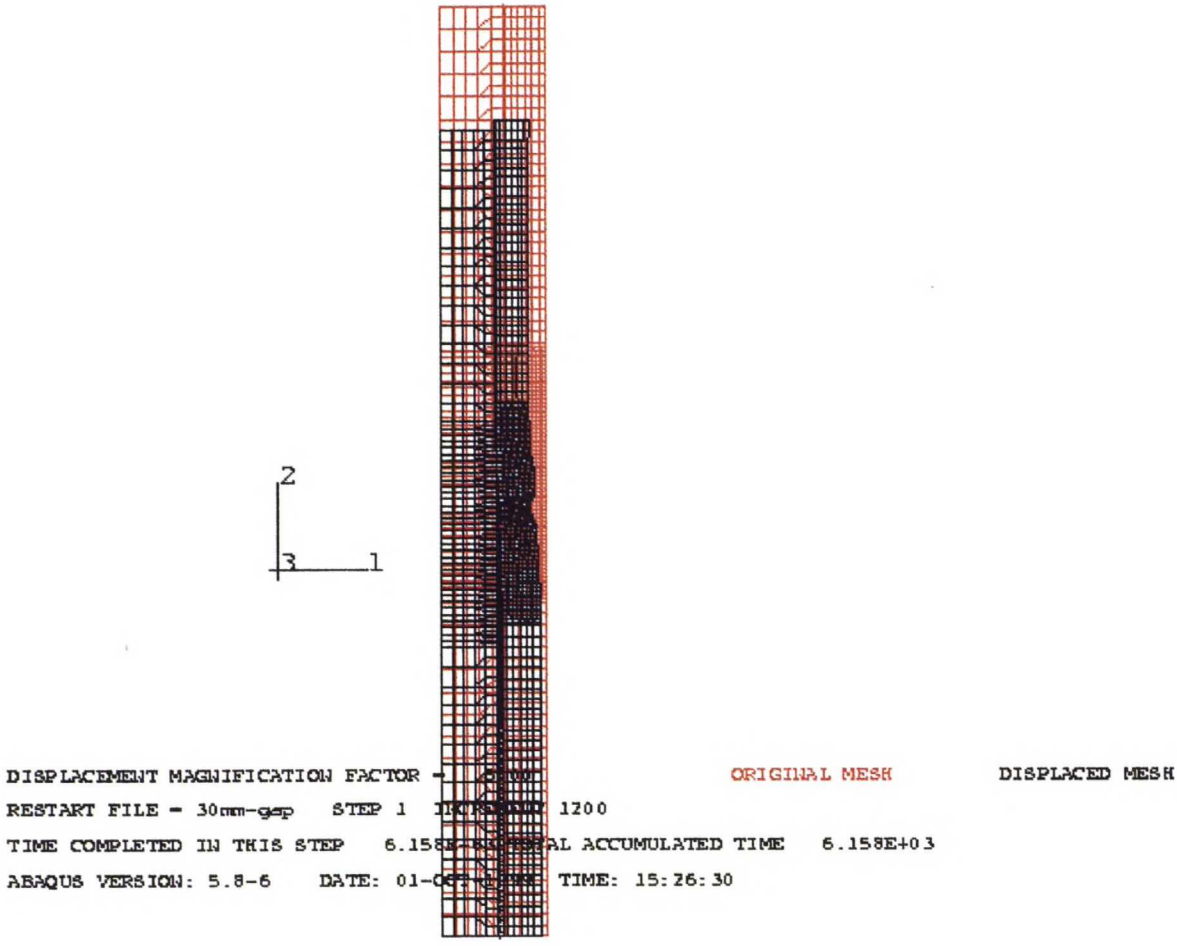

Figure 9.1 Displaced shape of the element model in the final state, at the last time increment (total accumulated time is 6158 seconds) in Case 3. The displacements are multiplied by five. The original mesh is in red color.

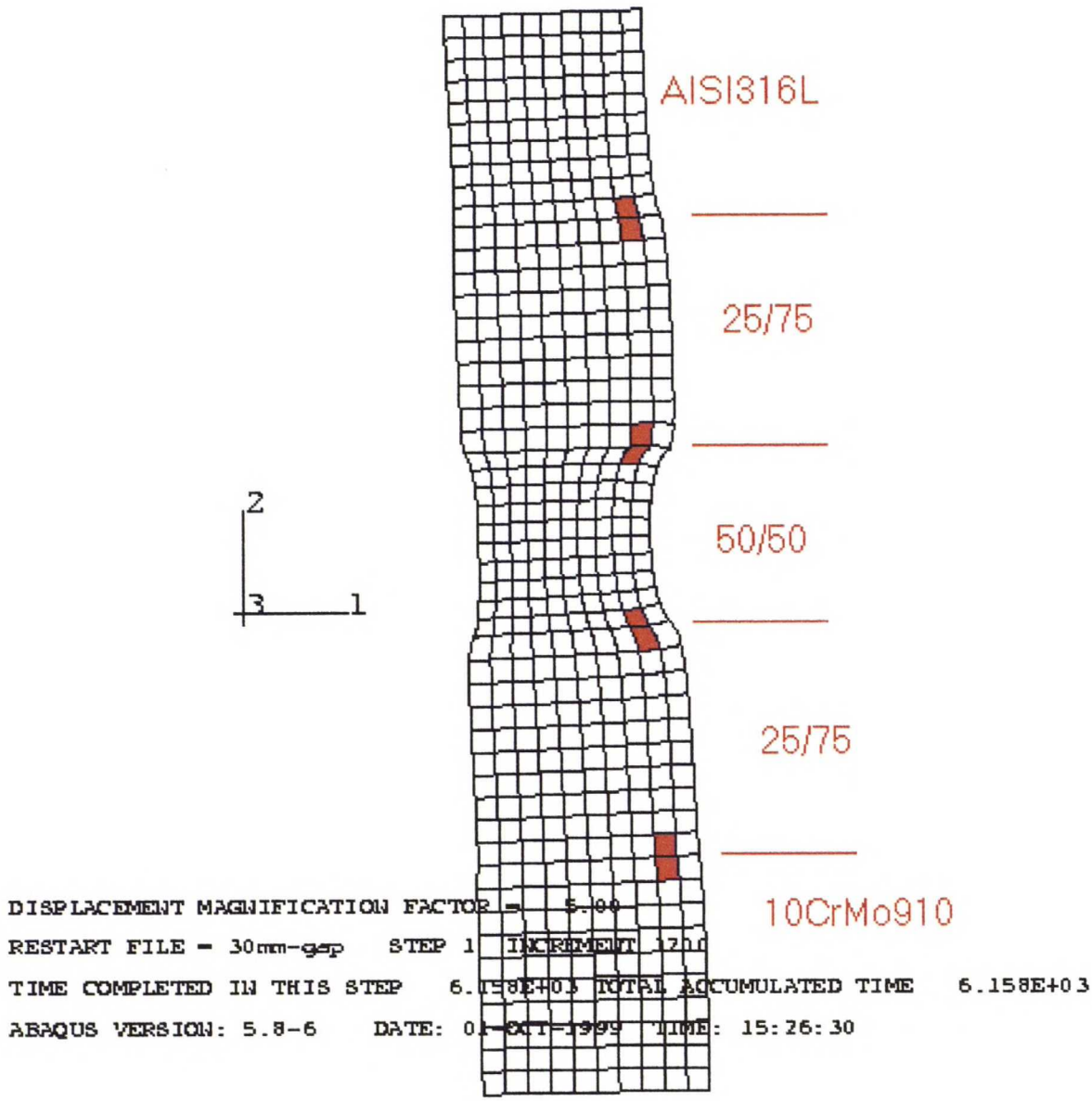

Figure 9.2 Detail of Figure 9.1. The detail is from the FG-region of the component. The displacement magnification factor is 5. The interfaces between each material are marked. The elements used in Tables 6.1-4 are colored red.

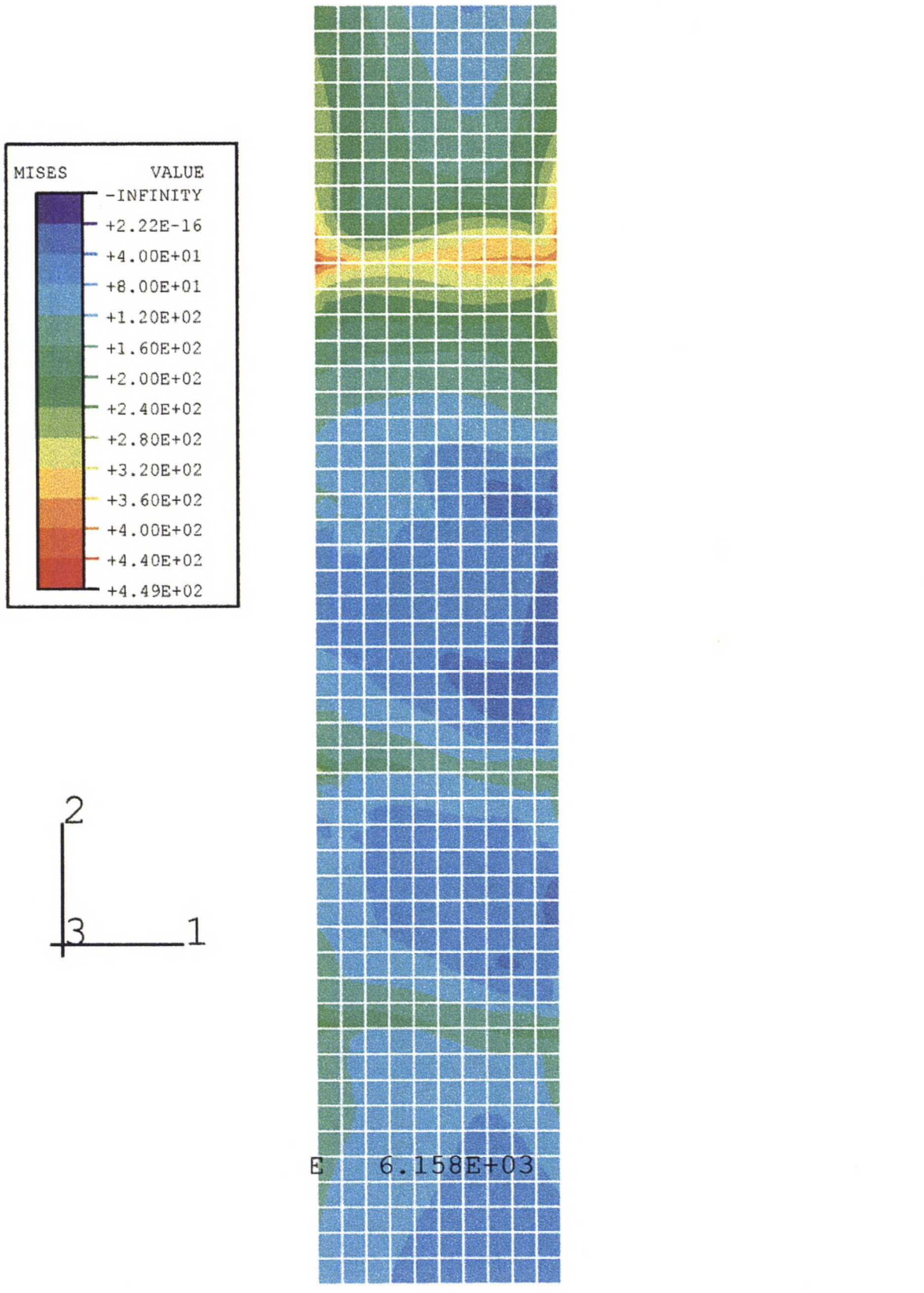

Figure 9.3 Contour plot of von Mises stress distribution in the FG-region. Case 3. The 10 element columns represent the powder materials (middle part of the finished component). The contours are at 40 MPa intervals. Stress magnitudes over 440 MPa are colored red.

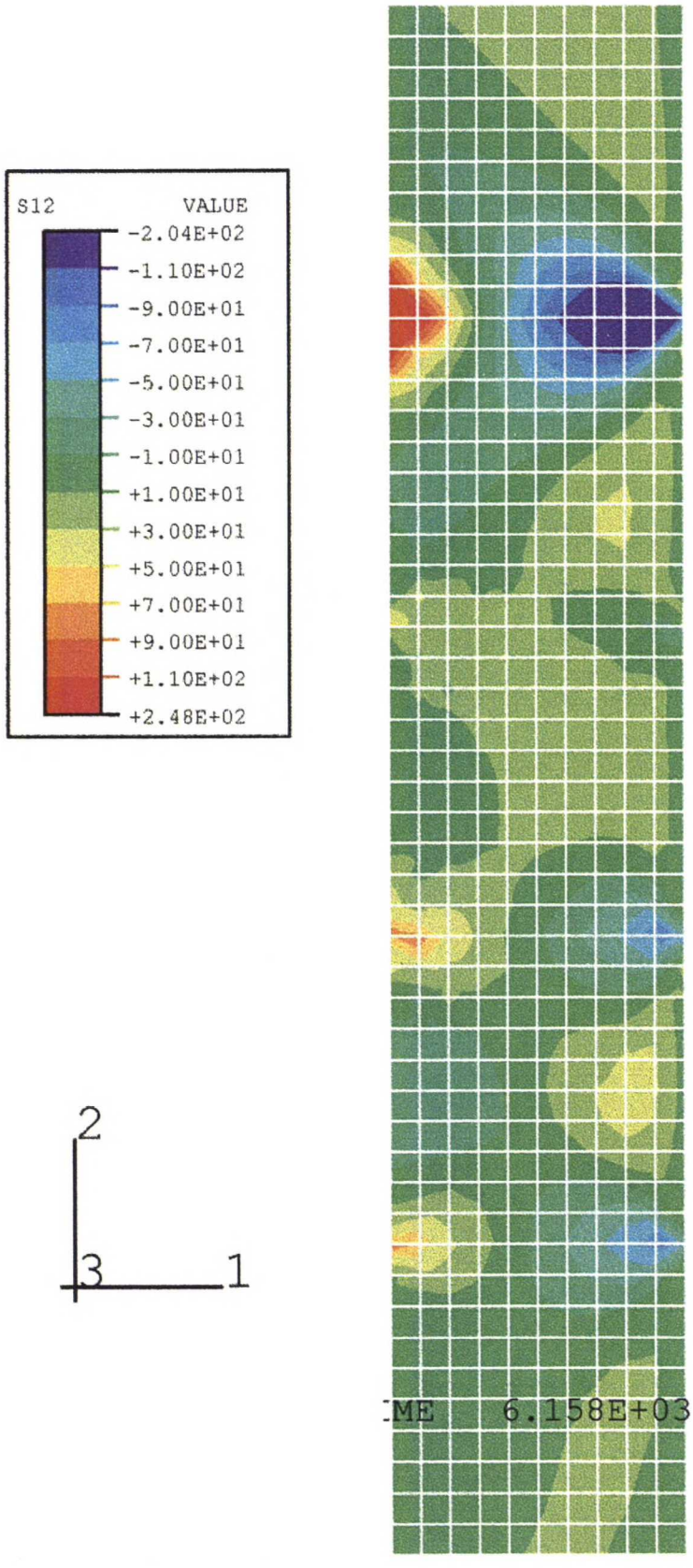

Figure 9.4 Contour plot of shear stress (σ_{12}) distribution in the FG-region. Case 3. The scale is from -110 MPa to 110 MPa.

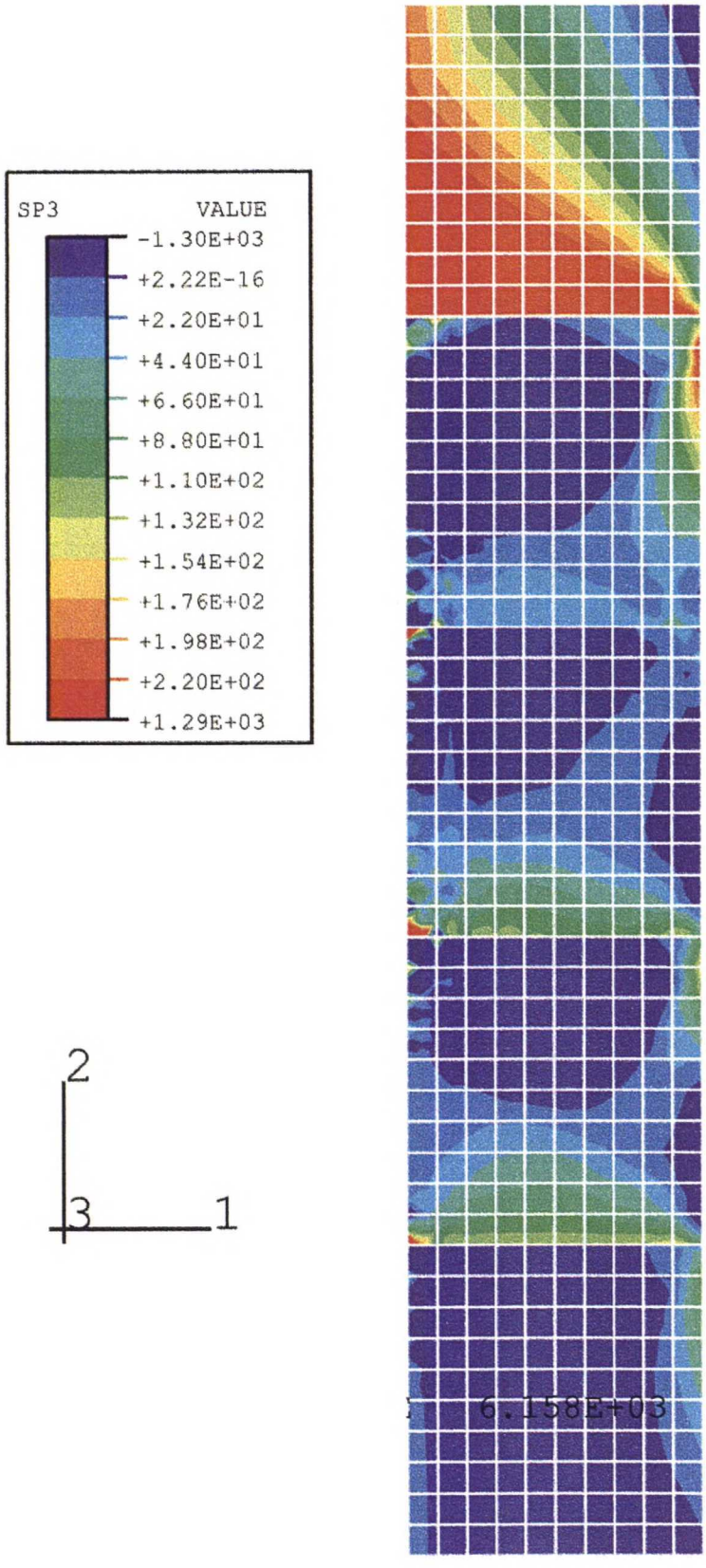

Figure 9.5 Contour plot of the maximum principal stress distribution (σ_3) in the FG-region. Case 3. The scale is from zero to 220 MPa. Positive stress values are tension. Dark blue color represents compression.

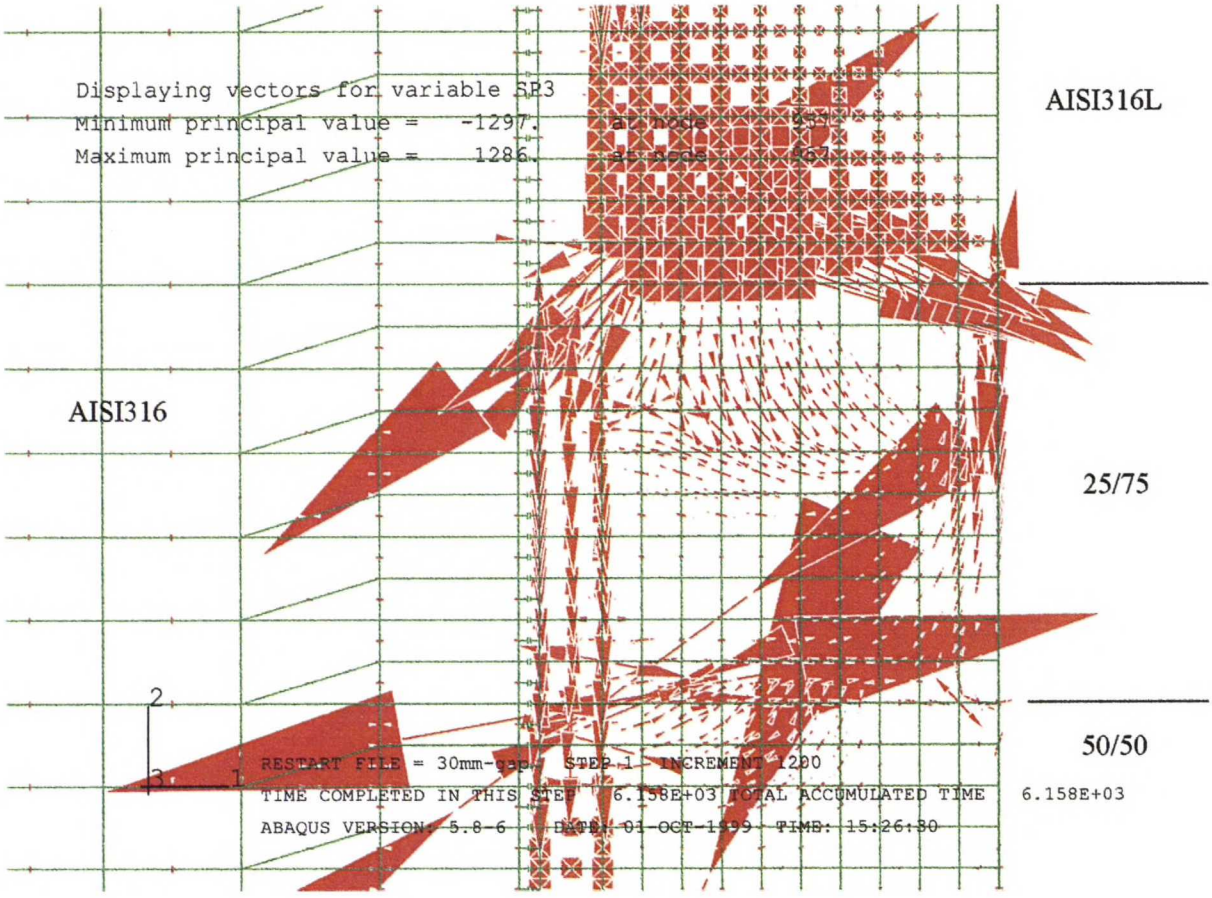

Figure 9.6 Vector plot of the maximum principal stress in the upper FG-region. Case 3. The direction of the arrow shows the direction of σ_3 in the corresponding node. Arrow size stands for the stress magnitude. Arrows pointing outwards from the node are tension.

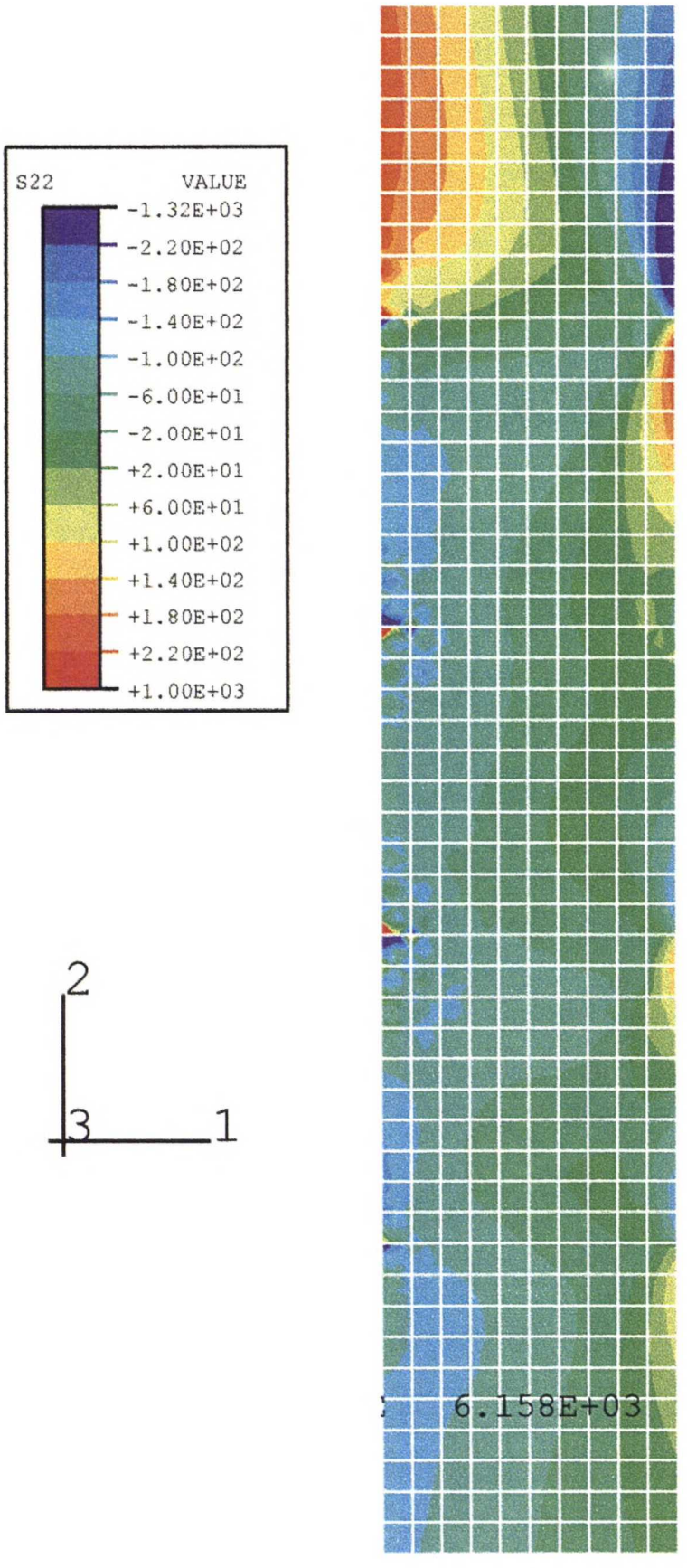

Figure 9.7 Contour plot of axial stress (σ_{22}) distribution in the FG-region. Case 3. The scale is from -220 MPa to 220 MPa.

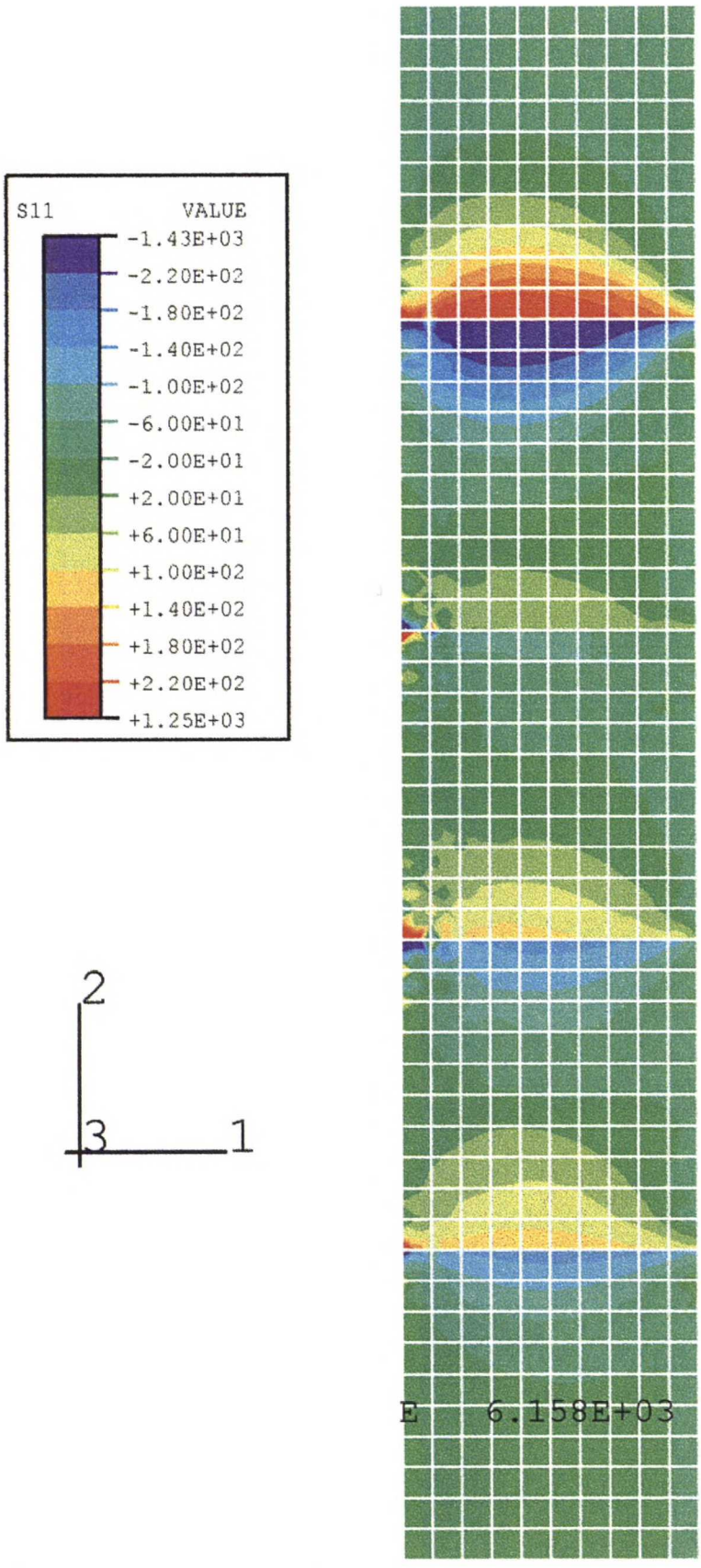

Figure 9.8 Contour plot of radial stress (σ_{11}) distribution in the FG-region. Case 3. The scale is from -220 MPa to 220 MPa.

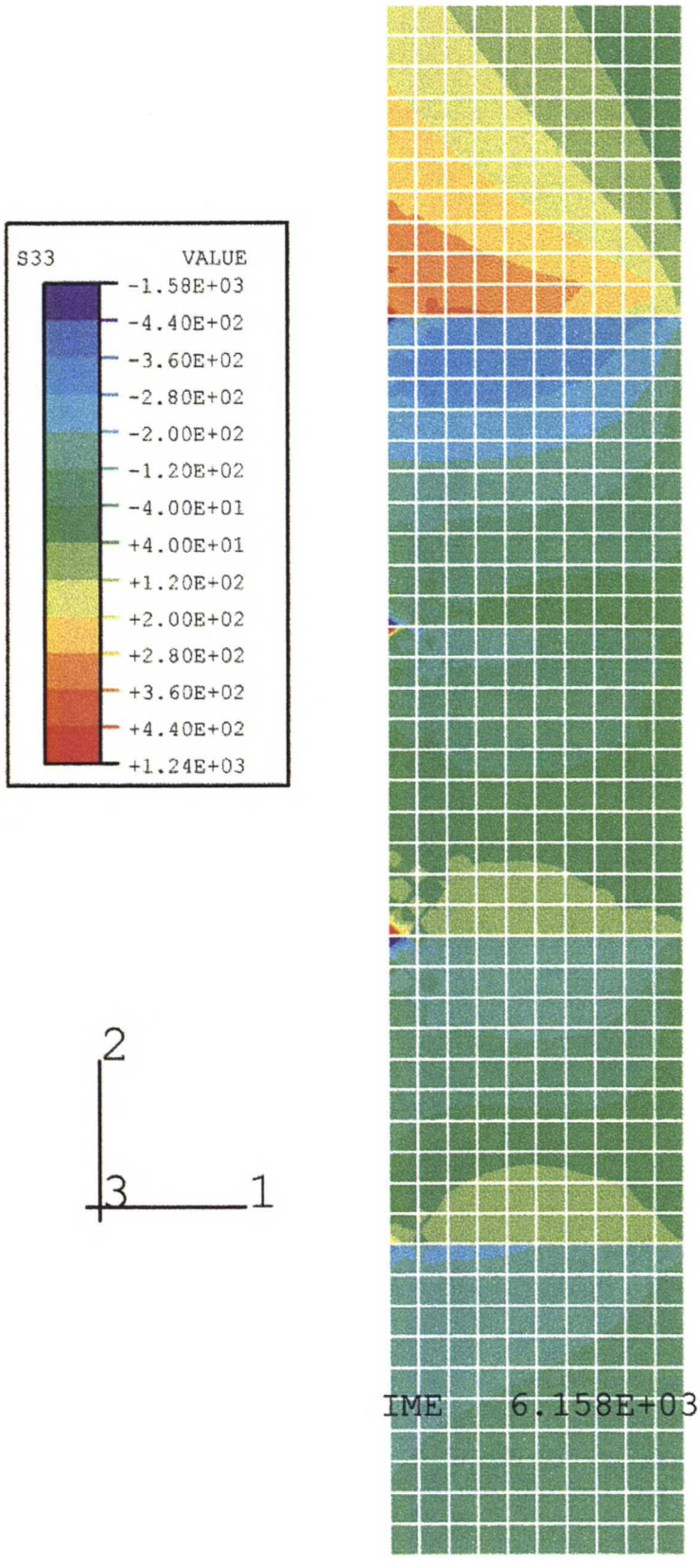

Figure 9.9 Contour plot of circumferential stress (σ_{33}) distribution in the FG-region. Case 3. The scale is from -440 MPa to 440 MPa.

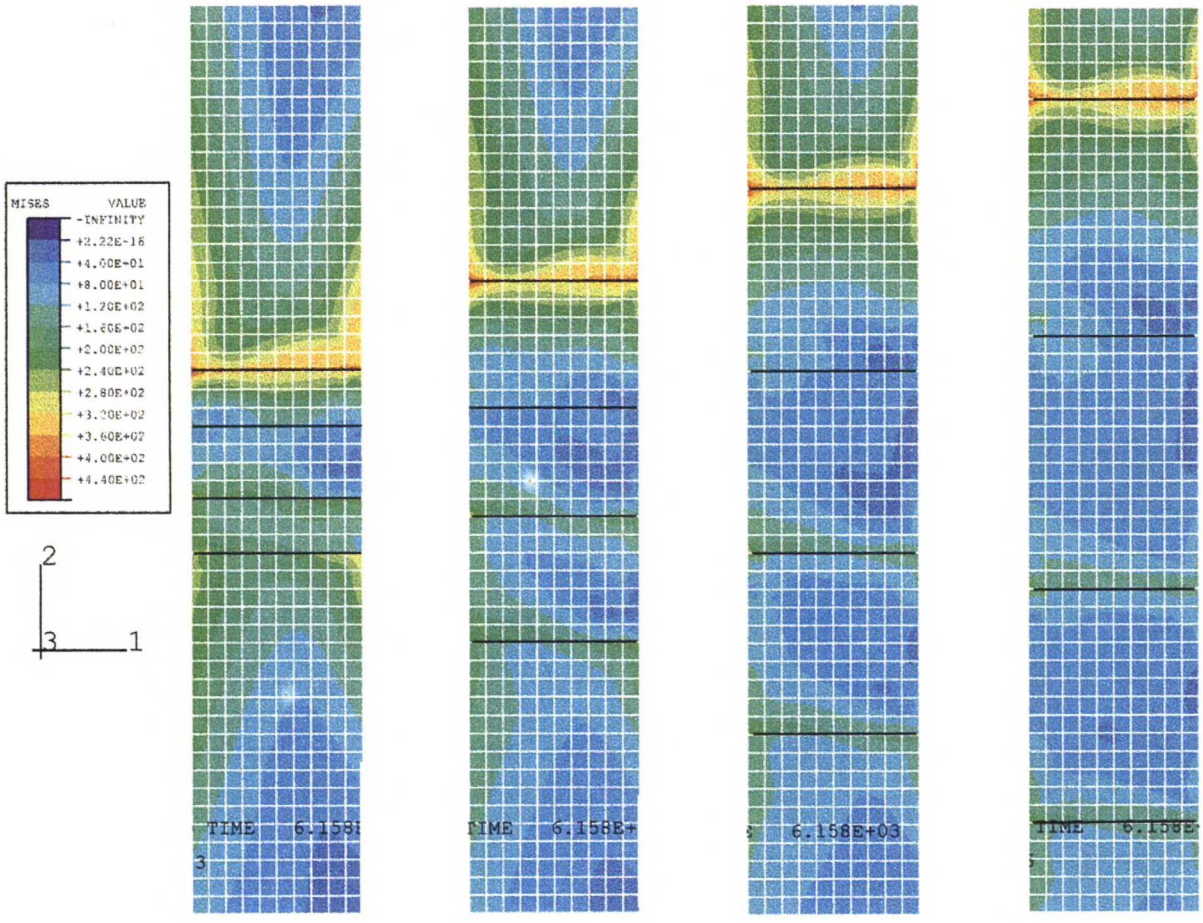

Figure 9.10 Contour plots of von Mises stress distribution in Cases 1-4, from left to right. The material interfaces are marked with dark lines. The scale of the legend is the same as in Figure 9.3 (from zero to 440 MPa) and the maximum values in Cases 1-4 are 482 MPa, 452 MPa, 449 MPa, 455 MPa, respectively.

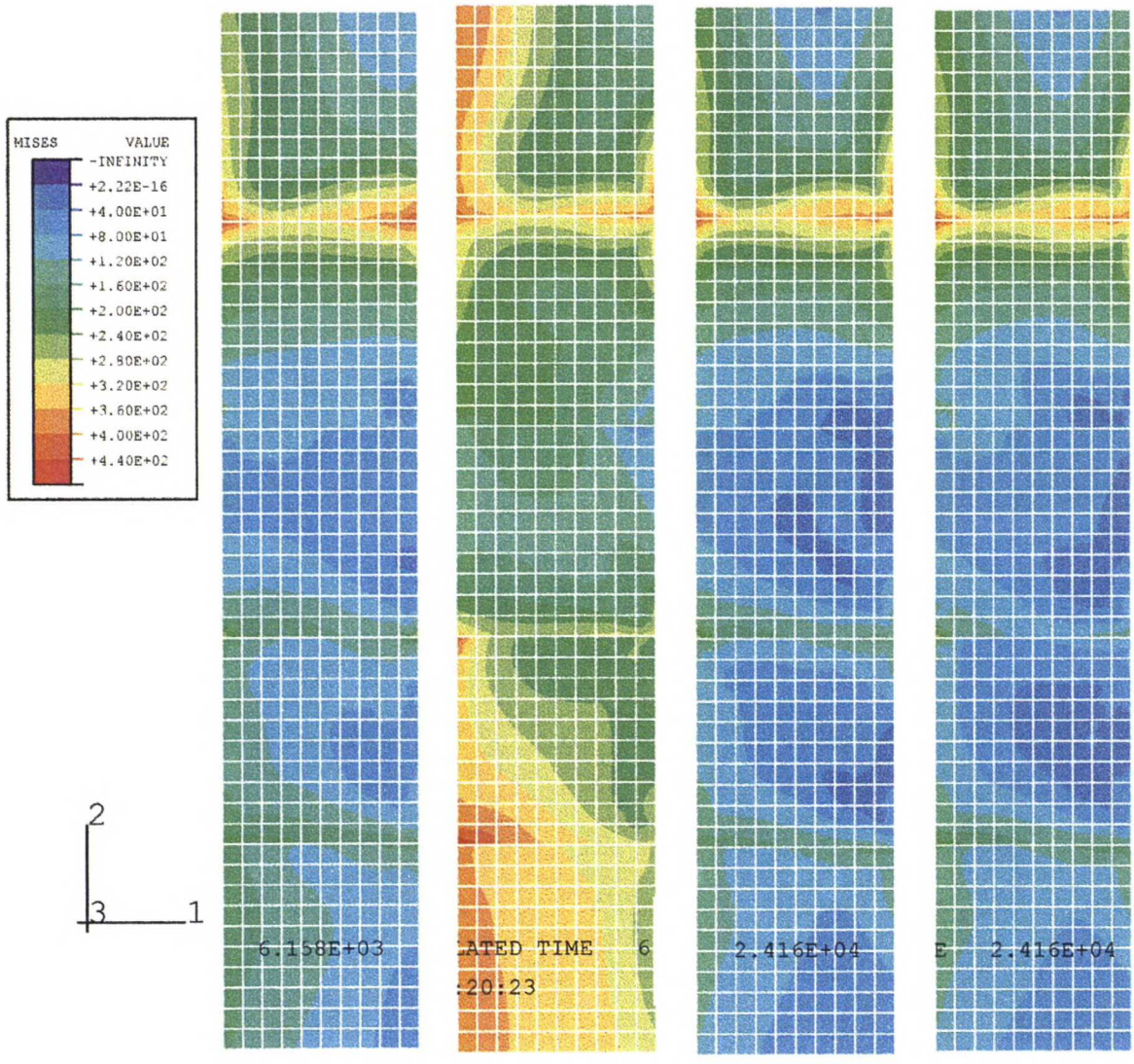

Figure 9.11 Contour plots of von Mises stress distribution in Cases 5-8, from left to right. The scale of the legend is the same as in Figure 9.3 (from zero to 440 MPa) and the maximum values in Cases 5-8 are 468 MPa, 496 MPa, 448 MPa and 450 MPa, respectively.

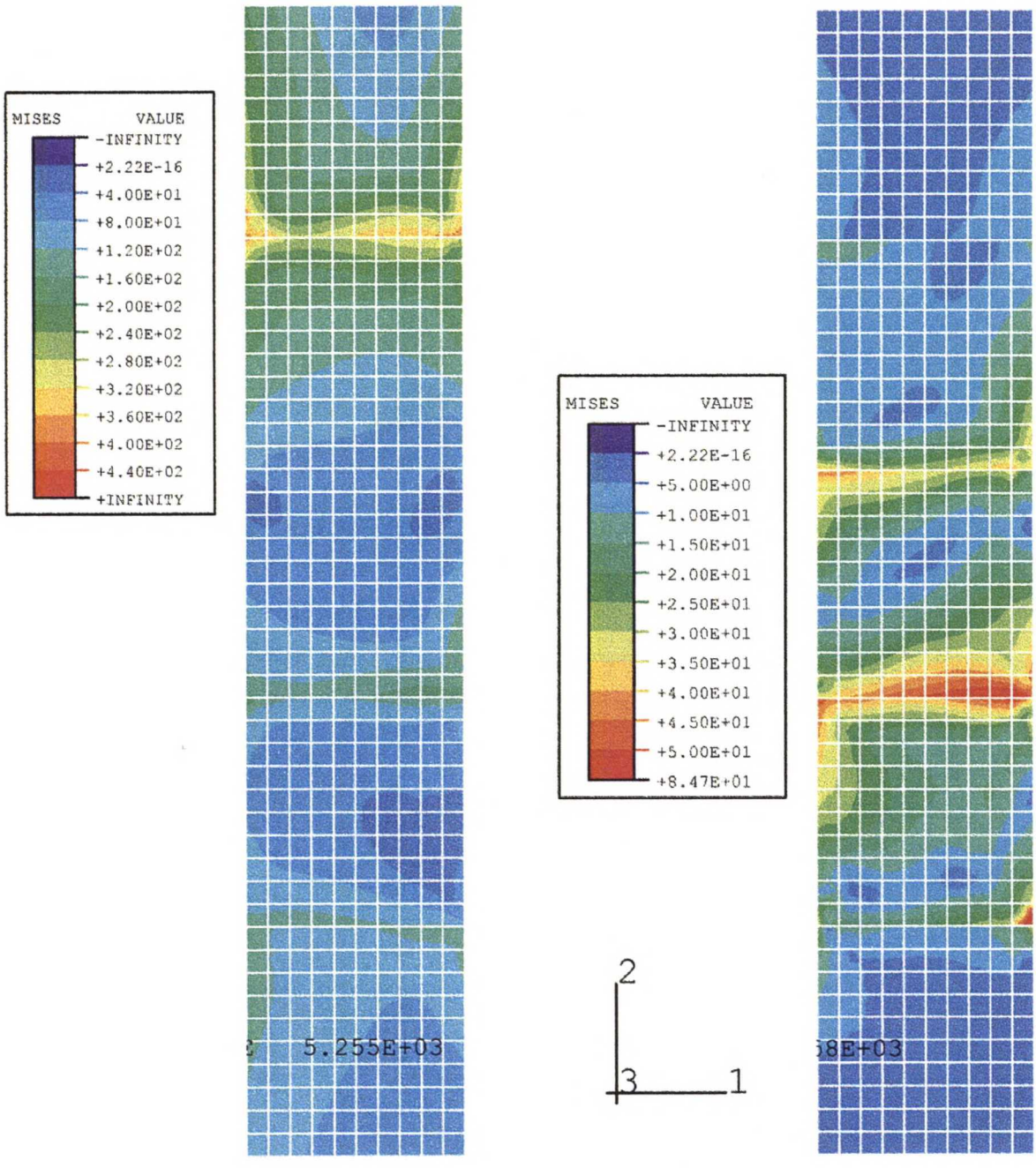

Figure 9.12 Contour plots of von Mises stress distribution in Case 9 (left) and Case 10 (right). The scaling in Case 9 is the same as in Figure 9.3, but the maximum value is indefinable. The scaling in Case 10 is from zero to 50 MPa and the maximum value is 85 MPa.

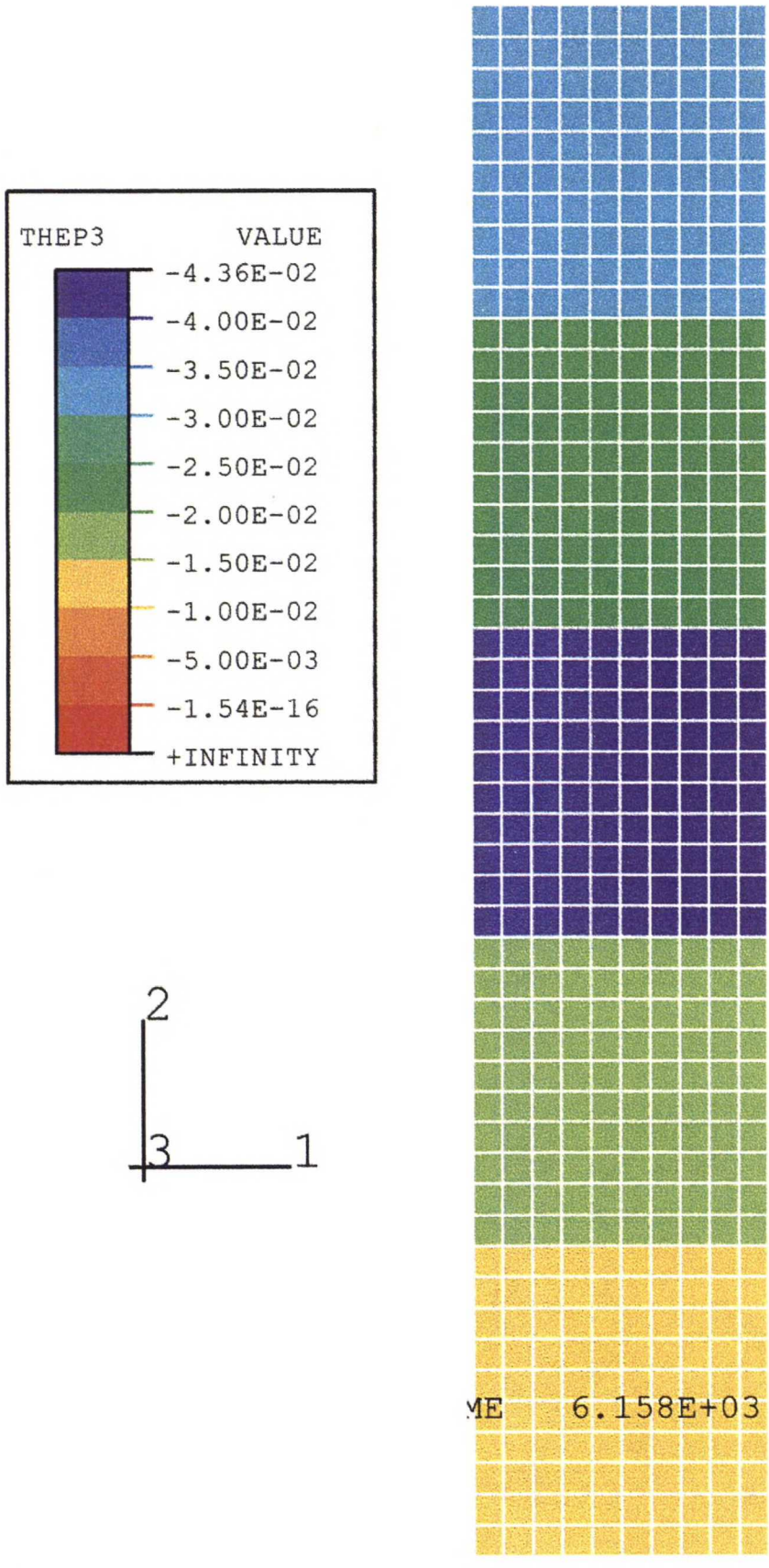

Figure 9.13 Contour plot of thermal strain (ε^{th}) in the FG-region. Case 3.

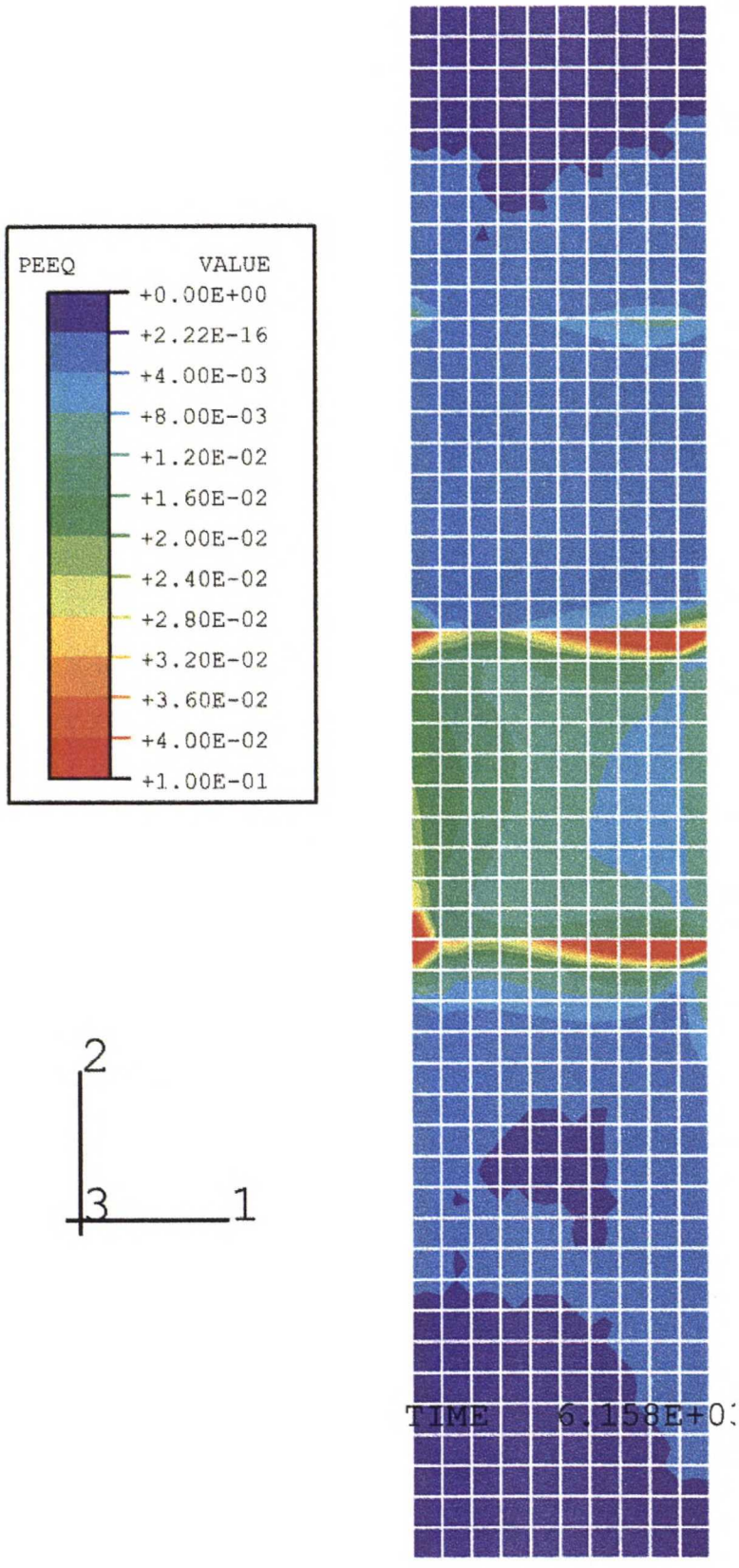

Figure 9.14 Contour plot of equivalent plastic strain ($\bar{\varepsilon}^{pl}$) in the FG-region. Case 3. The scale is from 0 to 4 % (values over 4% are represented by red color, highest values are about 10 %).

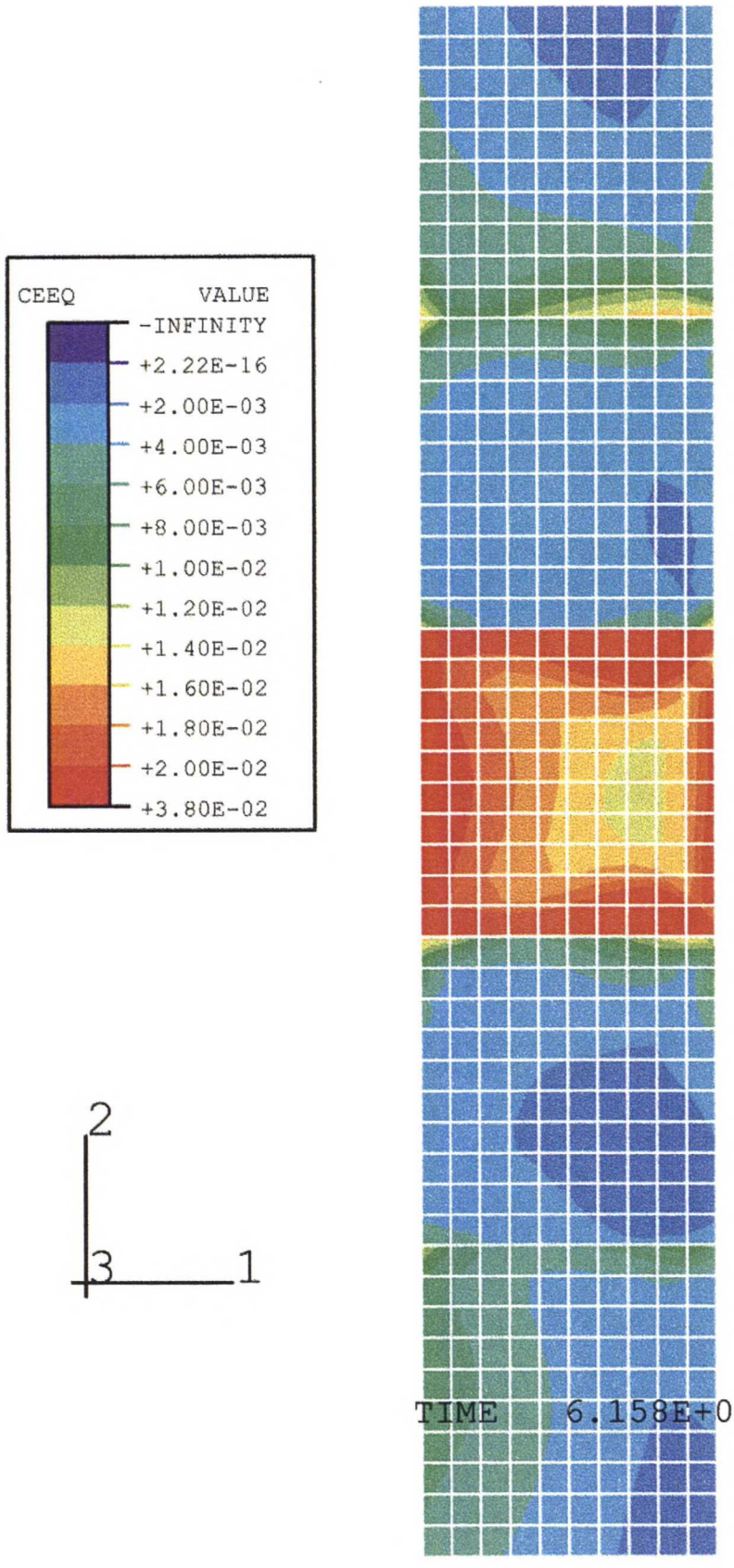

Figure 9.15 Contour plot of equivalent creep strain ($\bar{\varepsilon}^{cr}$) in the FG-region. Case 3. The scale is from 0 to 2 %. Red color represents values between 2% and the maximum value 3.8%.

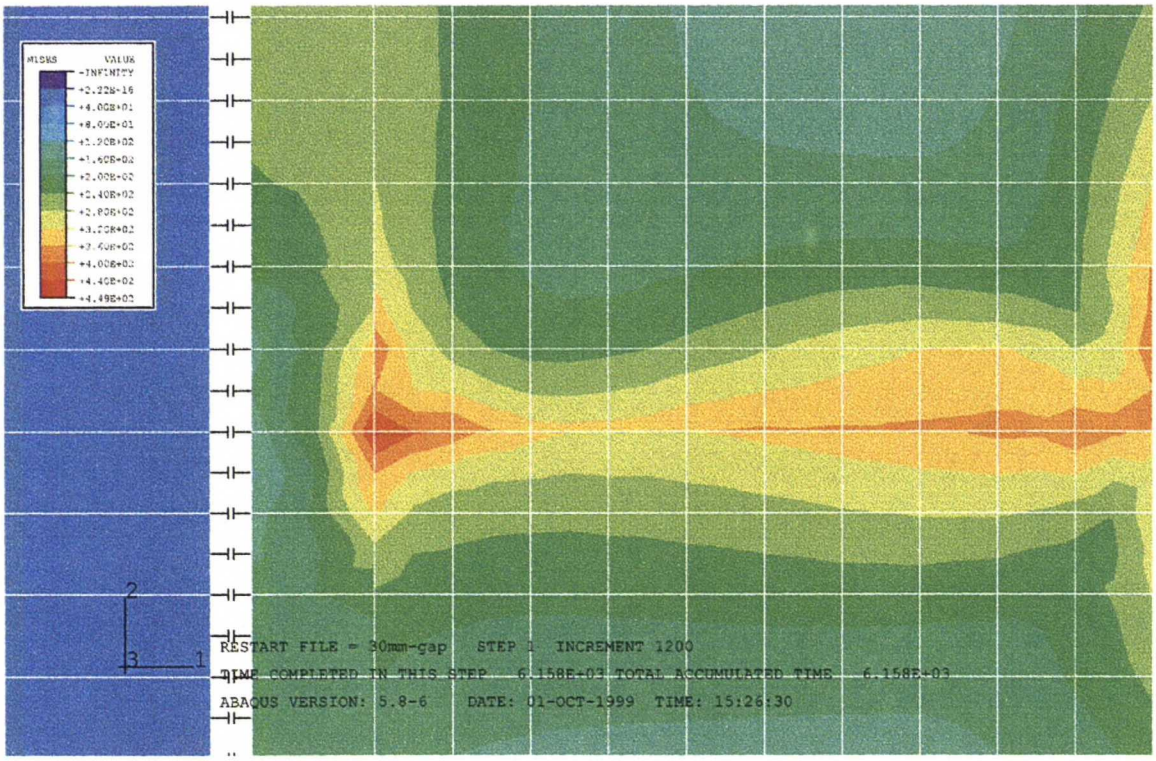

Figure 9.16 Contour plot of von Mises stress distribution near the interface between AISI316L steel and 25/75 steel. Case 3. A detail of Figure 9.3 with the same scale in the legend.

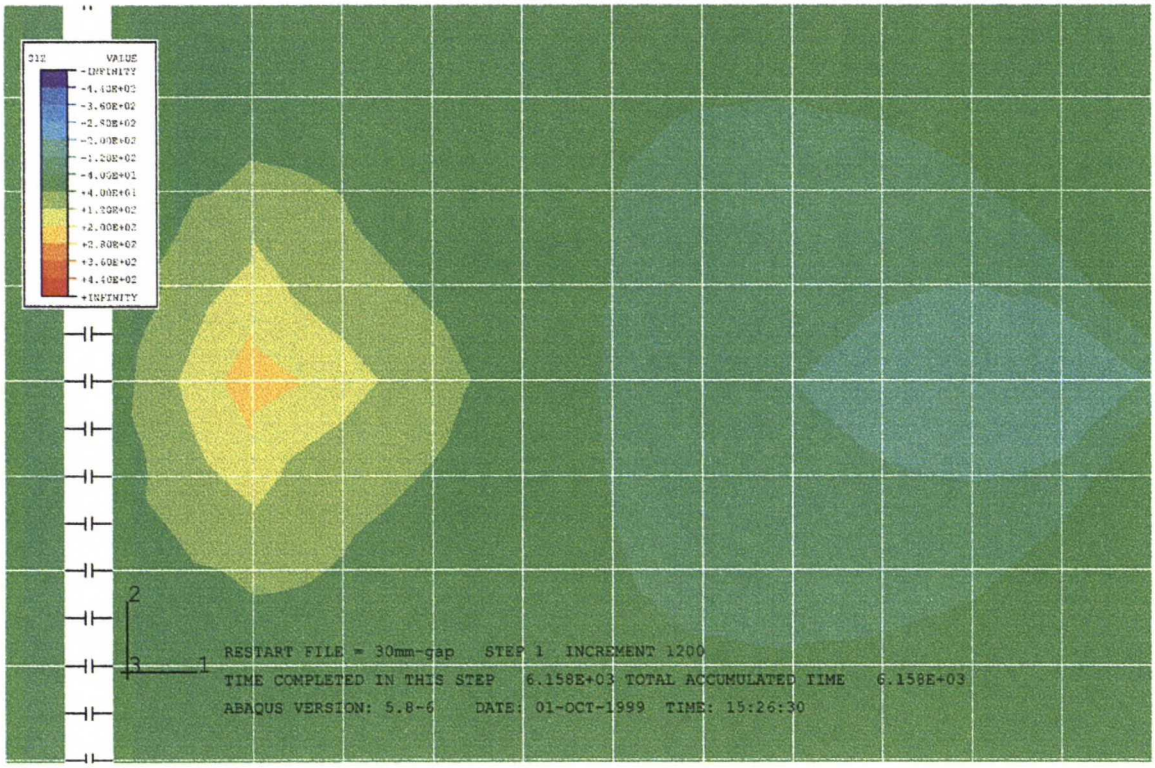

Figure 9.17 Contour plot of shear stress distribution near the interface between AISI316L steel and 25/75 steel. Case 3. A detail of Figure 9.4.

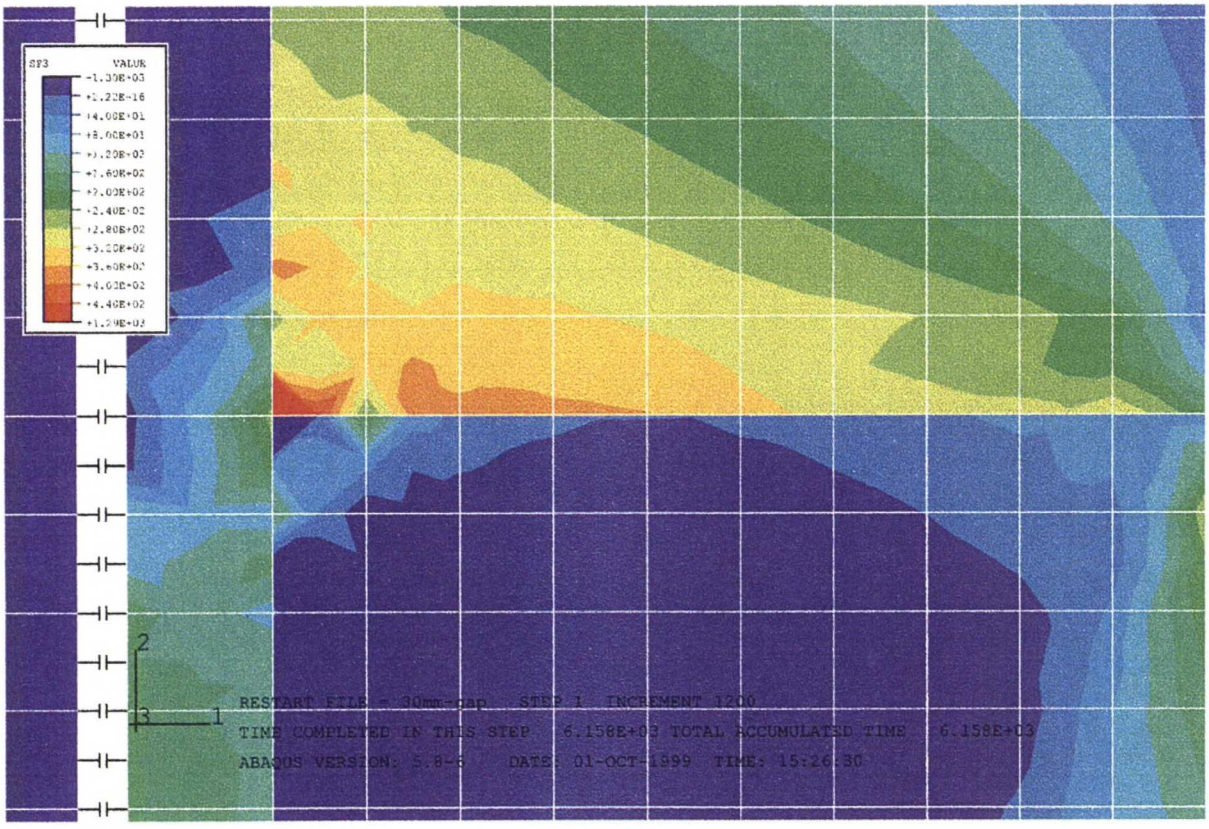

Figure 9.18 Contour plot of the maximum principal stress distribution near the interface between AISI316L steel and 25/75 steel. Case 3. A detail of Figure 9.5.

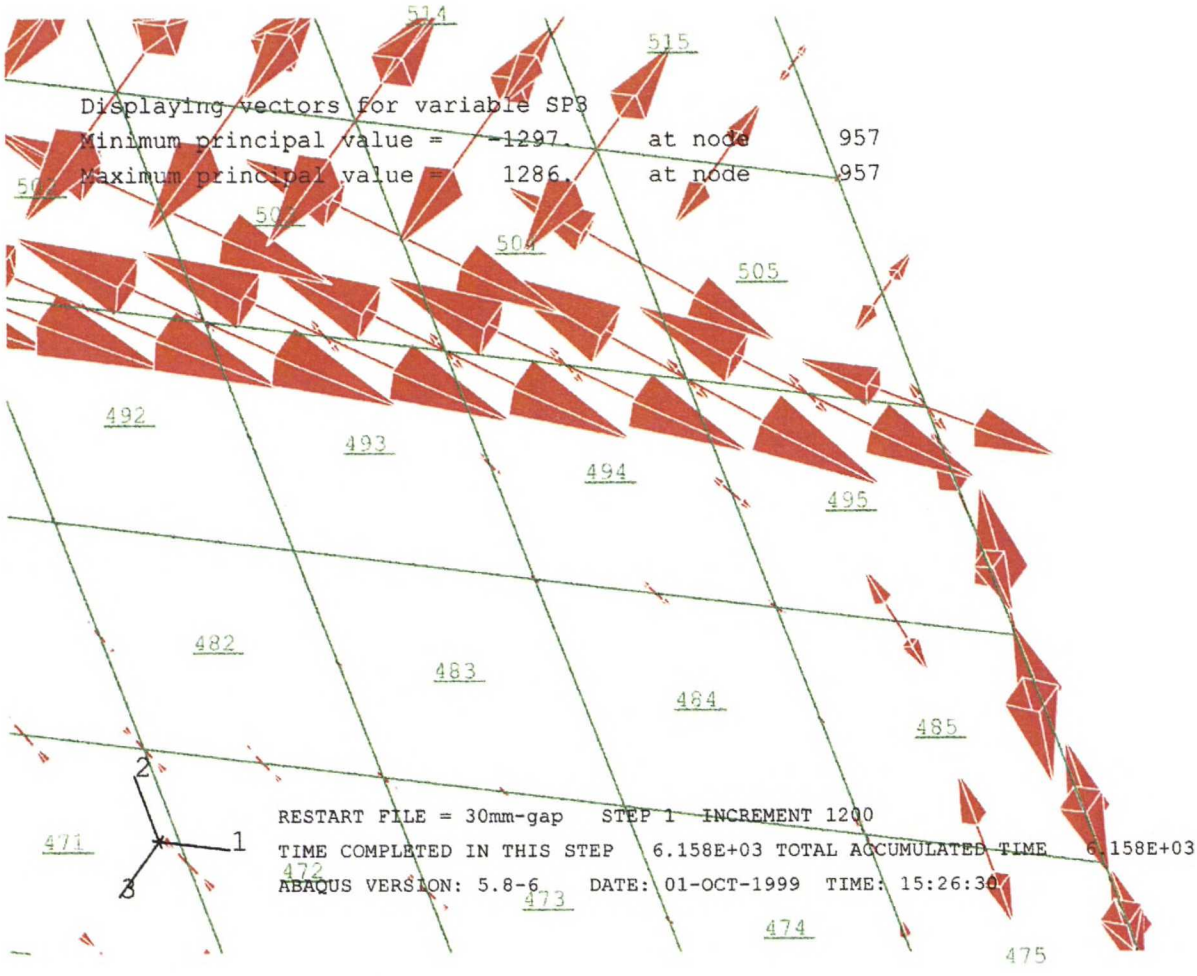

Figure 9.19 Rotated plot of maximum principal stress vectors near the interface between AISI316L steel and 25/75 steel (the interface is between elements 505 and 495) and the outer radial free edge. Case 3. Shows the direction of the stresses in Figure 9.18.

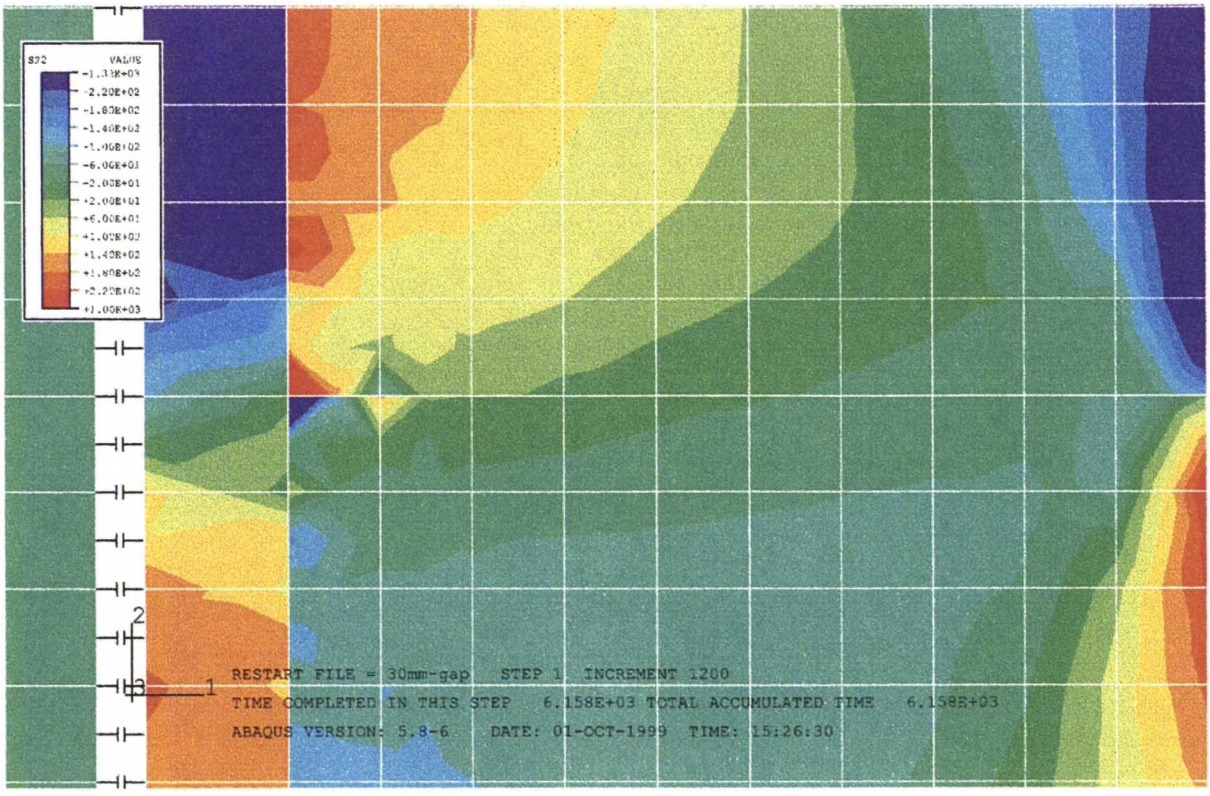

Figure 9.20 Contour plot of the axial stress distribution near the interface between AISI316L steel and 25/75 steel. Case 3. A detail of Figure 9.7

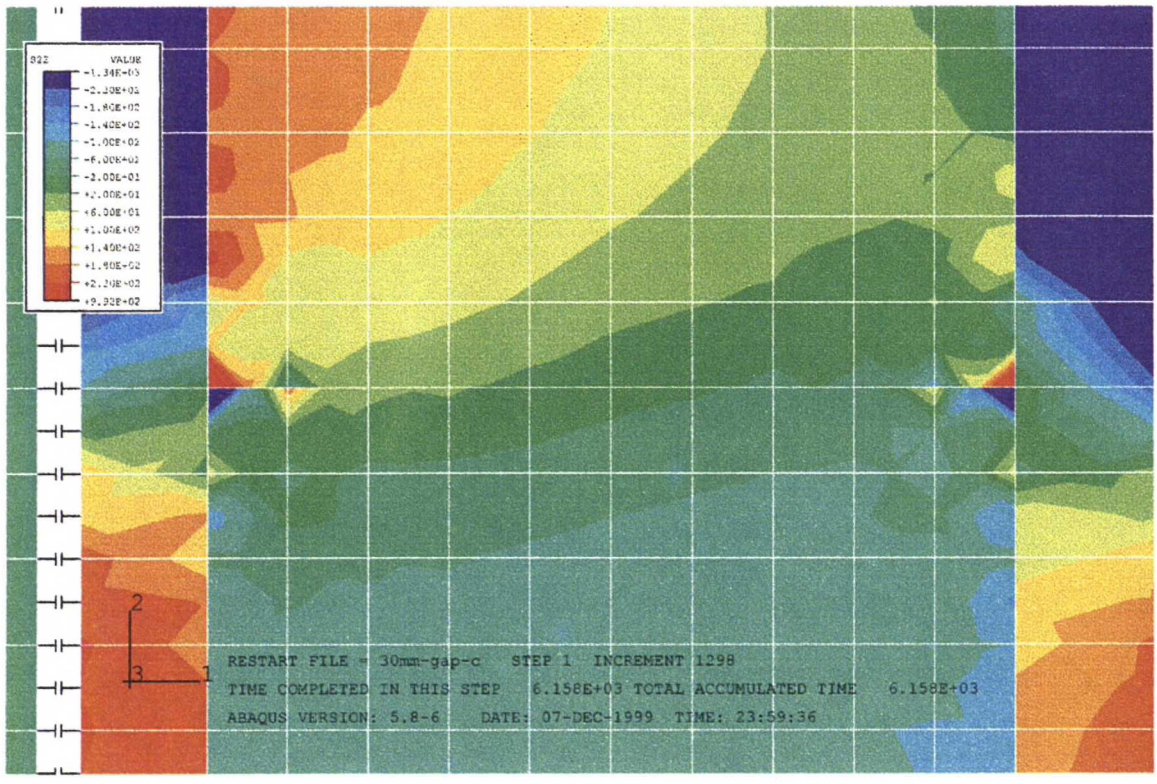

Figure 9.21 Contour plot of the axial stress distribution near the interface between AISI316L steel and 25/75 steel. Case 5.

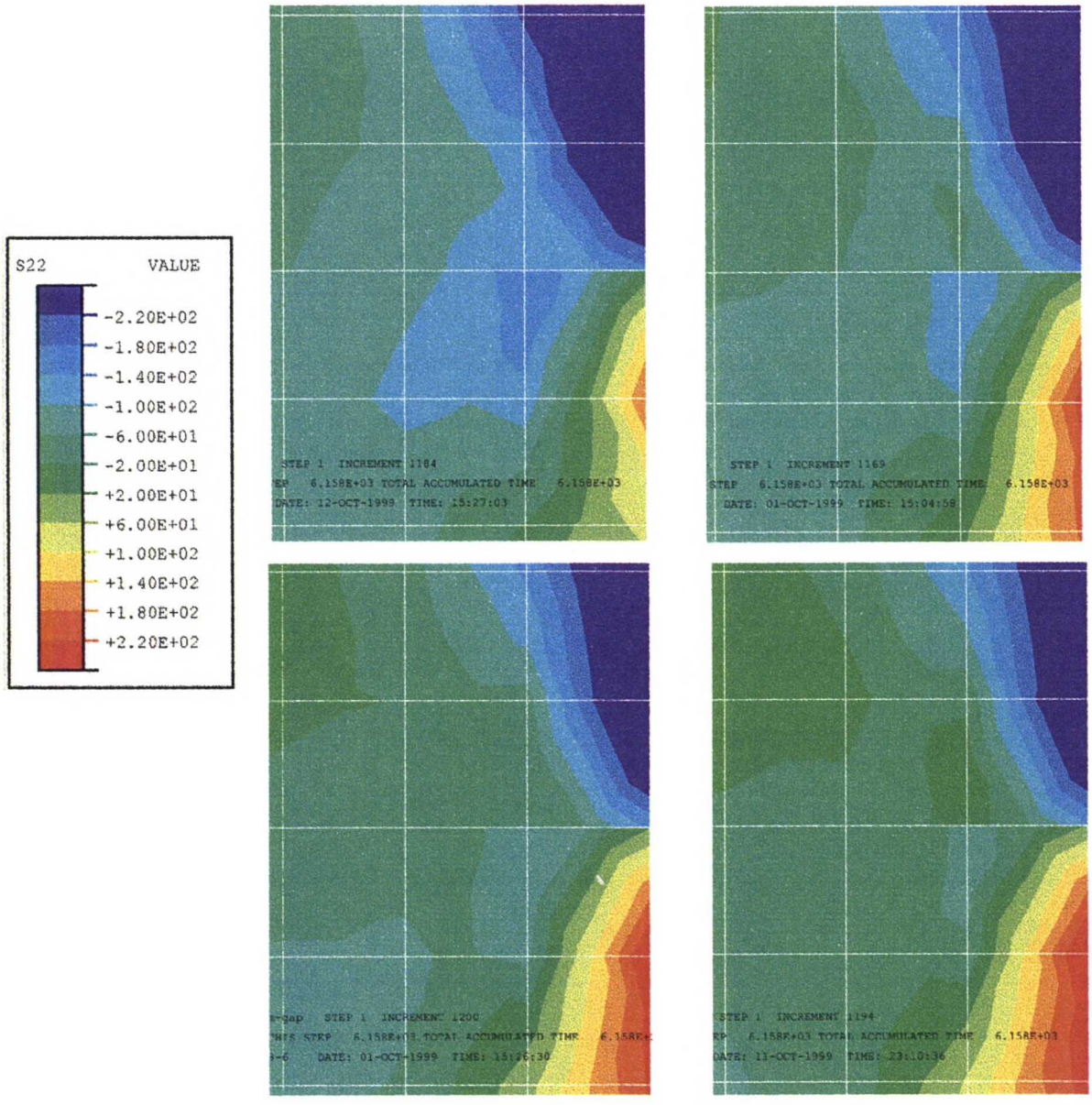

Figure 9.22 Contour plots of the axial stress distributions of Cases 1-4 near the outer radial free edge. Case 1 is on the upper left corner, Case 2 is on the upper right corner, Case 3 is on lower left corner and Case 4 is on the lower right corner of the page. The stresses are at 40 MPa intervals. Red represents tensile stresses of magnitude over 220 MPa and dark blue represents compression of magnitude over 220 MPa.

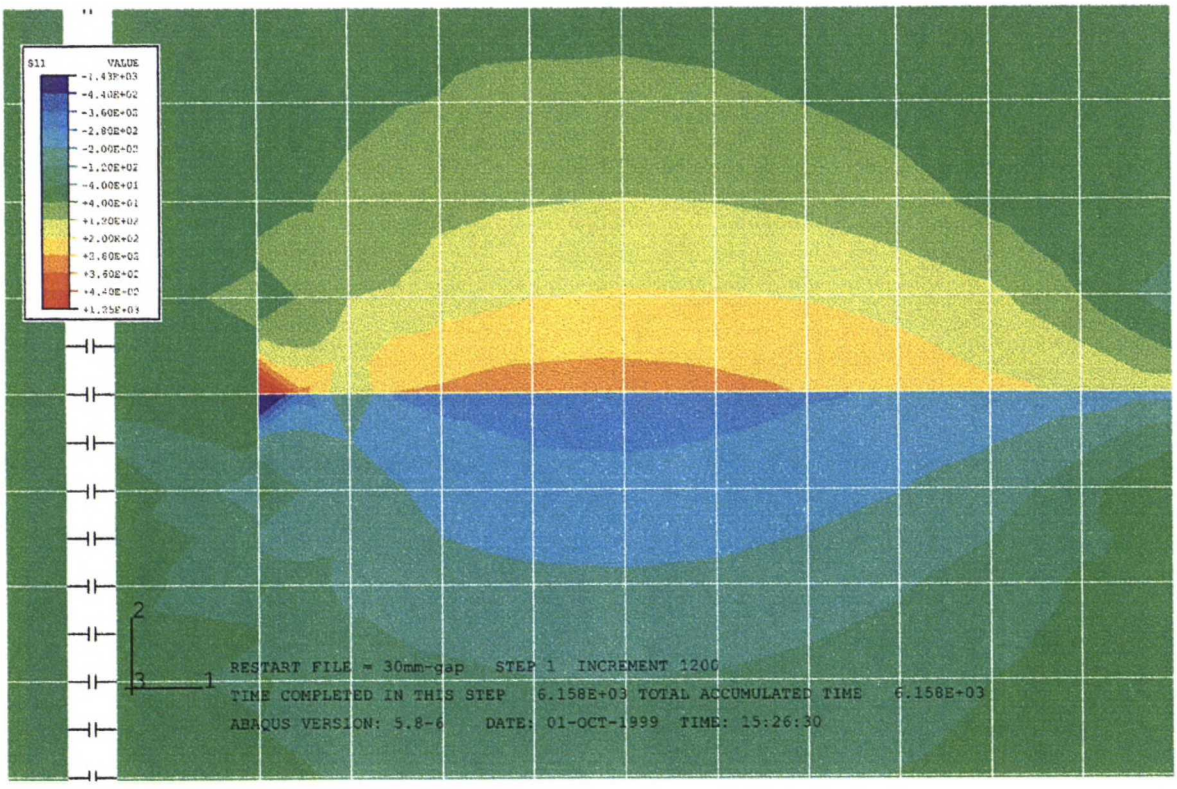

Figure 9.23 Contour plot of the radial stress distribution near the interface between AISI316L steel and 25/75 steel. Case 3.

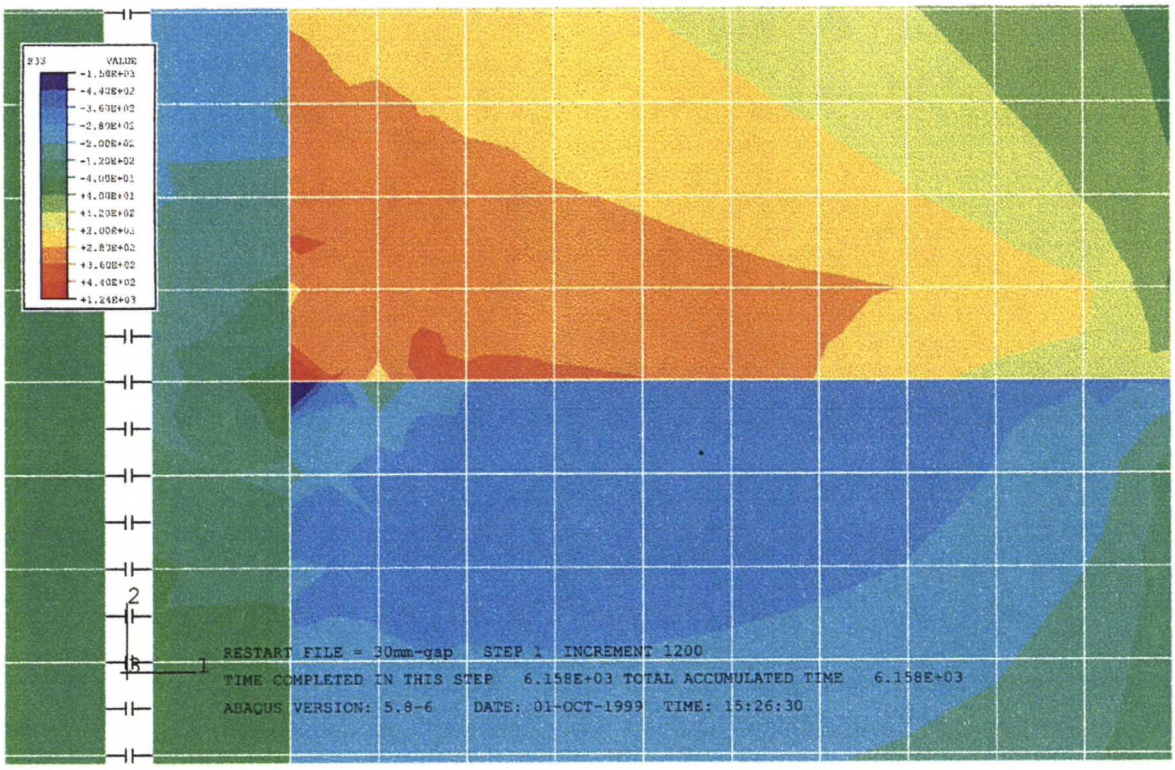

Figure 9.24 Contour plot of the circumferential stress distribution near the interface between AISI316L steel and 25/75 steel.